

# CONTROL OF A HIGHLY MANEUVERABLE MULTI-MEDIUM VEHICLE EMPLOYING MULTI-PLANE PROPULSION

by

MARCO M. MAIA

A dissertation submitted to the

School of Graduate Studies

Rutgers, The State University of New Jersey

In partial fulfillment of the requirements

For the degree of

Doctor of Philosophy

Graduate Program in Mechanical and Aerospace Engineering

Written under the direction of

F. Javier Diez

And approved by

---

---

---

---

New Brunswick, New Jersey

January, 2018

## **ABSTRACT OF THE DISSERTATION**

# **Control of a Highly Maneuverable Multi-medium Vehicle Employing Multi-plane Propulsion**

**By MARCO M. MAIA**

**Dissertation Director:**

**F. Javier Diez**

Multi-medium vehicles, which are capable of operating in multiple fluid mediums such as air and water, are a new paradigm in unmanned systems and the multirotor platform is an exceptional candidate configuration. Vehicles that can swim and fly are few and those that do exist are not maneuverable enough to accomplish complex missions. A multi-plane propulsion system is introduced that ensures seamless transition and sets forth some basic requirements and considerations on designing multi-medium multirotor vehicles which touches on hardware level components as well as firmware for the autopilot and the motor drivers. Five prototypes have been developed and these fully developed platforms adopted several control schemes that when aggregated, properly handle the continuous-discrete behavior that a multi-medium vehicle entails. The propulsion system was characterized and used to determine the approximate drag coefficient at several pitch angles and speeds, which helped validate the pseudo-spherical drag model as a reasonable candidate for the overall dynamic

model, especially at low speeds. From a controls standpoint, a standard multirotor controller employing a hierarchical PID controller was formalized. Next, this hierarchical controller was incorporated into a discrete-continuous system through a hybrid controller. Then, a gain scheduling algorithm was added by exploiting the discrete variables established by the hybrid system. Finally, a singularity-free quaternion representation was used such that a hierarchical hybrid quaternion controller with gain scheduling renders the vehicle highly maneuverable, agile and adept at each medium of operation. Several numerical simulations and experiments were conducted to assess vehicle performance with regard to maneuverability and convergence to a desired state.

## Acknowledgements

I am deeply grateful to my advisor, mentor, and friend F. Javier Diez-Garias for guiding me through this very awesome journey, teaching and continuously motivating me to *think big, think creatively*, yet also simply—so as to best achieve unrelenting success.

I am also incredibly indebted to my family, friends and loved ones who have given me so much emotional and spiritual support and so much to strive for not only in my professional life, but in all aspects of it. In particular, I want to thank my mother for being so present in all things.

The authors gratefully acknowledge the financial support provided for this study by the Office of Naval Research (ONR), Grant No. N00014-15-2235, with Dr. Thomas McKenna serving as Program Manager.



# Table of Contents

<b>Abstract</b> . . . . .	ii
<b>Acknowledgements</b> . . . . .	iv
<b>List of Tables</b> . . . . .	viii
<b>List of Figures</b> . . . . .	ix
<b>1. Introduction</b> . . . . .	1
1.1. Motivation and goals . . . . .	1
1.2. Review of multirotor vehicles . . . . .	2
1.3. Review of underwater vehicles . . . . .	2
1.4. Review of multi-medium vehicles . . . . .	3
1.5. The challenge and objective . . . . .	5
<b>2. Multi-Medium Transition for multirotor vehicles</b> . . . . .	6
2.1. Multi-plane transition strategy . . . . .	7
2.2. Dual-plane/Coaxial based transition . . . . .	9
<b>3. Design requirements of a multi-medium multirotor</b> . . . . .	11
3.1. Rotor Configuration . . . . .	12
3.2. Structural construction and pressure vessel . . . . .	14
3.3. Propulsion system for multi-medium vehicles . . . . .	16
3.3.1. Motors and Electronic Speed Controllers (ESC) . . . . .	16
3.4. Autopilot system and basic sensors for multi-medium vehicles . . . . .	18
<b>4. Design iterations of a multi-medium multirotor vehicle</b> . . . . .	20

4.1. Naviator-NV1: Proof of concept . . . . .	21
4.2. Naviator-NV2: Higher depth range . . . . .	21
4.3. Naviator-NV3: Enabling low UW rotor speeds . . . . .	22
4.4. Naviator-NV4: Maximizing high UW rotor speeds . . . . .	23
4.5. Naviator-NV5: Control strategy test platform . . . . .	23
4.6. Naviator-NV6: A stronger, smarter vehicle . . . . .	24
<b>5. Dynamic Model of a multi-medium multirotor vehicle . . . . .</b>	<b>25</b>
5.1. Frames of reference . . . . .	26
5.2. Dynamic model for aerial multirotors . . . . .	26
5.3. Dynamic model for multi-medium multirotors . . . . .	30
5.3.1. Buoyancy forces and moments . . . . .	30
5.3.2. Translational and angular drag forces . . . . .	31
<b>6. Parameter Identification . . . . .</b>	<b>36</b>
6.1. Mass, Volume and Moment of Inertia . . . . .	36
6.2. Propulsion . . . . .	37
6.3. Restoring Forces . . . . .	42
6.4. Drag Coefficient and Drag Forces . . . . .	43
<b>7. Control Strategies . . . . .</b>	<b>48</b>
7.1. Single-medium multirotor controller: Hierarchical PID . . . . .	49
7.1.1. Simulations in a single medium: Water . . . . .	53
7.1.2. Experiments in a single medium: Water . . . . .	56
7.2. Coupling discrete-continuous dynamics: Hybrid controller . . . . .	57
7.2.1. Trajectory tracking for a single medium . . . . .	61
7.2.2. Transition strategy . . . . .	63
7.2.3. Hybrid controller . . . . .	64
7.2.4. Hybrid controller Simulation . . . . .	67

7.2.5. Hybrid Controller Experiments . . . . .	69
7.3. Improving response: Gain scheduling . . . . .	74
7.4. Improving maneuverability: Quaternion controller . . . . .	76
7.4.1. Background on Quaternions . . . . .	81
7.4.2. Quaternion Control Laws . . . . .	82
7.4.3. Quaternion Simulations: Aerial operation . . . . .	83
7.4.4. Quaternion Simulations: Underwater operation . . . . .	84
7.4.5. Quaternion Experiments . . . . .	87
<b>8. Conclusion . . . . .</b>	<b>97</b>
8.1. Future work . . . . .	98
<b>Bibliography . . . . .</b>	<b>99</b>
<b>A. Simulink Model Employing An Euler angle Controller . . . . .</b>	<b>104</b>
<b>B. Simulink Model Employing a Quaternion Controller . . . . .</b>	<b>105</b>

## List of Tables

6.1. Translational Drag Experimental Results . . . . .	47
7.1. Control gains underwater . . . . .	53
7.2. Experimental parameters. . . . .	70

## List of Figures

2.1.	Graphical depiction of the dual-plane transition strategy out of water for a single coaxial rotor assembly on a vehicle that is negatively buoyant.	7
2.2.	Graphical depiction of the dual-plane transition strategy into water for a single coaxial rotor assembly on a vehicle that is negatively buoyant or positively/neutrally buoyant. . . . .	8
2.3.	Untethered air/underwater multirotor prototype, NV1, performing the air-to-water and water-to-air transition . . . . .	10
3.1.	Components diagram of a multirotor showing a power system, propulsion system and logic system. . . . .	11
3.2.	Illustration of several of the commonly utilized multirotor vehicle configurations for aerial operation employing coaxial propulsion. . . . .	12
3.3.	Illustration of several of the commonly utilized multirotor vehicle configurations for aerial operation employing single-plane propulsion. . .	13
3.4.	Illustration of other possible vehicle configurations derived from the vehicle arrangements shown in Figure 3.3. . . . .	13
3.5.	A simple illustration of the main structural components of a four-arm multirotor vehicle . . . . .	14
3.6.	A breakdown of a standard three-phase brushless motor . . . . .	17
4.1.	Pictures of each of the six prototypes developed as a test platform. .	20
5.1.	Illustration of the Naviator-NV6 model highlighting the frames of reference and rotor locations. . . . .	25

5.2.	Free body diagram of the vehicle indicating each individual thrust and torque vector ( $\mathbf{T}_i$ and $\mathbf{Q}_i$ , respectively), the counter-torque directions and gravity vector $\mathbf{G}$ . . . . .	29
5.3.	Rendering of the simplified drag model used for the Naviator. . . . .	32
5.4.	Graphical aide to describe how the frontal area of the Naviator is decoupled into frontal area of the four spheres. . . . .	33
6.1.	Snapshot of the CAD model of the 5th iteration of the multi-medium vehicle prototype “Naviator”, the NV5. . . . .	36
6.2.	Picture of the data acquisition (DAQ) system developed for the purpose of quantifying Naviator power system properties. . . . .	37
6.3.	Illustration of the experimental setup for collecting data corresponding to the thrust produced by a pair of counter-rotating coaxial rotors. . . . .	38
6.4.	Picture of the experimental setup for collecting data corresponding to the thrust produced by a pair of counter-rotating coaxial rotors placed inside of a water channel. . . . .	38
6.5.	Thrust force surfaces constructed by permutating though the different possible combinations of bottom and top rotor throttle levels operating underwater. . . . .	39
6.6.	Dynamic thrust in water for a stream velocity of 0.32 m/s showcasing the highest rotor angular velocity achieved in the water channel. . . . .	40
6.7.	Aerial propulsion characteristics showing (a) the thrust force surface for different permutations of bottom and top rotor throttles during static operation in the air and (b) and accompanying thrust performance surface, which is an indication of efficiency. . . . .	41
6.8.	Thrust force surface for different top and bottom rotor speeds and the hover thrust plane with a dashed intersection line. . . . .	42
6.9.	Illustration of the experimental setup for determining the translational drag coefficient of the Naviator NV5 prototype. . . . .	43

6.10. Plots detailing the two-stage interpolating process by which the throttle outputs of the translational drag experiments get converted into a thrust force per arm. . . . .	44
6.11. Illustration of the forces acting on the vehicle (neglecting restoring forces since they are inconsequential for horizontal motion). . . . .	46
6.12. Frontal area for different pitch angles taken directly from the Naviator NV5 CAD model. . . . .	46
7.1. Block diagram of a standard hierarchical PID controller commonly used for multirotor vehicles in a single medium. . . . .	49
7.2. Euler angles and respective input reference angles of the vehicle over time as it conducts a figure 8 maneuver in simulation. . . . .	54
7.3. Euler angles and respective input reference angles of the vehicle over time as it conducts a figure 8 maneuver in simulation. . . . .	54
7.4. Position of the vehicle over time as it conducts a figure 8 maneuver in simulation. . . . .	55
7.5. Euler angles and respective input reference angles of the vehicle over time as it conducts a figure 8 maneuver in the field. . . . .	56
7.6. Altitude/Depth and respective input altitude reference of the vehicle over time as it conducts a figure 8 maneuver in the field. . . . .	56
7.7. Graphical aide to describe hybrid transition through the interface. . .	60
7.8. $x$ , $y$ and $z$ (from top to bottom) position during the mission. Three transitions take place at $0.27s$ , $27.08s$ and $50.80s$ . The darker (blue) area highlights when the vehicle is on underwater mode, and the white area represents air mode. . . . .	67
7.9. Orientation response (top three) and total thrust force (bottom) underwater and in air. Underwater movements require higher angular changes to overcome drag forces. . . . .	69

7.10. 3D representation of the mission. The vehicle starts close to the water (solid yellow cross mark), submerges immediately to $-2m$ , moves $2m$ first on $y$ then on $x$ , before emerging again to the air to displace $2m$ on $y$ then $x$ and go back underwater. The darker (green) planes signal the boundaries of the transition zone, while the shaded (blue) volume represents the water. . . . .	70
7.11. Real-time experiment on altitude. The vehicle hovers at an altitude of $2.5m$ for $15s$ , descends at a rate of $10cm/s$ until it reaches the water level, transitions into the water, then it sinks until it approaches the depth reference of $0.5m$ and maintains the desired depth for $15s$ . . .	71
7.12. Throttle percentage output during the autonomous mission into water.	72
7.13. Orientation during the experiment into the water. . . . .	72
7.14. Real-time experiment on altitude. The vehicle starts $1m$ underwater, goes to $0.5m$ , goes to $0m$ , proceeds to transition out of the water, and goes to a reference of $0.5m$ . . . . .	73
7.15. Throttle percentage output during the autonomous mission out of water.	73
7.16. Orientation during the experiment out of the water. . . . .	75
7.17. Block diagram showing the architecture of how gain scheduling could be applied to a multi-medium vehicle. . . . .	75
7.18. Two plots of demonstrating the singularity problem of Euler angles for a reference $\theta = 90^\circ$ . . . . .	78
7.19. Example of a typical mission with pitch angle limited to $< 90^\circ$ . . . .	79
7.20. Example of a typical mission without pitch angle limit. . . . .	79
7.21. Trajectory tracking position in air. Real vs desired position (top). The position errors (bottom) quickly converge to zero and remain well bounded. . . . .	84



7.22. Trajectory tracking attitude in air. The desired orientation is provided by the position controller. The attitude (top) remains mostly close to the origin to compensate gravity. The attitude errors (bottom) quickly converge to the origin and stay close to zero. . . . .	85
7.23. Trajectory tracking control inputs in air. The thrust force (top) is used mainly to compensate for gravity. Small changes in the torques inputs (bottom) produce significant motions of the vehicle in air. . . . .	86
7.24. 3D visualization of the trajectory tracking in air. The desired trajectory consists of a spiral with $4m$ amplitude and $20s$ period. The vehicle is able to follow the spiral trajectory with good performance. . . . .	87
7.25. Trajectory tracking position underwater. Real vs desired position (top). The position errors (bottom) remain bounded, but the increased drag force underwater slows down the system response, resulting in larger errors. . . . .	88
7.26. Trajectory tracking attitude underwater. The desired orientation is provided by the position controller. Due to the increased drag and buoyancy forces underwater, the thrust force must be pointed in the direction of motion, hence, more aggressive orientations are commanded (top). The attitude errors (bottom) quickly converge to the origin and remain well bounded. . . . .	89
7.27. Trajectory tracking control inputs underwater. In order to overcome the larger drag force and keep track of the desired position, the thrust force (top) is saturated to its maximum and oriented in the direction of motion. Torques inputs (bottom). . . . .	90

7.28. 3D visualization of the trajectory tracking underwater. The desired trajectory consists of a spiral with $4m$ amplitude and $50s$ period. The larger drag force underwater acts as a natural damper to the system, hindering the motion of the vehicle. Henceforth, only slower trajectories are accomplished underwater. . . . .	91
7.29. An illustration of the mission conducted experimentally showing the Naviator conducting a vertical loop underwater. . . . .	92
7.30. The input quaternion references throughout the underwater vertical loop mission showing the value of each Euler parameter over time. . .	93
7.31. The value of the pitch angle throughout the underwater vertical loop mission obtained from converting the Euler parameters in Figure 7.30 to Euler angle where throughout the mission, the roll and yaw references are zero. . . . .	93
7.32. Experimental platform "Naviator" performing a flip maneuver underwater, shown approaching a forward pitch of $45^\circ$ in (a), $90^\circ$ in (b) and $180^\circ$ in (c). . . . .	94
7.33. Plots of the desired quaternion Euler parameters, actual Euler parameters and the quaternion error for a mission of a vertical loop underwater similar to the experiment, using a quaternion controller. . . . .	95
7.34. Plot of the path obtained for a mission of a vertical loop underwater similar to the experiment, using a quaternion controller. . . . .	95
7.35. Plot of the desired pitch angle references and pitch angle response for a mission of a vertical loop underwater similar to the experiment, using an Euler angle controller. . . . .	96
7.36. Plot of the path obtained for a mission of a vertical loop underwater similar to the experiment, using an Euler angle controller. . . . .	96
A.1. Snapshot of the outermost layer of the Simulink model created to model the Euler angle controller on a multi-medium vehicle. . . . .	104

B.1. Snapshot of the outermost layer of the Simulink model created to model the quaternion controller on a multi-medium vehicle. . . . .	105
---	-----

# Chapter 1

## Introduction

There have been great strides in the development of unmanned systems in recent years, particularly with regard to Unmanned Aerial Vehicles (UAV) as it is an area that has exciting applications and could benefit from a variety of improvements. Another segment that has seen an abundance of innovation recently is Unmanned Underwater Vehicles (UUV). But, they are normally studied separately and designed with a high degree of specialization to the corresponding medium. There is much to gain from the assimilation of these two disciplines into one that encompasses multiple mediums.

### 1.1 Motivation and goals

Bridging the efforts made in UAV and UUV to present a vehicle that is capable of both aerial and underwater (UW) navigation is of interest. Benefits include rapid deployment for both air/underwater missions (ie. search/rescue), point-to-point underwater (UW) mapping and object recognition without needing to consistently overcome opposite water currents. Such a vehicle would also serve as a multipurpose extreme weather vehicle since it is completely waterproof, perfectly adapted for rain, and recoverable by air if driven into a body of water. It is not surprising to note that this subject is not new but a revisited one, as it was tried in the past, at least conceptually, by the Soviet Union [36] during the last world war and has been of interest to DARPA in the last decade [9]. Unfortunately, however, former approaches to the

issue were far too costly or impractical to be of any real use.

## **1.2 Review of multirotor vehicles**

Of the many Unmanned Aerial Systems (UAS), one type drawing special attention is of the multirotor class, due to its robustness, reliability and practicality. Multirotors are vertical take-off and landing vehicles (VTOL) that do not require variable pitch propulsion systems and, although under-actuated, can easily compensate for irregular mass concentrations of payload. Research efforts in this area include improving the vehicle control strategy and optimizing the overall system as well as investigating different multirotor configurations [23]. As the UAV market expands together with new well-defined government regulations, industry has joined the race and multirotors are becoming smarter and more reliable vehicles. After all, if they are to be commercialized, they must be capable of safely interacting with people and objects alike.

## **1.3 Review of underwater vehicles**

The underwater research community also has a favorite, the Remotely Operated underwater Vehicles (ROV), which have been in use since the 1950s and are still used today [3]. One novelty as of late with regard to UUV has been the development of autonomous underwater vehicles capable of long term deployment, chiefly for data collection and underwater mapping. Underwater gliders have been successful in achieving this objective, with some gliders capable of operations lasting over one year [46].

## 1.4 Review of multi-medium vehicles

Unmanned aerial-underwater systems are a new class of unmanned vehicles having new capabilities. Efforts have been made to merge the capabilities of aerial and underwater systems, such as the AquaMAV that dives into the water [40]. Other approaches include submersible airplanes [12, 11] and launching an UAV out of the water [22, 31], but without the possibility of vehicle retrieval. The first buoyancy-based multi-medium vehicle has been the Naviator developed by Rutgers University and in years that followed, three other groups working with buoyancy-based multi-rotor multi-medium vehicles have surfaced, making it a total of four buoyancy-based multi-medium vehicles at the time that this was written.

**Buoyancy-based Naviator by Rutgers University** At Rutgers University, a team developed a buoyancy based multi-medium vehicle during the 2012-13 academic year. The “Naviator”, as the team called the vehicle, used an inflatable bladder to raise the rotors above the air-water interface so that it could pull the vehicle into the air.

**Cracuns by Johns Hopkins University** The Cracuns is a quadcopter multi-medium vehicle developed by the Johns Hopkins University Applied Physics Laboratory in Laurel, Maryland. It is designed to stay dormant underwater in the long-term until it is needed, at which point it floats to the surface so that it can take off from the water. The team focused primarily on sealing water-sensitive components and corrosion resistance. No underwater maneuverability is evident [18].

**Loon Copter by Oakland University** The Loon Copter is a quadcopter multi-medium vehicle developed by the Oakland University Embedded Systems Research Laboratory. The vehicle employs a buoyancy engine for both orientation change and

to transition in and out of the water. The vehicle is also capable of some underwater maneuvers. However, they are limited to just below the surface of the water since the vehicle is strictly controlled by radio frequency signals, which cannot penetrate very deep into the water [37].

**GTQ-Cormorant by Georgia Institute of Technology** The GTQ-Cormorant is a quadcopter multi-medium vehicle developed by the Georgia Tech UAV Research Facility. The vehicle employs a buoyancy engine in order to transition in and out of the water. There is no apparent underwater maneuverability [4].

**Buoyancy independent transition** In later prototypes, the Naviator evolved away from transition assisted by a buoyancy engine to a propulsion system that does not require supplemental transition aides (see Chapter 2). Although the Naviator is the only coaxial multi-medium multirotor vehicle in existence upon its manufacture and even to date, there is another vehicle concept worth mentioning. In 2014, a group based in Brazil published a conference paper on a multirotor vehicle concept that employs four arms, each comprising of one aerial propeller on the top and water propeller on the bottom [10]. The top and bottom propulsion systems are co-axially arranged and are medium specific, meaning that the top propellers are for aerial use only and the bottom propellers are for underwater use only. To date, there is no evidence of such a vehicle being built. Nevertheless, it would be interesting to see how this system compares with the Naviator if it were ever developed, the Naviator would have the upper hand due to the underwater propulsion system becoming payload once their vehicle is airborne.

## 1.5 The challenge and objective

Unmanned multi-medium vehicles are a new paradigm in unmanned systems and multirotors are a great candidate for this space. However, there is very little use for a multi-medium vehicle that is not capable of navigating freely within one of its mediums. It is revealed in Section 1.4 that not only are there few implementations of such vehicles, but that they lack underwater maneuverability. Whereas some are only capable of traveling up and down, others are depth limited by radio frequency water penetration. Furthermore, considering that multirotors are often used to carry unknown payloads, it becomes obvious that a buoyancy engine is unsuitable for variable payloads. The main objective of the present work is to push the limits of multi-medium multirotor vehicles with a focus on extending underwater maneuverability through the implementation of singularity-free attitude representations and control strategies.



## Chapter 2

### Multi-Medium Transition for multirotor vehicles

Prior to considering design specifications and maneuverability of a multi-medium multirotor vehicle, it is necessary to first decide on a method that will enable the vehicle to traverse between mediums. Chapter 1 describes some buoyancy-dependent mechanisms to facilitate transition between air and water. However, multirotors are often used as a versatile and mechanically simple aircraft that are capable of lifting a variety of payloads, which poses a serious challenge for buoyancy engine systems that are typically constrained by fluid displacement volume and in the case of aerial vehicles, limited by weight. Buoyancy engine systems are not lightweight and become heavier if they need to operate at high depths, typically involving pump driven fluid displacement using mechanisms such as ballscrews. Additionally, the fluid displacement necessary to compensate for a given payload needs to be considered. Employing a buoyancy engine that is large enough to handle any payload size that the multirotor vehicle can handle is cumbersome and will undoubtedly decrease the payload capacity that the vehicle originally had. Lastly, while utilizing a buoyancy engine is an efficient path toward depth control underwater, it is by no means the fastest or most reliable and should instead be a payload attachment if there is a need. Whereas most multi-medium multirotor vehicles rely on buoyancy to assist with the transition in and out of different mediums, there is another approach that avoids the inherent issues associated with buoyancy engines—the multi-plane transition strategy.

## 2.1 Multi-plane transition strategy

For a multi-medium multirotor vehicle to function properly, first and foremost, it must be capable of transitioning in and out of each medium. While entering the water for a vehicle whose buoyancy is lower than its weight is trivial due to gravity, exiting from a denser fluid into lighter fluid such as air is much more difficult. The multi-plane transition strategy utilizes a very simple but effective mechanism to accomplish this without buoyancy engines—through the use of propulsion systems on different parallel planes with a separation gap. The idea behind this strategy is to ensure that there is enough thrust generation for all actuators at each moment during the transition. Consider the case of a vehicle with dual-plane propulsion as shown in Figure 2.1 entering an air domain from a water domain. As the vehicle ascends from water to air, it will go through five stages where (1) both planes of propulsion are in the water domain, (2) the upper plane is at the air-water interface and the lower plane is completely submerged in the water, (3) the upper plane is within the air domain and the lower plane is still in the water domain, (4) the upper plane is still in the air domain and the lower plane is at the air-water interface and (5) both planes of propulsion are in the air domain.

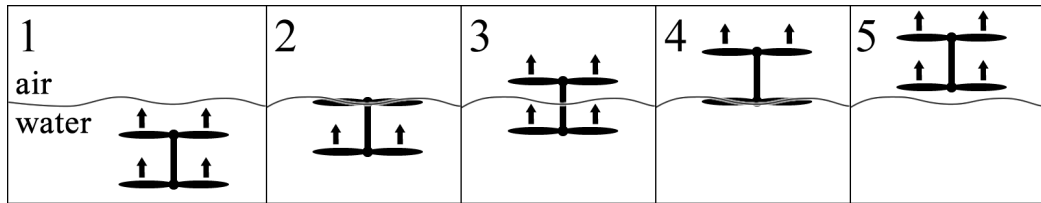


Figure 2.1: Graphical depiction of the dual-plane transition strategy out of water for a single coaxial rotor assembly on a vehicle that is negatively buoyant where the wavy line is the air-water interface showing (1) both of the rotors providing thrust in water, (2) the top rotor at the interface and the bottom rotor providing thrust in water, (3) the top rotor providing thrust in air and the bottom rotor providing thrust in water, (4) the top rotor providing thrust in the air and the bottom rotor at the interface and (5) both of the rotors providing thrust in air. The black arrows indicate actuation direction.

Due to the nature of the propulsion system, which consists of a rotor, thrust generation

at the air-water interface is unreliable and can add instability to the vehicle. However, through careful control of each rotor, it is possible to remove these instabilities and ensure a seamless transition. The full transition strategy out of the water for a multi-plane transition strategy of a negatively buoyant vehicle consisting of two planes is illustrated in Figure 2.1. The actuation of the rotors shown always point upward regardless of whether the vehicle is exiting the water or entering the water, which follows the same sequence in reverse. However, there are other scenarios to explore,

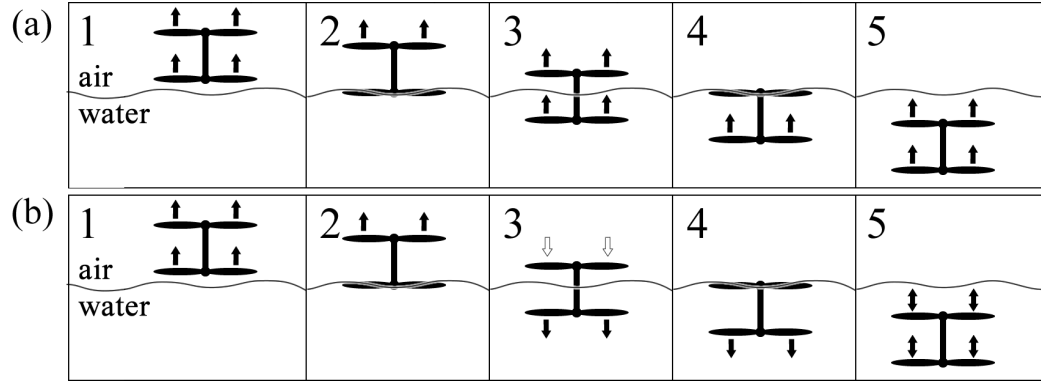


Figure 2.2: Graphical depiction of the dual-plane transition strategy into water for a single coaxial rotor assembly on a vehicle that is negatively buoyant in (a) or positively or neutrally buoyant in (b) both showing (1) both of the rotors providing thrust in air, (2) the bottom rotor at the interface and the top rotor providing thrust in air, (3) the top rotor providing thrust in air and the bottom rotor providing thrust in water, (4) the bottom rotor providing thrust in the water and the top rotor at the interface and (5) both of the rotors providing thrust in the water. The black arrows indicate actuation direction and the wavy line is the air-water interface. In the 3<sup>rd</sup> window in (b), the white arrows indicate an optional independent rotor control strategy to speed up transition but because low RPM underwater propulsion is less energy intensive, only operating the bottom rotors is ideal in this stage of transition. In the 5<sup>th</sup> window in (b), the double arrow indicates that upon transition, the top and bottom rotors are free to provide actuation in either direction, depending on the mission.

such as that of a positively buoyant or neutrally buoyant vehicle. In such a case, it becomes necessary for the rotors to provide both positive and negative actuation. Though variable pitch propellers are optimal for this scheme, they are heavier than fixed pitch propellers, are more complex, require additional components and thus may not survive well underwater and during transition. An alternative is to operate

rotors capable of spinning in reverse as well, thus providing the negative actuation necessary to pull a positively buoyant vehicle into the water or in the case of neutral buoyancy, obtain enough depth to perform maneuvers to orient the vehicle in the direction of travel. An illustration of transition into the water is shown for a negatively buoyant vehicle in Figure 2.2(a) and for a positively or neutrally buoyant vehicle in Figure 2.2(b). Admittedly, most propellers are optimized to provide thrust in a single direction. However, since the operation of the vehicle with rotors reversed would be limited to simply reorienting the vehicle after which normal operation would resume, the inefficiency of reversed operation is acceptable since it is only a necessity during the transition into the water. Reversing rotor direction may also be used to increase maneuverability.

## 2.2 Dual-plane/Coaxial based transition

Soon after the development of the buoyancy based “Naviator”, a non-buoyancy based multi-medium multirotor vehicle was developed in December 2013 that inherited the “Naviator” name and employed the dual-plane transition strategy [30], which is a subset of the multi-plane transition strategy. Henceforth, the only two mediums considered will be air and water and further discussions will be limited to these mediums. However, the study may be extended to other mediums such as oil or gaseous atmospheres found in planets/moons of interest to NASA without loss of generality. Similarly, although the multi-plane transition strategy may involve more than two planes of propulsion, further discussions will be limited to a dual-plane propulsion system for simplicity. This platform technology able to transition in and out of water is used on all prototypes that followed. A full transition cycle is shown in Figure 2.3 highlighting states ( $a, b, c$ ) of Figure 2.1 for both transition into and out of the water. More details on the design of such a platform can be found in Chapter 3.

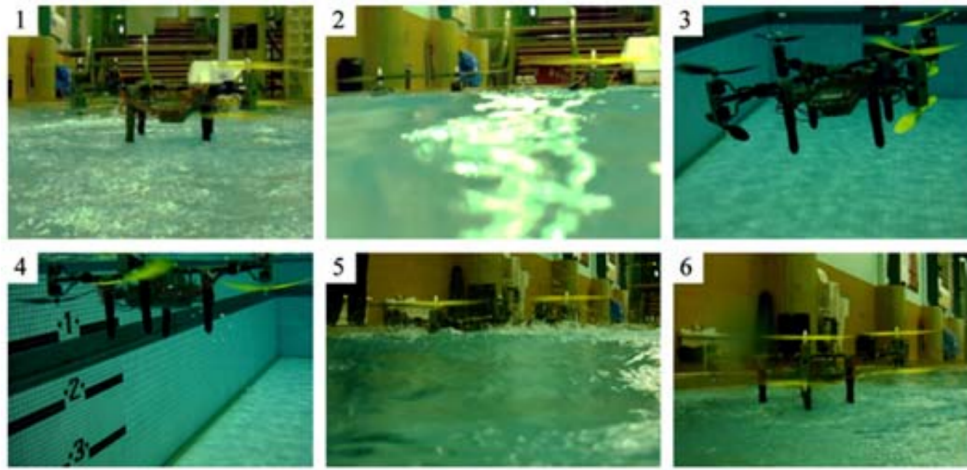


Figure 2.3: Untethered air/underwater multirotor prototype, NV1, performing the air-to-water transition (1-3) and the water-to-air transition (4-6).

## Chapter 3

### Design requirements of a multi-medium multirotor vehicle

Prior to studying and improving underwater agility, the vehicle must first be capable of smooth operation in both mediums. As shown in Figure 3.1, a typical aerial multirotor is composed of a power system, a propulsion system, and a logic system, all of which are also a core element of multi-medium multirotor vehicles. First and foremost, for the electronics to function, they must be protected from the elements. Furthermore, some of the hardware and firmware must be replaced or modified to allow for smooth operation in the air and underwater. The sections that follow will discuss some of the changes that a multi-medium multirotor vehicle employing dual-plane transition strategies must go through to function in both air and water.

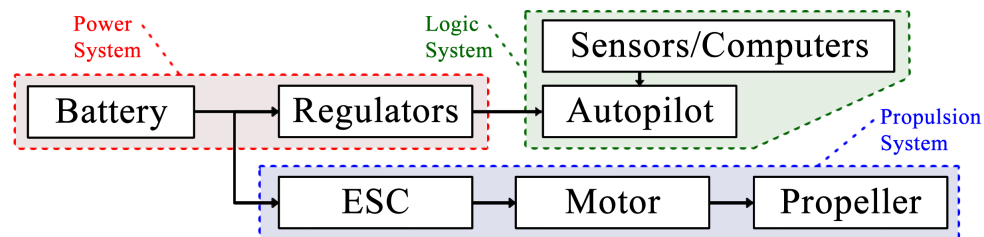


Figure 3.1: Components diagram of a multirotor showing a power system comprising of a battery and voltage regulators, a propulsion system consisting of an electronic speed controller (ESC), a motor and a propeller, and a logic system consisting of sensors, computers and autopilots.

### 3.1 Rotor Configuration

Before discussing the necessary changes for air and underwater operation, it is also important to highlight a benefit of utilizing a multirotor platform, which allow for a variety of rotor configurations (ie. the number of rotors and corresponding rotor placements). If the dual-plane propulsion is used, the configuration of the vehicle is very flexible. For instance, any coaxial multirotor configuration may be used by simply separating the planes of the upper rotors and bottom rotors, such as in the Hexa-rotor Y (Y6), Octo-rotor X (X8) or other coaxial multirotors (X12, X16, etc...).

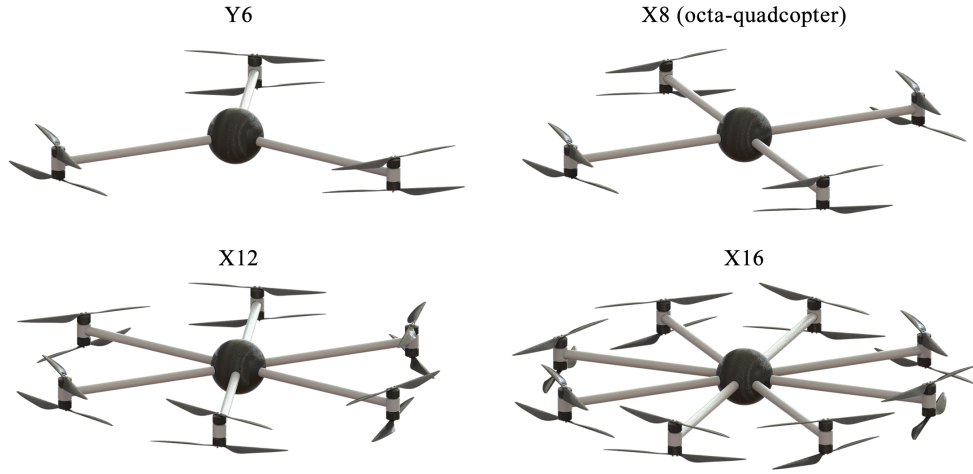


Figure 3.2: Illustration of several of the commonly utilized multirotor vehicle configurations for aerial operation employing coaxial propulsion.

Furthermore, any single plane multirotor arrangement with an even number of rotors such as the commonly used hexacopter shown in Figure 3.3 may be modified to apply the dual-plane propulsion strategy by offsetting half of the rotors to a parallel plane by some distance, as shown by the dual-plane HEXA X configuration in Figure 3.4. With less than six rotors, however, there will be loss of actuation during transition, which means that the vehicle may not be able to maintain a given attitude during the transition process. Lastly, any other combination of dual-plane rotors may be used as long as the vehicle does not lose actuation during the transition process. To demonstrate, consider the X8+4 configuration in Figure 3.4, where the OCTA X

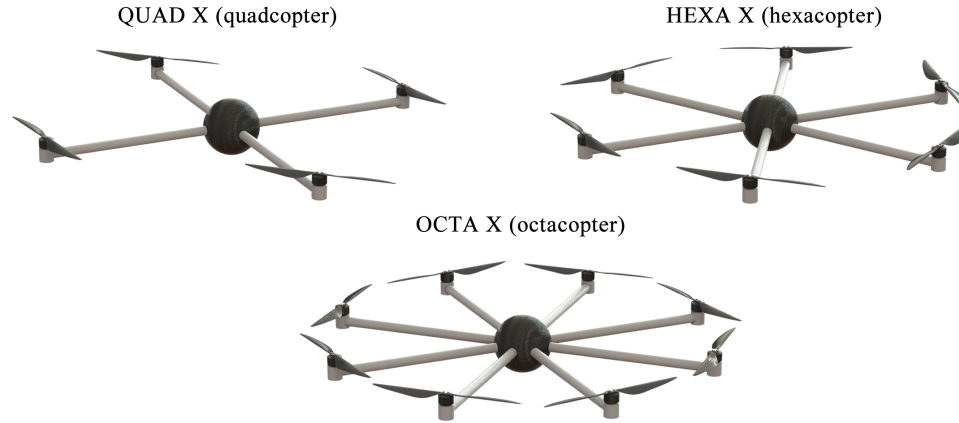


Figure 3.3: Illustration of several of the commonly utilized multirotor vehicle configurations for aerial operation showing the most popular configurations that can be found which consist of four to eight rotors on a single plane.

configuration is supplemented by four additional rotors on a lower plane arranged in the QUAD X configuration. When transitioning, the eight rotors on the top plane ensure full torque actuation as well as altitude control when the bottom rotors are at the interface and vice versa. The rotor arrangement selected for the Naviator and discussions moving forward is the X8 shown in Figure 3.2 due to its simplicity and symmetry.

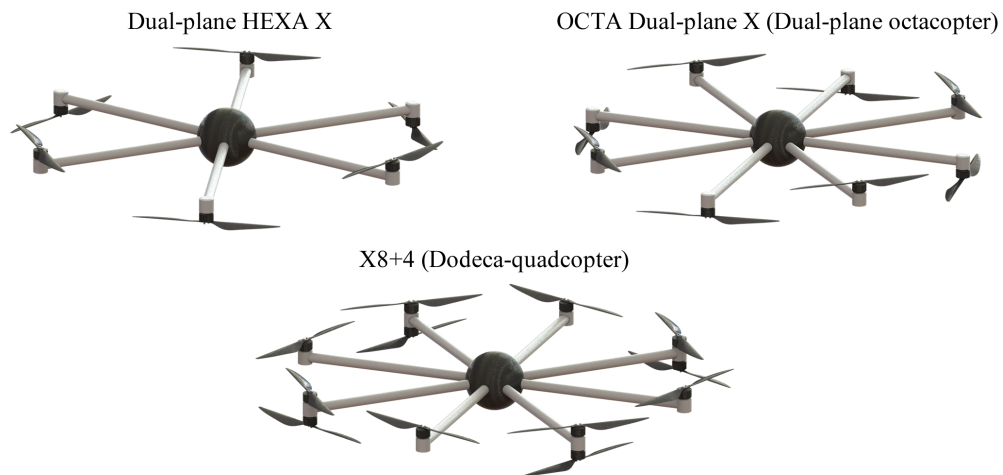


Figure 3.4: Illustration of other possible vehicle configurations derived from the vehicle arrangements shown in Figure 3.3 where a single-plane propulsion system is converted to a dual-plane propulsion system, thus allowing for seamless transition between air and water.



### 3.2 Structural construction and pressure vessel

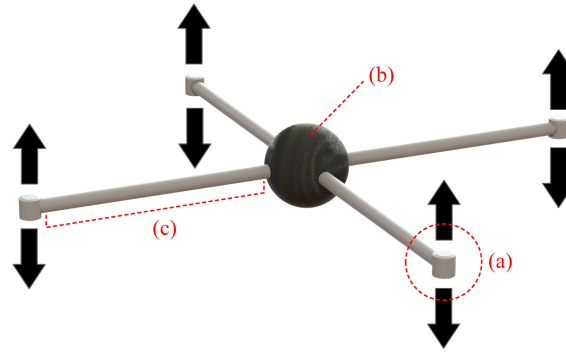


Figure 3.5: A simple illustration of the main structural components of a four-arm multirotor vehicle comprising of (a) actuators, (b) a central hub and (c) a structural bridge between the actuators and the central hub. The black arrows indicate an actuation axis.

Just as with any UAS, the vehicle must be capable of withstanding loads generated from its actuators, payloads, landing impact as well as any associated vibrations. To aid the present work, the methodology behind the vehicle structure and pressure vessel is briefly discussed for the frame of a standard four-arm multirotor in Figure 3.5 where a central hub, actuators and a structural bridge between the central hub and actuators can be seen.

**Structural bridge** One of the first steps in determining what structural components to use is to determine the bare vehicle weight before the structure is created. Toward this goal, the items generally considered include the battery, motors, propellers, electronics and electrical harnesses. Secondly, the actuator outputs must be determined and used to derive the maximum forces and moments that are exerted on the body other than forces due to gravity. From this, a structure that is strong enough to bridge the weight of the vehicle with the actuators can be determined. Revision G of The Handbook of Instructions for Airplane Design (HIAD) recommends a ultimate factor of safety of 1.5. In the case of the Naviator an ultimate factor of safety at or greater than 1.5 was used and the structural bridge was chosen to be a carbon fiber

tube arm of sufficient diameter and thickness. Carbon fiber tubes are a material of choice for many multirotor producers due to its strength to weight density.

**Central hub** In general, multirotors have a central hub to which all actuators connect through a structural bridge. This hub must be able to handle the forces and moments transferred from the actuators as well as impact during landing procedures. The landing gear is often attached to the central hub, although it is also commonly found attached to the structural bridge. In most cases, the central hub houses most of the logic circuits, including the autopilots, computers and sensors. It must be designed such that these components be kept safe from damage. In an aerial vehicle, it is sufficient to add a weather proof enclosure to keep these components away from the elements. For a multi-medium vehicle, the enclosure must be made waterproof and sensors that require access to the elements such as the altimeter/depth sensor must be routed from the inside to the outside of the enclosure. This waterproof enclosure must also be rated to a desired pressure and will henceforth be referred to as the pressure vessel. Several different types of enclosures as a pressure vessel were tested in each of the design iterations. These pressure vessels will be described in later sections and pictures of the pressure vessels on the vehicle during operation can be seen in Figure 4.1.

**Actuator** The actuators on a multirotor are the rotors. The two types of rotors used in multirotors are: (1) those that consist of a motor and a fixed pitch propeller and (2) those that consist of a motor, fixed pitch blades and a servo to actuate the pitch of the blades. The former is more common and selected for the Naviator due to its simplicity and reliability. Both types of rotors are driven by electronic speed controllers (ESC), which must also be waterproofed in a manner that allows them to dissipate heat. There are several ways of achieving this, such as applying a thermal waterproof coating or applying a non-thermal waterproof coating with a heat sink.

Since these methods are unproven, we opted to develop a waterproof metal enclosure for the ESCs that would serve three purposes. First, the enclosure will be a pressure vessel for the ESC. Second, by adhering the ESC to the metal enclosure through a thermal compound, it will become a heat sink through the enclosure itself. Third, the metal enclosure will also serve as a mounting point for the motors.

### **3.3 Propulsion system for multi-medium vehicles**

As mentioned in Section 3.2, the Naviator employs a rotor consisting of a motor and a fixed pitch propeller. Furthermore, it utilizes the same rotor for operation in the air and underwater, where the fluid density and viscosity differ by three orders of magnitude and one order of magnitude, respectively. These differences in medium properties result in vastly different RPM ranges of rotor angular velocities. For the Naviator, the operational RPM may reach up to 1,000 to 10,000 in the air and 1 to 500 in the water. Consequently, standard multirotor ESCs are not adequate for operation multiple mediums due to their inability to operate at drastically different angular velocities, which hinders vehicle maneuverability.

#### **3.3.1 Motors and Electronic Speed Controllers (ESC)**

There are two types of motors used in multirotors: brushed and brushless. Brushless motors are more efficient and durable, but require more sophisticated ESC drivers. For multirotors with frames that can fit within an 8" diameter (ie. 200mm class, or lower), both brushed and brushless motors can be found. However, for multirotors at a higher class, strictly brushless motors are utilized. Whereas motor commutation is done automatically by the brushed motor mechanism, brushless motors must be pulsed in a very specific manner in order to rotate. There are many different types of brushless motors as well, but when it comes to multirotors, the three-phase brushless

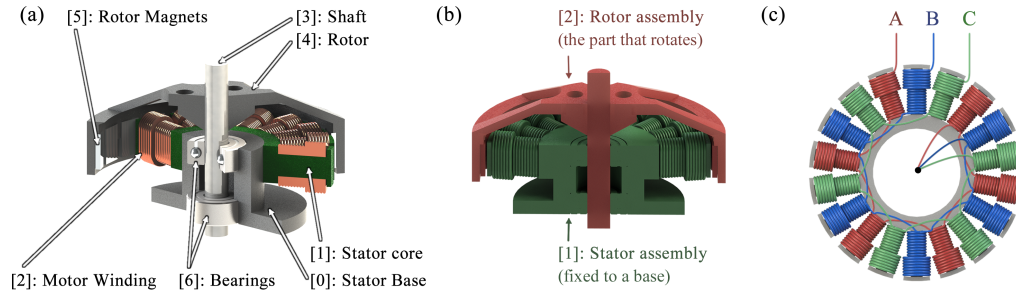


Figure 3.6: A breakdown of a standard three-phase brushless motor showing (a) a section view of the motor labeling all components to put the motor assembly into perspective, (b) the rotor assembly in red and the stator assembly in green to point out which parts are stationary and which parts rotate together and (c) a wiring diagram for how each of the channels  $\{A, B, C\}$  are routed through and around the stator core where the black dot indicates the common node at which the ends of the windings for each channel connect to each other.

motors are the most common.

A complete assembly of a typical three-phase brushless motor is shown in Figure 3.6(a) and Figure 3.6(b). The assembly in green contains the stator core, which has insulated electrical wires wound around it forming several electromagnets whose groupings can be seen in Figure 3.6(c). The rotor assembly shown in red contains many permanent magnets along its inner perimeter as shown in item 5 of Figure 3.6(a). When current is driven through the electromagnets of the stator, a magnetic field is induced which reacts with the already present magnetic field of the permanent magnets to align the rotor relative to the stator in a specific way. In order to pulse these three-phase motors correctly for continuous rotation, the driver must know the current position of the rotor relative to the stator. This fact divides the brushless motor category into sensed and sensorless three-phase brushless motors. Most multirotors, including the Naviator, employ sensorless brushless motors and obtain rotor position information from the electromotive force that is generated from rotating the permanent magnets around inactive electromagnets on the stator. For instance, if an electromotive potential is applied between channels  $A$  and  $B$  to activate the electromagnets shown in red and blue in Figure 3.6(c) thus incrementing through the

commutation cycle, then channel  $C$  can be used to detect the electromotive force that is fed back, called the counter-electromotive force (CEMF). The CEMF can then be used to determine when to next commutate the motor further.

### 3.4 Autopilot system and basic sensors for multi-medium vehicles

The logic circuit responsible for fusing the sensor data and controlling the attitude and position of a multirotor is called an Autopilot. There are countless autopilots in use, but not all are user/research friendly. In order to modify or replace control strategies on a multirotor, the autopilot must be reprogrammed, which is much easier to do when the source code is available. There are several open source autopilot firmwares and the ArduCopter (AC) firmware by DIY Drones was selected as the building block for further Naviator development. The AC firmware is primarily written for the AutoPilot Mega (APM, versions 1 and 2) and more recently, the Pixhawk. The APM2 was chosen as the primary autopilot platform due to its simpler code base. Before diving deeper into control strategies, there are some basic changes that needed to be programmed into the firmware that would allow the autopilot to function for a multi-medium multirotor vehicle.

**Altitude and depth** The APM2 is equipped with a gyroscope, accelerometer, barometer and temperature sensor. The temperature and pressure sensors are used to determine altitude from exterior air properties. Since a multi-medium multirotor vehicle autopilot is inside a waterproof enclosure, the sensor needs to be replaced with one that could be exposed to the elements and routed from the exterior of the pressure vessel to the autopilot. Furthermore, the firmware needs to be updated to properly handle the new sensor and make use of both altitude and depth data.

**Water sensors** When transitioning in and out of water, the altitude/depth sensor is not precise enough to indicate which medium the planes of propulsion are. Therefore, a simple solution is to incorporate water sensors along the height of the vehicle to determine which medium the rotors are in.

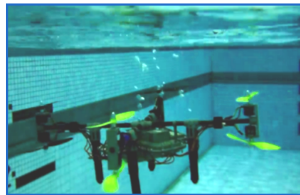
**Independent rotor control** Lastly, since multi-medium multirotor vehicles may, at a given instant, need to operate the different rotors in different mediums, there needs to be a way to tell the autopilot whether the rotor should be in air mode or in water mode so that it can output the correct signal to the ESC (see the discussion from Section 3.3.1).

## Chapter 4

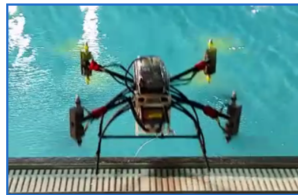
### Design iterations of a multi-medium multirotor vehicle

Following the design requirements set forth in Chapter 3, six iterations of the multi-medium multirotor vehicle known as the “Naviator” were developed, each taking a stride forward toward a reliable test platform that could take full advantage of new control algorithms tailored specifically for multi-medium operation. In this chapter, the purpose of each of the prototypes will be described and their contribution toward high maneuverability will be highlighted. Briefly, improvements include the extension of underwater rotor angular velocities to a higher range, the addition of sensors capable of operating in multiple mediums, high heat dissipation, and better overall construction. A picture of each of the six prototypes can be seen in Figure 4.1.

NV1



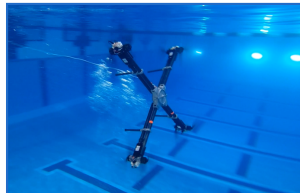
NV2



NV3



NV4



NV5



NV6



Figure 4.1: Pictures of each of the six prototypes developed as a test platform.

## **4.1 Naviator-NV1: Proof of concept**

### **Achieving air-water and water-air transition**

The NV1 was the very first prototype employing the dual-plane propulsion system and was used to demonstrate seamless transition in and out of the water, as seen in Figure 2.3. Its relevant hardware comprised of the APM2 and a 72MHz transmitter/receiver, which allowed the vehicle to be controlled without a tether for up to a few feet underwater. All sensitive electronics, including the ESCs, were enclosed in a rapid prototype acrylic pressure vessel.

This prototype was made to be slightly heavier than the mass of its water displacement and so, in the absence of actuation, it descends into the water. It was not capable of any complex maneuver since rotor speeds underwater could not be brought low enough for an underwater hover. Instead, the rotor system had such a small resolution of thrust output that as soon as any non-zero throttle was provided, the vehicle shot up into an ascent. Of course being the first prototype, the NV1 was not equipped with sensors capable of providing depth but if it had been, in order to keep it at a given depth, the scheme would resemble an on-off controller, which is the simplest form of feedback control.

## **4.2 Naviator-NV2: Higher depth range**

### **Going beyond air-water and water-air transition**

To study maneuverability underwater, the controller behavior needed to be tuned and capable of operating further than just a few feet deep. Toward that end, three things were done:

1. To allow quicker access to the autopilot for tuning and configuring purposes, a two COTS waterproof cases were used as pressure vessels—one for the logic



circuits and one for the power system (battery and ESC).

2. A tether out of phone cable was used to send pilot commands to the autopilot and for telemetry.
3. The radio transmitter was updated to a 2.4GHz type to allow for more than six pilot inputs, thus allowing for more complex manual tests.

With these changes, the vehicle was capable of entering the water, pitching forward and traversing through the water before transition back out to air. However, an issue with the NV2 is that even upon completion of autopilot tuning of the proportional-integral-derivative (PID) controllers built-in to the autopilot, notable jitters could be observed as it traveled underwater. This anomaly is due to the ESC's inability to commutate the rotor properly. We observed that periodically, the speed controller would lose commutation and reboot, thus causing the jitters.

### **4.3 Naviator-NV3: Enabling low UW rotor speeds**

#### **Introducing the hybrid ESC firmware "HESC"**

Until this prototype, no work had been done toward smooth rotor operation underwater. The NV3 was designed with ESC firmware upgrade in mind and therefore employed speed controllers whose hardware was capable of adapting open-source AVR Assembly code, parts of which could be rewritten and amended. The firmware in the ESC was modified to have two modes: air and water. In the air mode, it operates as a normal multicopter (rotor speeds of 1000 to 10000 RPM) and in water mode, it is able to precisely control the rotor at low speeds (1 to 1000 RPM).

## 4.4 Naviator-NV4: Maximizing high UW rotor speeds

### A short study on UW closed-loop ESC performace

The NV4 is perhaps the most unique prototype that was built due to the fact that the vehicle batteries are distributed throughout the inside of the carbon fiber arms of the vehicle in a modular fashion. It is very lean and was meant to be a skeleton for an aero/hydrodynamic outer shell. The larger size when compared to its predecessors and good performance during real-time tests highlight that the platform has scalability. However, its main contribution comes from a brief ESC study in which over a dozen speed controllers were tested underwater in several scenarios to qualitatively rank them in terms of smooth underwater performance and maximum achievable rotor speed. The highest performing speed controller was deployed for use in this vehicle and vehicle speed experiments showed a top speed of 3.24 knots. This vehicle was also featured in a National Geographic episode “Man V. Machine” of a show titled “Machine Impossible”.

## 4.5 Naviator-NV5: Control strategy test platform

The NV5 prototype incorporates all lessons learned through its predecessors and is meant to finally be a platform ready for control strategy implementation. It employs the tether of the NV2, the HESC firmware of NV3, the ESC of NV4 and also contains sensors not previously implemented, such as the altitude/depth sensor and the water sensors. It was used to test the majority of the custom autopilot firmware, including new attitude representations, control strategies and predefined autonomous missions.

## **4.6 Naviator-NV6: A stronger, smarter vehicle**

### **Metal construction and additional sensors**

The NV6 is meant to be a replacement for the NV5 with a metal construction instead of plastic, greater payload and broader variety of sensors. The goal is to have a more robust vehicle that is smarter and more capable.

## Chapter 5

### Dynamic Model of a multi-medium multirotor vehicle

Before discussing control strategies that will render the vehicle more maneuverable, the vehicle's dynamic model must be established, which will be based on the X8 multirotor configuration (the same platform adopted by the Naviator). Common ways to obtain the dynamic model of a multirotor include using the Euler-Lagrange or Newton-Euler formalism. The latter will be used to achieve a more intuitive way of looking at the forces and moments.

The configuration of the Naviator is that of an octa-quadcopter, which consists of four pairs of coaxial rotors—eight rotors total. They are orthogonal to the  $\hat{\mathbf{b}}_3$  axis with

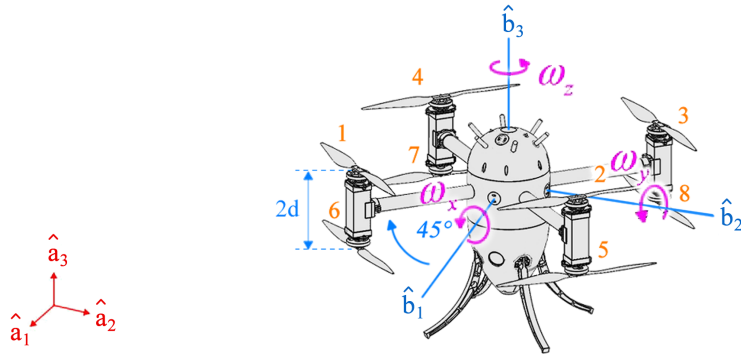


Figure 5.1: Illustration of the Naviator-NV6 model highlighting the frames of reference  $A$  with position vector  $X\hat{\mathbf{a}}_1 + Y\hat{\mathbf{a}}_2 + Z\hat{\mathbf{a}}_3$  (inertial) and  $B$  with position vector  $x\hat{\mathbf{b}}_1 + y\hat{\mathbf{b}}_2 + z\hat{\mathbf{b}}_3$  (body) as well as the right-hand convention for positive rotations, rotor locations comprising of a rotor planar gap distance  $2d$ , the angle to the first rotor, and the rotor indices.

the first rotor pair  $-45^\circ$  from the  $\hat{\mathbf{b}}_1$  axis. This arrangement is shown in Figure 5.1, which also describes the number index for each of the motors. The rotors' direction of rotation alternates from counter-clockwise (CCW) to clockwise (CW) as the indices increase, beginning with CCW on rotor 1. The top rotors lie on the plane offset a distance  $d$  from the  $xy$ -plane and the bottom rotors lie on the plane offset a distance  $-d$  from the  $xy$ -plane.

Although the multi-plane transition discussed in Chapter 2 applies to many different configurations, further discussion will be limited to the X8 rotor configuration as shown in Figure 3.2. The illustration of the vehicle model with the frames of reference, rotor indices and rotor locations shown in Figure 5.1 will be used for all further analysis and discussions.

## 5.1 Frames of reference

The inertial or Earth fixed frame  $A$  is the Cartesian coordinate frame in Euclidean space with unit vectors  $\hat{\mathbf{a}}_1$ ,  $\hat{\mathbf{a}}_2$ , and  $\hat{\mathbf{a}}_3$ , respectively, where the position variables are  $X$ ,  $Y$  and  $Z$ . The body frame  $B$  coordinate system is coincident with the center of mass (COM) of the vehicle and is the Cartesian coordinate frame in Euclidean space with unit vectors  $\hat{\mathbf{b}}_1$ ,  $\hat{\mathbf{b}}_2$ , and  $\hat{\mathbf{b}}_3$ , respectively, where the position variables are  $x$ ,  $y$  and  $z$  (lowercase). Moreover, the gravitational field will be taken to be uniform such that the COM aligns with the center of gravity (COG). The vehicle model is depicted in Figure 5.1(a) with the corresponding frames of reference.

## 5.2 Dynamic model for aerial multirotors

Before determining choosing a formalism for the dynamic model, it is necessary to examine whether or not effects planetary rotation are large compared to the rotations

of the vehicle and associated fluid. For that purpose, the Rossby number [39]

$$Ro = \frac{U}{Lf} \quad (5.1)$$

is used, where  $U$  is the characteristic velocity,  $L$  is the characteristic length,  $f = 2\Omega \sin \varphi$  is the Coriolis frequency,  $\Omega$  is the planetary angular frequency and  $\varphi$  is the latitude geographic coordinate. Given that the rotation rate of the Earth is  $\Omega \approx 7.3 \times 10^{-5} \text{ rad/s}$  and that the latitude angle of New York City is  $\varphi \approx 40.7^\circ$ , the corresponding Coriolis frequency is  $f = 4.8 \times 10^{-5} \text{ rad/s}$  [43]. If characteristic speed is taken to be the velocity of the vehicle (0.1 m/s to 26 m/s) and the characteristic length is taken to be the vehicle range (tens of meters to a few kilometers), then the Rossby number ranges from  $Ro = 1$  and  $Ro = 5.4 \times 10^4$ , depending on the vehicle operation. However, in a lab environment where typical speeds are  $U = 10 \text{ m/s}$  in the air and  $U = 0.5 \text{ m/s}$  underwater with a range limited to  $L = 25\text{m}$ , the Rossby number lies between  $Ro = 4.2 \times 10^2$  and  $Ro = 8.3 \times 10^3$ . Since the Rossby number is high, the effects of planetary rotation and thus, the Coriolis force, may be neglected [39]. For simplicity, only the lab environment will be considered.

For the dynamic model, the Newton-Euler formalism with transnational dynamics relative to the inertial frame and rotational dynamics relative to the body frame is used,

$$\begin{bmatrix} m\mathbf{I}_{3 \times 3} & \mathbf{0} \\ \mathbf{0} & \mathbf{I}_{cm} \end{bmatrix} \begin{pmatrix} \dot{\mathbf{v}} \\ \dot{\boldsymbol{\omega}} \end{pmatrix} + \begin{pmatrix} \mathbf{0} \\ \boldsymbol{\omega} \times \mathbf{I}_{cm}\boldsymbol{\omega} \end{pmatrix} = \begin{pmatrix} \mathbf{F} \\ \boldsymbol{\tau} \end{pmatrix} \quad (5.2)$$

where  $m$  is the total mass of the vehicle,  $\mathbf{I}_{3 \times 3}$  is the identity matrix in  $\mathbb{R}^{3 \times 3}$ ,  $\mathbf{I}_{cm}$  is the inertia matrix for the vehicle about the center of mass,  $\mathbf{v}$  is the translational velocity of the center of mass in the inertial frame,  $\boldsymbol{\omega}$  is the angular velocity about the body frame axes,  $\mathbf{F}$  is the resultant forces vector on the system, and  $\boldsymbol{\tau}$  is the resultant moments vector.

For multirotors, the forces and moments are

$$\mathbf{F} = \mathbf{T} - \mathbf{G} \quad (5.3)$$

$$\boldsymbol{\tau} = \boldsymbol{\tau}_{xyz} \quad (5.4)$$

The standard forces considered in multirotors are gravity  $\mathbf{G}$  and the resultant forces and moments due to the rotor actuations ( $\mathbf{T}$  and  $\boldsymbol{\tau}_{xyz}$ , respectively). For multirotors that move at high speeds, drag is sometimes incorporated as well, although it is often ignored.

The combined thrust produced by each rotor is  $T_\Sigma$ , which acts in the direction of the body frame z-axis,  $\hat{\mathbf{b}}_3$ . Since an estimation of the position is desired, the forces on the body must be expressed in the inertial frame. Therefore, a transformation  $\mathbf{R}(\boldsymbol{\Phi})$  is applied which converts vectors from body frame to inertial frame, yielding

$$\mathbf{T} = T_\Sigma \hat{\mathbf{b}}_3 = T_\Sigma \mathbf{R}(\boldsymbol{\Phi}) \hat{\mathbf{a}}_3 \quad (5.5)$$

where  $\boldsymbol{\Phi}$  is the Euler angle vector consisting of roll  $\phi$ , pitch  $\theta$  and yaw  $\psi$ . Since gravity already acts along the inertial z-axis, it does not require a transformation and is given by

$$\mathbf{G} = mg \hat{\mathbf{a}}_3 \quad (5.6)$$

where  $m$  is the rigid body mass and  $g$  is the acceleration due to gravity. The thrust for each rotor in a single fluid medium,  $T_i$ , can be modeled as

$$T_i = K_T \varpi_i^2 \quad (5.7)$$

where  $K_T$  is a thrust factor mapping the rotor angular velocity squared  $\varpi_i^2$  to the thrust force. **The** total thrust can then be determined by the sum of every rotor

thrust  $\sum_{i=1}^8 T_i$ . Similarly, the torque is modeled in the same way as the thrust, but with a torque factor,  $K_Q$ . Since the torque correlates linearly with thrust, it is the thrust multiplied by a factor that maps thrust to torque,  $K_{QT}$ , and the counter-torque  $Q_i$  be simply defined as

$$Q_i = K_Q \varpi_i^2 = K_{QT} K_T \varpi_i^2 = K_{QT} T_i \quad (5.8)$$

where the counter-torque produced is negative if the rotor is spinning CCW and positive if the rotor is spinning CW. The individual forces and torques experienced by the vehicle are illustrated in Figure 5.2.

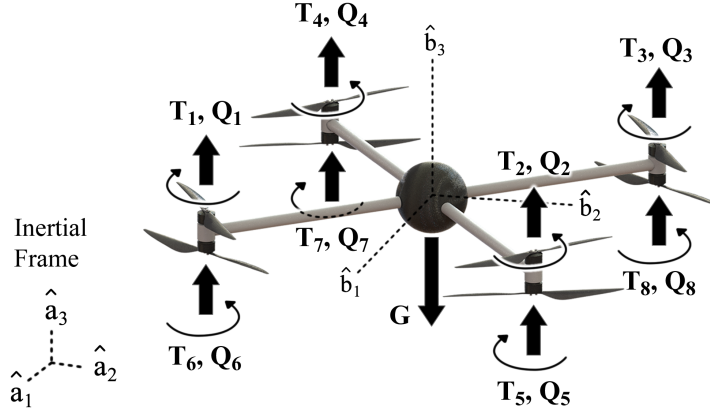


Figure 5.2: Free body diagram of the vehicle indicating each individual thrust and torque vector ( $\mathbf{T}_i$  and  $\mathbf{Q}_i$ , respectively), the counter-torque directions and gravity vector  $\mathbf{G}$ .

The vector defined by

$$\begin{bmatrix} T_\Sigma \\ \boldsymbol{\tau}_{xyz} \end{bmatrix} = \begin{bmatrix} \mathbf{1}_{1 \times 8} \\ \mathbf{C} \end{bmatrix} \begin{bmatrix} T_1 \\ \vdots \\ T_8 \end{bmatrix} \quad (5.9)$$

shows how the total thrust  $T_\Sigma$  and rotor induced torques  $\boldsymbol{\tau}_{xyz}$  are calculated for the Naviator vehicle, where  $\mathbf{C}$  describes the vehicle rotor configuration,  $\mathbf{1}_{1 \times q}$  is a column vector in  $\mathbb{R}^q$  containing ones and  $l$  is the moment arm for the rotor induced torques. The torques about the  $\hat{\mathbf{b}}_1$  and  $\hat{\mathbf{b}}_2$  axes are produced by the thrust acting on the



moment arms of the vehicle. The torque produced about the  $\hat{\mathbf{b}}_3$  axis is produced by the combined counter-torques of each rotor.

$$\mathbf{C} = \begin{bmatrix} -l & l & l & -l & l & -l & -l & l \\ -l & -l & l & l & -l & -l & l & l \\ -K_{QT} & K_{QT} & -K_{QT} & K_{QT} & -K_{QT} & K_{QT} & -K_{QT} & K_{QT} \end{bmatrix} \quad (5.10)$$

### 5.3 Dynamic model for multi-medium multirotors

The dynamic model for a multi-medium multirotor vehicle must comprise both aerial elements and underwater elements. Missing contributions to the dynamic model include those due to buoyancy, drag and added mass. Whereas the decision on whether or not to include contributions due to drag for aerial operation depend on discretion and type of application, it becomes a necessity for a vehicle that must operate underwater. Maneuverability is the topic of interest and for simplicity, further analysis will only consider buoyancy and drag, although a more general model which includes added mass can be found in [13]. Here, the buoyancy  $\mathbf{B}$ , translational drag forces  $\mathbf{F}_{Dv}$  and angular drag moments  $\mathbf{F}_{D\omega}$  will also be considered as external forces on the system

$$\mathbf{F} = \mathbf{T} - \mathbf{G} + \mathbf{B} - \mathbf{F}_{Dv} \quad (5.11)$$

and external torques

$$\boldsymbol{\tau} = -\mathbf{F}_{D\omega} + \boldsymbol{\tau}_{xyz} \quad (5.12)$$

where the thrust  $T$  and torque  $\boldsymbol{\tau}_{xyz}$  are dependent on the speeds of each rotor,  $\boldsymbol{\omega}_i$ .

#### 5.3.1 Buoyancy forces and moments

An assumption has been made stating that the body frame coordinate system deliberately coincides with the vehicle center of mass and although the vehicle may

be designed such that the center of buoyancy (COB) coincides with the COM, it is sometimes not the case. For instance, the COB may be chosen such that the vehicle always remains upright in the absence of forces other than those due to buoyancy and gravity. Such a selection could render the vehicle more stable. The buoyancy force itself is given from Archimedes' principle by  $\mathbf{B} = \rho V g \hat{\mathbf{K}}$  for a fluid with density  $\rho$  and rigid body with volume  $V$ . However, a partially submerged vehicle requires that the buoyancy  $\mathcal{B}$  be a function of position, attitude and density

$$\mathcal{B}(Z, \Phi, \rho) := \begin{cases} \rho_A V g & Z \geq h(\Phi) \\ \rho_W g \int_{Z-h(\Phi)}^0 A(\zeta, \Phi) d\zeta + \rho_A g \int_0^{Z+h(\Phi)} A(\zeta, \Phi) d\zeta & |Z| < h(\Phi) \\ \rho_W V g & Z \leq -h(\Phi) \end{cases} \quad (5.13)$$

where  $A(\zeta, \Phi) d\zeta$  is the infinitesimal volume displacement and  $h(\Phi)$  is half of the height of the vehicle, both at offset  $Z$  from water level.

### 5.3.2 Translational and angular drag forces

It is common for the drag on a multirotor to be neglected in the dynamic model and controls since they operate in the air, often at speeds lower than 40 mph [34]. However, since the Naviator also operates underwater, the drag forces and moments must be defined and compensated for, even at very low speeds. Typically, the total drag force in aerodynamics is modeled as [27]

$$F_D = \frac{1}{2} \rho U_\infty^2 C_D(\text{Re}) A \quad (5.14)$$

where  $U_\infty$  is the stream velocity,  $C_D$  is the coefficient of drag,  $A$  is the characteristic area,  $D$  is the characteristic length,  $\nu$  is the kinematic viscosity, and  $\mu$  is the dynamic

viscosity of the fluid medium and  $Re$  is the Reynolds number

$$Re = \frac{\rho \mathbf{v} \mathbf{D}}{\mu} = \frac{\mathbf{v} \mathbf{D}}{\nu} \quad (5.15)$$

Therefore, the drag force in  $\mathbb{R}^3$  can be defined as

$$\mathbf{F}_{\mathbf{D}\mathbf{v}} = \frac{1}{2} \rho \mathbf{A}_{\mathbf{v}} \mathbf{C}_{\mathbf{D}\mathbf{v}} \mathbf{v} \circ \mathbf{v} \circ \text{sgn}(\mathbf{v}) \quad (5.16)$$

where  $\mathbf{A}_{\mathbf{v}}$  is the characteristic area matrix of the vehicle for each plane defined by  $\text{diag}(A_{vx}, A_{vy}, A_{vz})$ ,  $\mathbf{C}_{\mathbf{D}\mathbf{v}}$  is the translational drag coefficient matrix defined by  $\text{diag}(C_{Dvx}, C_{Dvy}, C_{Dvz})$ ,  $\mathbf{v}$  is the relative velocity of the vehicle with respect to the fluid,  $\text{sgn}(\mathbf{v}_i) = \mathbf{v}_i/|\mathbf{v}_i|$  and  $\circ$  is the Hadamard product (i.e. element/entry-wise multiplication).

In the absence of a more accurate drag model, the vehicle drag model will be initially taken to be a set of perfectly smooth spheres as shown in Figure 5.3, where a 3-D rendering of the drag model is shown in (a) and a sketch depicting angular drag is shown in (b). Four spheres are used to represent the drag of the cylinder arms and rotors and a single sphere is used to represent the drag acting of the main pressure vessel at the central hub. The characteristic diameters of the spheres are chosen to be indicative of the actual frontal area of the vehicle, as shown in Figure 5.4, where the centroids of the areas are indicated by the symbol  $\bullet$ .

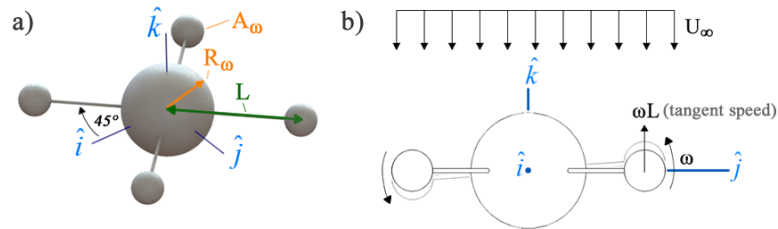


Figure 5.3: Rendering of the simplified drag model used for the Naviator showing (a) the central hub sphere and four outer spheres and (b) the angular velocities of the arms due to rotation for the purposes of highlighting angular drag contributions.

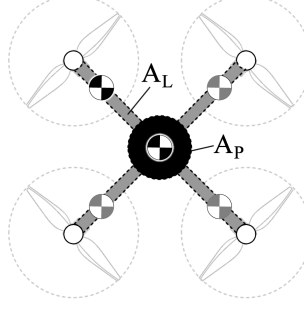


Figure 5.4: Graphical aide to describe how the frontal area of the Naviator is decoupled into the frontal areas of the five spheres in 5.3(a), where  $A_P$  (shown in black fill) is the frontal area for the main pressure vessel represented by the sphere at the central hub and  $A_L$  is the frontal area of each arm assembly (shown in gray fill) represented by each of the four outer spheres, where the center of the spheres coincide with the centroid of the frontal areas, which are indicated by  $\odot$ .

The moments produced by drag at the four spheres is given by

$$\mathbf{F}_{D\omega 1} = 4 \cdot \frac{1}{2} \rho A_\omega C_{D\omega} \omega L \circ \omega L \circ \text{sgn}(\omega) \cdot L \quad (5.17)$$

and viscous moments produced from drag due to the central hub sphere rotating in a fluid is given by [26]

$$\mathbf{F}_{D\omega 2} = 8\pi R_\Phi^3 \mu \omega \quad (5.18)$$

The total angular drag is therefore  $\mathbf{F}_{D\omega 1} + \mathbf{F}_{D\omega 2}$ .

After combining the resultant forces and moments into (5.11)-(5.12), they are expanded to (5.19) and (5.20).

$$\mathbf{F} = (T_\Sigma \mathbf{R}(\Phi) - mg + \mathcal{B}) \hat{\mathbf{b}}_3 - \mathbf{F}_{D\mathbf{v}} \quad (5.19)$$

$$\boldsymbol{\tau} = -\mathbf{F}_{D\omega} + \boldsymbol{\tau}_{xyz} \quad (5.20)$$

However, generating a link between actuator forces/moments and useful information, such as rotor speeds or ESC pulse-width modulation (PWM) inputs, remains to be done. The thrust produced by each rotor of index  $i$  is directly proportional to its

rotor angular velocity squared  $\varpi_i^2$  and can be modeled by (5.21), where  $K_{T_j}$  is a conversion factor that maps  $\rho\varpi_i^2$  to thrust with index  $j$  describing which medium the rotor is in (i.e.  $j \in \{ \text{A: air, W: water, } \dots \}$ ). Furthermore, the thrust and torque produced by a rotor are directly proportional to each other. Therefore, we can model the counter-torque of each rotor by applying another conversion factor from thrust to torque  $K_{QT_j}$ , resulting in the counter-torque shown in (5.22).

$$T_i = K_{T_j} \rho \varpi_i^2 \quad (5.21)$$

$$Q_i = K_{QT_j} K_{T_j} \rho \varpi_i^2 = K_{QT_j} T_i \quad (5.22)$$

Inserting these definitions into the equations of motion in (5.2), we obtain a complete dynamic model described by (5.23) through (5.26) where  $\mathbf{r}$  is the vehicle position vector and  $\mathbf{Q}(\Phi)$  is a transformation from Euler angle rates to body angular velocity.

$$\dot{\mathbf{r}} = \mathbf{v} \quad (5.23)$$

$$m\dot{\mathbf{v}} = (T_\Sigma \mathbf{R}(\Phi) - mg + \mathcal{B}) \hat{\mathbf{a}}_3 - \mathbf{F}_{\mathbf{D}\mathbf{r}} \quad (5.24)$$

$$\boldsymbol{\omega} = \mathbf{Q}(\Phi) \dot{\Phi} \quad (5.25)$$

$$\dot{\boldsymbol{\omega}} = [\mathbf{I}_{cm}]^{-1} (-\boldsymbol{\omega} \times \mathbf{I}_{cm} \boldsymbol{\omega} - \mathbf{F}_{\mathbf{D}\boldsymbol{\omega}} + \boldsymbol{\tau}_{xyz}) \quad (5.26)$$

Unlike unmanned systems with access to global positioning systems (GPS), the Navigator does not always have an accurate measure of position since the GPS satellite signals do not propagate through water when the vehicle is submerged. Fortunately, there are alternatives such as acoustic doppler velocimetry (ADV), ultra-short base-line systems (USBL, a method of underwater acoustic positioning) and other forms of acoustic triangulation (see [42]). Such systems are very costly and have properties not suited for a small scale vehicle due to weight requirements, communication speeds,

update rates and blind spots. Nevertheless, pressure and temperature sensors provide a reasonable indication of positioning along the inertial  $Z$ -axis,  $\hat{\mathbf{a}}_3$ . Therefore, we will proceed with the knowledge that positioning in the along  $\hat{\mathbf{a}}_1$  and  $\hat{\mathbf{a}}_2$  are unknown.

## Chapter 6

### Parameter Identification

Although the model of a multi-medium vehicle has been introduced in Chapter 5, the simulations that correspond to real-time experiments cannot be conducted until the dynamic model parameters are identified. This chapter will aim to declare key attributes corresponding to the Naviator prototype NV5, characterize its capabilities with regard to propulsion and also investigate drag.

#### 6.1 Mass, Volume and Moment of Inertia

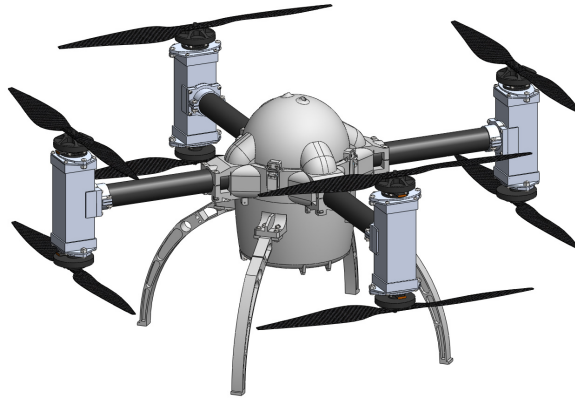


Figure 6.1: Snapshot of the CAD model of the 5th iteration of the multi-medium vehicle prototype “Naviator”, the NV5.

Vehicle geometry for the 5th iteration of the “Naviator” prototype is available in the SOLIDWORKS® powered computer aided design (CAD) model shown in Figure 6.1 with all mass and corresponding volumetric parts appropriately placed and distributed. Since the vehicle was designed to be negatively buoyant in order to allow

hovering underwater, the ready-to-fly mass of the vehicle without considering a tether was measured to be  $4.2\text{kg}$  ( $41.2\text{N}$  in air), which has a greater weight than that of the displaced water with corresponding volume of  $3.7\text{L}$  ( $36.3\text{N}$  of displaced water). The resultant restoring force (buoyancy minus gravity) yields a net buoyancy of  $-4.90\text{N}$ . Utilizing the mass properties tool available in the CAD software, the mass moment of inertia is found to be

$$\mathbf{I}_{cm} = \begin{bmatrix} 0.06906 & -0.00001 & 0.00000 \\ -0.00001 & 0.06929 & -0.00001 \\ 0.00000 & -0.00001 & 0.11896 \end{bmatrix} [kg-m^2] \quad (6.1)$$

where the symmetry of the vehicle is apparent in the nearly diagonal inertia matrix. It follows that the inertia matrix may be approximated by  $\mathbf{I}_{cm} \approx \text{diag}(0.069, 0.069, 0.119)$ .

## 6.2 Propulsion

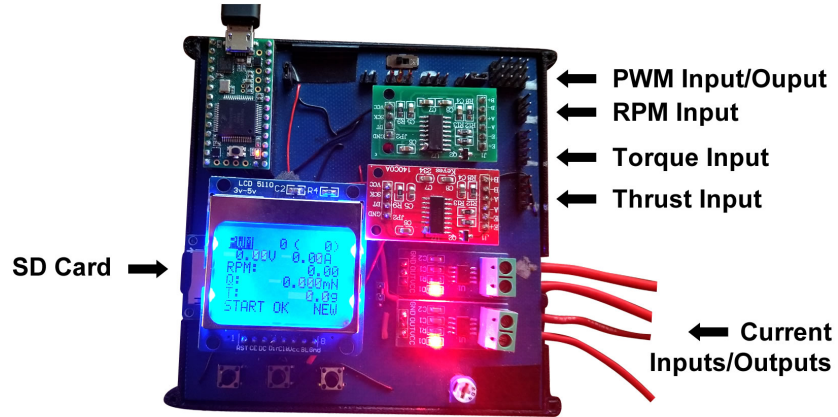


Figure 6.2: Picture of the data acquisition (DAQ) system developed for the purpose of quantifying Naviator power system properties.

Actuation of the vehicle is achieved through the use of eight rotors paired into four coaxial pairs as discussed in previous sections. However, the actuation is limited and it is important to characterize these limits. Therefore, a data acquisition system (DAQ)



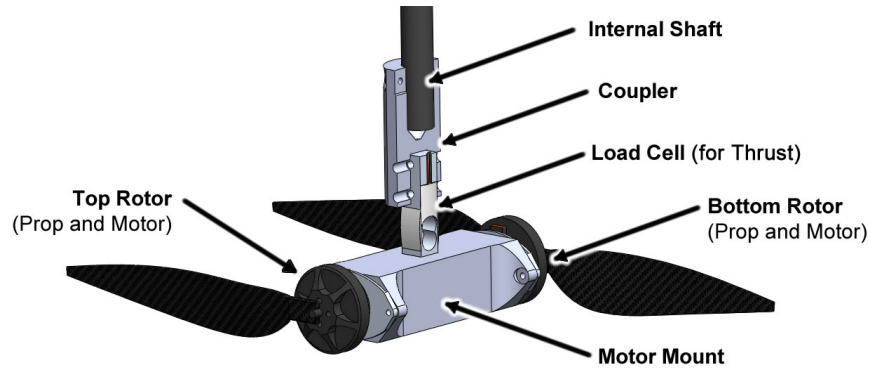


Figure 6.3: Illustration of the experimental setup for collecting data corresponding to the thrust produced by a pair of counter-rotating coaxial rotors.

was developed to collect data from the power system which consists of a battery or power supply feeding into an ESC that then commutates the rotor. The DAQ, shown in Figure 6.2, comprises two ACS712 30A hall effect-based linear current sensors, two HX711 24-Bit analog-to-digital converters (ADC) for load cells, a digital screen, an SD card port and a Teensy 3.2 breakout board running a 72MHz Cortex-M4 micro-controller unit to tie all of the sensors and peripherals together. Experiments were carried out to test the thrust generated per arm of the vehicle for different pulse-width modulated values, which are used to as the input to the motor drivers. The test setup is shown in Figure 6.3 and consists of two coaxial rotors with the same



Figure 6.4: Picture of the experimental setup for collecting data corresponding to the thrust produced by a pair of counter-rotating coaxial rotors placed inside of a water channel in preparation for static and dynamic water testing.

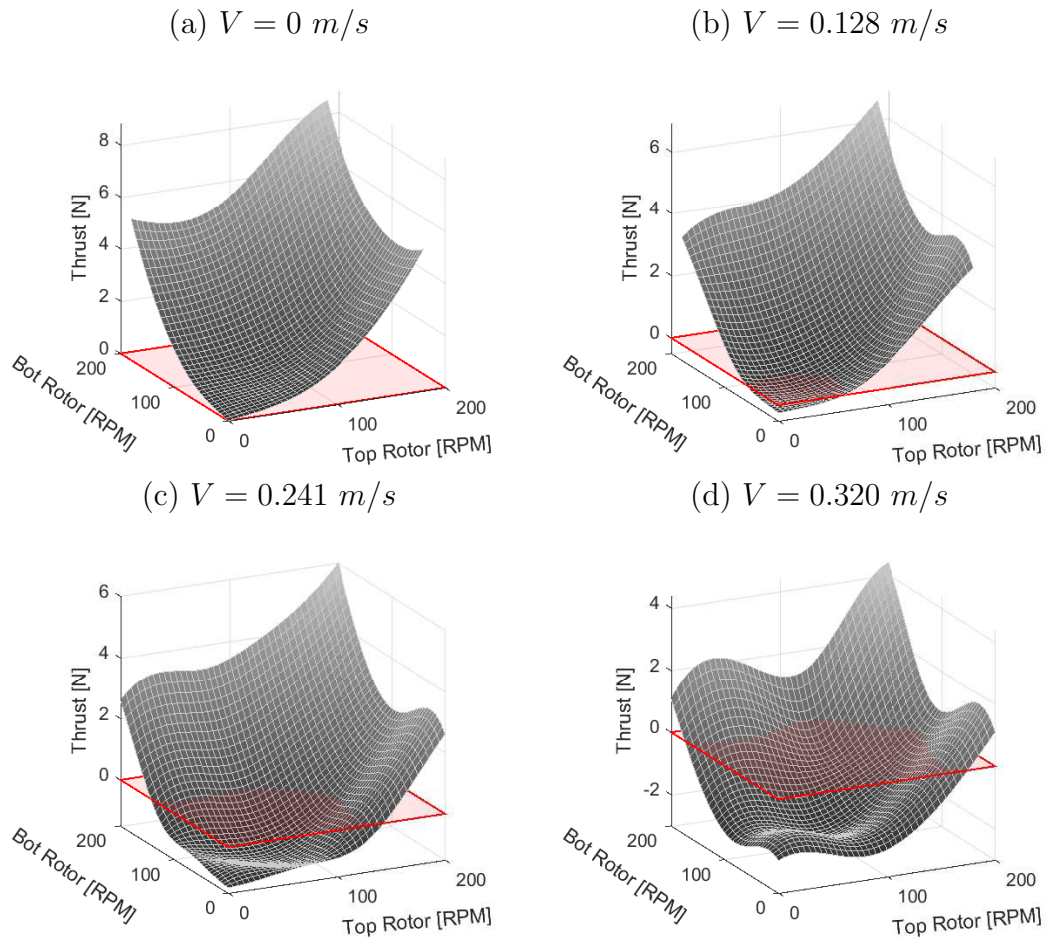


Figure 6.5: Thrust force surfaces constructed by permutating through the different possible combinations of bottom and top rotor throttle levels operating underwater, plotted in terms of rotor angular velocities and thrust force for (a) the static case where  $V = 0 \text{ m/s}$  and dynamic cases where (b)  $V = 0.128 \text{ m/s}$ , (c)  $V = 0.241 \text{ m/s}$  and (d)  $V = 0.320 \text{ m/s}$ .

geometrical characteristics as the propulsion system on one arm of the vehicle. Each rotor is driven by the same ESCs as those running on the vehicle prototype NV5 and are power using a power supply set to 25.2V, which is the same voltage as when the vehicle is fully charged.

Thrust generation for aerial propellers in the air is well understood, but for underwater propulsion, information is not as easily available. Therefore, the test setup was put inside of a water channel as shown in Figure 6.4, which is capable of supplying 0–0.35 m/s stream velocities at a water height of 1m. Experiments were conducted in a static water channel with  $V = 0$  m/s as well as with dynamic conditions of  $V = 0.13$  m/s,  $V = 0.24$  m/s and  $V = 0.32$  m/s. Since the total thrust depends of the throttle inputs for the top rotor and bottom rotor, the result for each water channel velocity will be a surface, as shown in Figure 6.5. The results map the rotor angular velocities to thrust generated per arm and show that for the same rotor speed, the thrust generated decreases as the stream velocity increases.

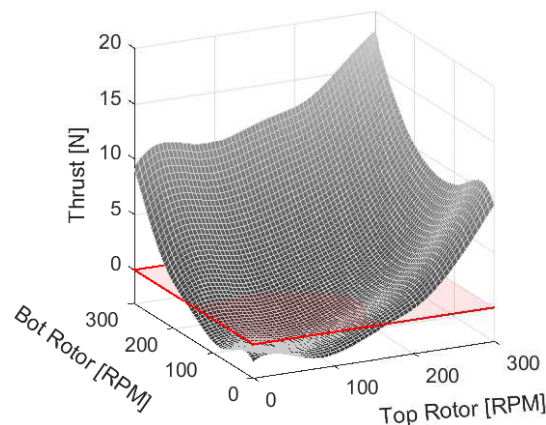


Figure 6.6: Dynamic thrust in water for a stream velocity of 0.32 m/s showcasing the highest rotor angular velocity achieved in the water channel.

The rotor angular velocities in Figure 6.5 were limited to 200 RPM for comparison. However, at the highest water tunnel stream velocity of 0.32 m/s, the achievable angular velocity of the rotors was 300 RPM generating a combined thrust of 19N, as shown in Figure 6.6.

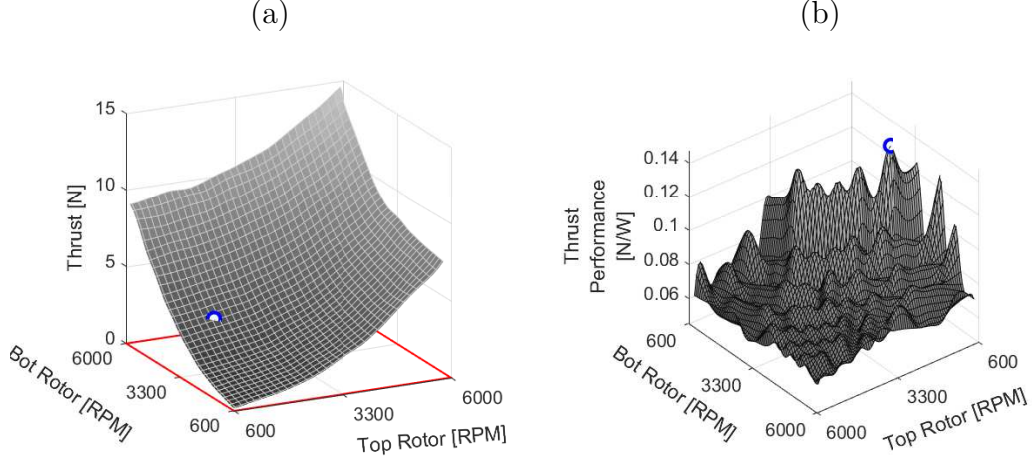


Figure 6.7: Aerial propulsion characteristics showing (a) the thrust force surface for different permutations of bottom and top rotor throttles during static operation in the air and (b) and accompanying thrust performance surface, which is an indication of efficiency.

The static thrust surface for operation in the air is shown in Figure 6.7(a), showing a similar trend to the static thrust surface for operation in the air in Figure 6.5(a). Furthermore, since the rotor operation in the air is known to be optimized, the thrust performance (which is an indication of efficiency) results for aerial propulsion is shown in Figure 6.7(b), where the minimum thrust performance observed was 0.0455 N/W (with corresponding top/bottom velocities of 2020 and 1241 RPM, respectively) and the maximum thrust performance observed was 0.143 N/W (with corresponding top/bottom velocities of 1500 and 3420 RPM, respectively), which is marked by a circle in the figures and produces a thrust force of 3.3N.

The ESCs are driven by PWM signals and have two modes: water and air. For water mode, the driver was programmed to use specific speeds for a given PWM range of 1050 – 1300  $\mu s$ . For air mode, the driver attains speeds matching to specific torques (ultimately, a duty cycle) controlled by a PWM range of 1325 – 1800  $\mu s$ . For PWM values greater than 1800  $\mu s$ , the air mode duty cycle saturates to 100% and for all other PWM values outside the defined domains, the rotors do not spin. The RPM

for a given PWM in water mode was programmed according to

$$\text{RPM} = 1.5644 \cdot \text{PWM} - 1641.9 \quad , \quad 1050 < \text{PWM} < 1300 \quad (6.2)$$

and the duty cycle for the air mode for a given PWM is known to be

$$\text{Duty Cycle} = (0.1968 \cdot \text{PWM} - 254.2) \% \quad , \quad 1325 < \text{PWM} < 1800 \quad (6.3)$$

where the duty cycle is directly proportional to torque.

### 6.3 Restoring Forces

The restoring forces of the vehicle include the balance between forces and moments induced from gravity and buoyancy. Since the centers of mass and buoyancy were designed to coincide, the resulting restoring moments are negligible. However, whereas gravity is present throughout all vehicle operation (air and underwater), buoyancy only plays a major role when the vehicle is underwater. Since the restoring moments

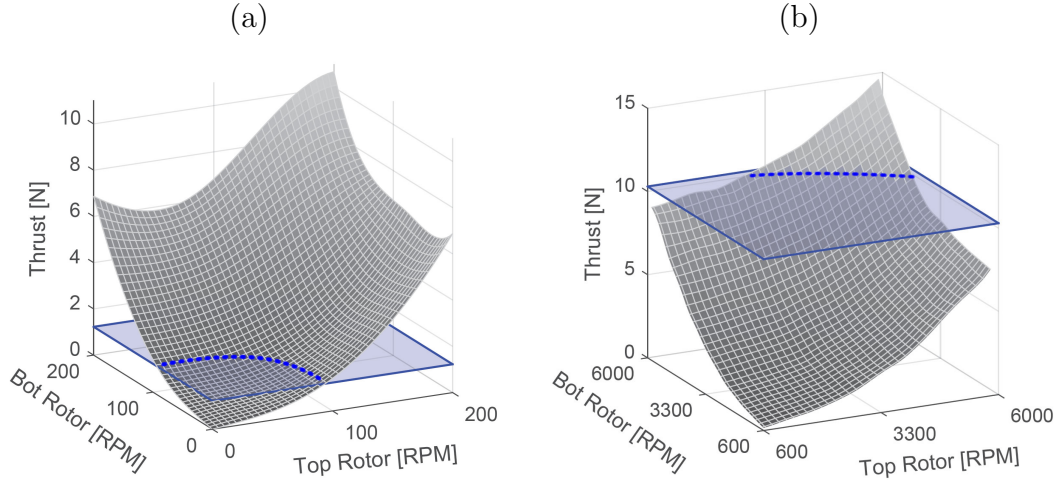


Figure 6.8: Thrust force surface for different top and bottom rotor speeds and the hover thrust plane with a dashed intersection line indicating the speeds at which the rotors may operate to maintain altitude for (a) underwater operation and (b) aerial operation.

are negligible, the disparity between gravity and buoyancy is the only force that must be compensated for when designing the controllers. As given in Section 6.1, the net buoyancy of the vehicle is  $\mathcal{B} - mg = -4.9N$  when completely underwater and  $\mathcal{B} - mg \approx -41.2N$  when completely in air. When the vehicle is partially submerged, the buoyancy may be found according to equation (5.13) in Section 5.3. If the vehicle is in a single medium and level, the possible PWM values for hovering in place is indicated by the dashed blue line in Figure 6.8(a) for water and Figure 6.8(b) for air.

## 6.4 Drag Coefficient and Drag Forces

The translational drag underwater will be calculated using information about the pitch, throttle and speed of the vehicle as it translates underwater as close to steady state conditions as possible. To accomplish this, the vehicle will be given a pitch and throttle that result in a linear trajectory at constant depth. Once the vehicle is moving at steady state, the time at which it crosses two markers along the direction of travel will be logged and the time difference between when it crossed these markers together with the distance between them will be used to determine the average vehicle speed.

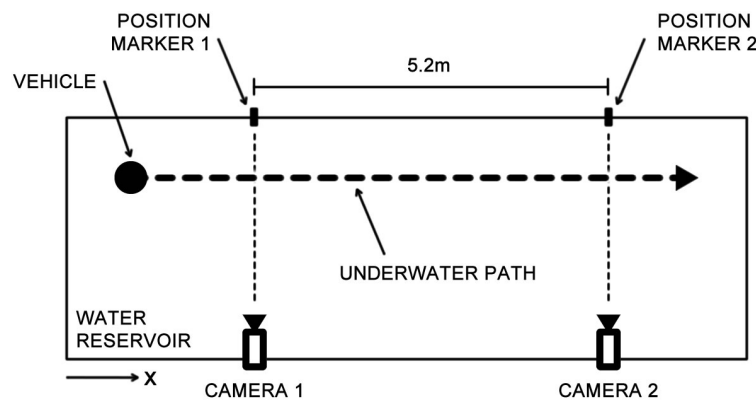


Figure 6.9: Illustration of the experimental setup for determining the translational drag coefficient of the Naviator NV5 prototype showing the vehicle position, the distance markers, travel path, camera sensors, and associate relative positions (not to scale).

The pitch angle will determine the characteristic area to utilize for determining the drag coefficient. A top view of the test setup is illustrated in Figure 6.9 showing the initial location of the vehicle, the location of the distance markers and the location of the cameras used to time when the vehicle crosses a marker. The controlled variable is the distance. The independent variables are pitch angle and throttle. The dependent variables are the output throttles for each rotor and the time difference between when the vehicle crosses the first marker and the second marker, which can be used to determine the average speed.

For instance, the first mission with input pitch angle  $\theta = 35^\circ$  and throttle  $Thr = 29\%$  resulted in a time interval of  $\Delta t_{(1)} = 34.3 \text{ s}$  and thus an average speed of  $v_{(1)} = d/\Delta t_{(1)} = 0.174 \text{ m/s}$  where  $d = 5.2 \text{ m}$  is the distance between the two distance markers. Additionally, the output PWM to each individual rotor driver for motors 1

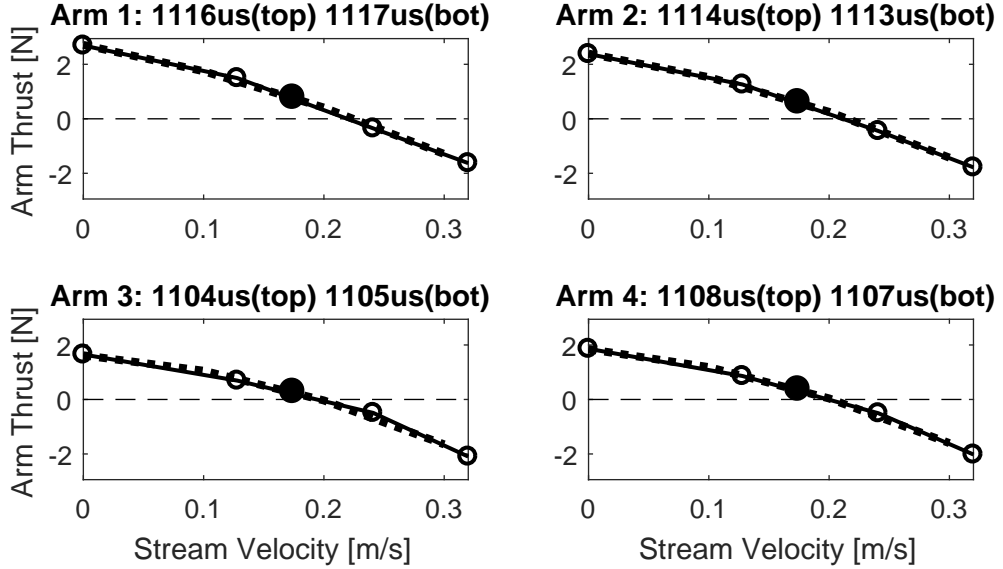


Figure 6.10: Plots detailing the two-stage interpolating process by which the throttle outputs of the translational drag experiments get converted into a thrust force per arm by first undergoing a three-dimensional thrust surface linear interpolation for several speeds, followed by a quadratic interpolation to obtain thrust for speeds which do not have associated experiment data. The hollow circles indicate data extracted from the first stage interpolation (connected by a solid line), the dashed line is the polynomial fit to the first stage interpolation, and the solid circle marks the output of the second stage of the interpolation process.

through 8 was recorded to be

$$[M1 \ M2 \ ... \ M8] = \begin{bmatrix} 1116 & 1114 & 1104 & 1108 & 1113 & 1117 & 1107 & 1105 \end{bmatrix} \quad (6.4)$$

Next, the thrust data from Section 6.2 for static and dynamic underwater operation is used to determine the thrust output per arm corresponding to the motor PWM outputs from (6.4). The thrust surfaces for the rotor pairs (top and bottom) are available for four different relative stream velocities and the current stream velocity of  $0.174 \text{ m/s}$  is not among them. To determine the most adequate thrust output, a two-stage interpolation is conducted, which is illustrated in Figure 6.10 for each of the vehicle rotor pairs. First, for each arm, a three-dimensional linear interpolation is done to determine what the thrust output per arm would be for the given top and bottom rotor PWM values for each of the stream velocities available, marked by the hollow circles. Next, it is known that the drag force is quadratic with the stream velocity and that in this situation, drag is a negative force (opposite the thrust). Therefore, the second step is to apply a quadratic fit to the data points found for each stream velocity and indeed it is found that it is a negative quadratic with an offset. This polynomial fit is used to determine what the thrust generated for each arm would be at the given stream velocity  $v$  and it is found that the thrust generated for arms 1 through 4 is

$$[A1 \ A2 \ A3 \ A4] = \begin{bmatrix} 0.79 & 0.62 & 0.30 & 0.38 \end{bmatrix} [N] \quad (6.5)$$

for a total thrust of  $T_{\Sigma} = 2.1 \text{ N}$ . Assuming the vehicle is close enough to steady state conditions, which is a reasonable assumption since throughout the mission there are negligible variations in pitch angle, throttle outputs, and depth, the drag force may be approximated by the projection of the total thrust onto the horizontal  $F_D \approx T_{\Sigma} \cdot \sin(\theta) = 1.22N$  as illustrated in Figure 6.11.



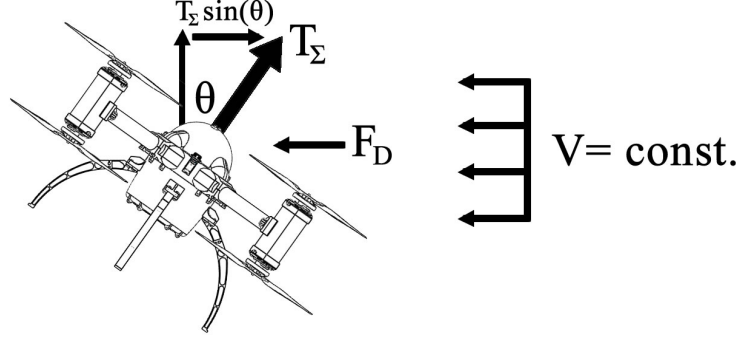


Figure 6.11: Illustration of the forces acting on the vehicle (neglecting restoring forces since they are inconsequential for horizontal motion).

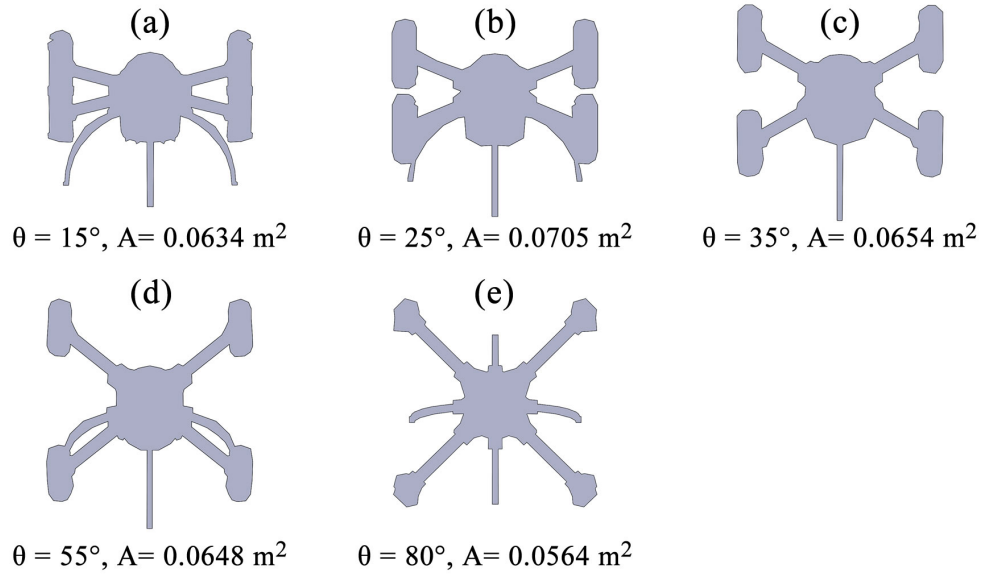


Figure 6.12: Frontal area for different pitch angles taken directly from the Naviator NV5 CAD model.

In addition to isolating the horizontal component of the total thrust, the pitch angle also determines the characteristic area used to calculate the drag coefficient, which is taken to be the frontal area of the vehicle, as shown in Figure 6.12 for different pitch angles. The final step is to calculate the drag coefficient according to (5.16), where the drag coefficient

$$C_D = \frac{F_D}{0.5 \cdot \rho \cdot V^2 \cdot A} = \frac{1.22N}{0.5 \cdot (1000\text{kg/m}^3) \cdot (0.174\text{m/s})^2 \cdot (0.0654\text{m}^2)} = 1.23 \quad (6.6)$$

with a corresponding Reynolds number of

$$\text{Re} = \frac{DV}{\nu} = \frac{(0.23\text{m})(0.174\text{m/s})}{1.0035 \cdot 10^{-6}\text{m}^2/\text{s}} = 3.99 \cdot 10^4 \quad (6.7)$$

where  $D$  is the characteristic diameter of the vehicle (diameter of the main pressure vessel). The results of this experiment and similar experiments following the same procedure are summarized in Table 6.1. The shape of the vehicle falls somewhere between a sphere, a cylinder and a rectangular prism for which the drag coefficients near  $\text{Re} \sim 10^4$  are 0.5, 1.15, and 1.05-2.05, respectively [1]. The results confirm that the drag coefficient does fall within these ranges and for preliminary studies, the drag coefficient will be taken to be the average of these results, which is  $C_D = 1.02$ .

Table 6.1: Translational Drag Experimental Results

$\theta$ [°]	$Thr$ [%]	$V$ [ $\text{m}^2$ ]	$A$ [ $\text{m}^2$ ]	$\text{Re} \cdot 10^4$	$F_D$ [ $N$ ]	$C_D$
15.4	22.9	0.116	0.0634	2.64	0.36	0.84
24.13	24.7	0.152	0.0705	3.46	0.64	0.79
30.25	26.6	0.179	0.0700	4.09	0.67	0.60
35.50	28.5	0.174	0.0654	3.99	1.22	1.23
53.99	38.7	0.273	0.0648	6.21	3.92	1.63

At this stage, it is important to realize that research into multi-medium vehicles is a new field of study and that much of what is being investigated falls within uncharted territory—with few comparatives from which to verify results. The hope is that through eventual collaborative effort, a consensus will be reached as to how such vehicle should be characterized.

## Chapter 7

### Control Strategies

Thus far, the vehicle configuration and dynamic model were defined. Next, control laws will be presented which will render the system stable and aim to improve the maneuverability of the vehicle. Some key challenges include the assimilation of discrete-continuous dynamics into a controller that is both effective at offering agility and practical for implementation in real-time experiments, while acknowledging that the vehicle will, in most cases, be operating in a GPS-denied environment without position estimation where neither the absolute or relative positions are available (ie. the controller does not have access to translation measurements along the  $\hat{\mathbf{a}}_1$  and  $\hat{\mathbf{a}}_2$  directions or the inertial  $xy$ -plane). Position estimation could be made possible with aides such as doppler velocimetry log (DVL), short baseline (SBL), ultra-short baseline (USBL), optical flow, or simultaneous localization and mapping (SLAM) and similar techniques. However, these systems are too heavy for MAVs and therefore, further discussions will give special focus to the observable state variables ( $Z$ ,  $\phi$ ,  $\theta$  and  $\psi$ ).

**Input vector, state space and state variables** Let the input vector be

$$\mathbf{u} = \begin{bmatrix} T_\Sigma & \boldsymbol{\tau}_{xyz}^T \end{bmatrix}^T = \begin{bmatrix} T_\Sigma & \tau_x & \tau_y & \tau_z \end{bmatrix}^T \quad (7.1)$$

and the state space  $O \subset \mathbb{R}^n$  where the state vector  $\boldsymbol{\eta} \in O$  stores the position and attitude of the vehicle along with the corresponding derivatives at a given instant

$$\boldsymbol{\eta} = \begin{bmatrix} \mathbf{r}^T & \mathbf{v}^T & \boldsymbol{\Phi}^T & \dot{\boldsymbol{\Phi}}^T \end{bmatrix}^T = \begin{bmatrix} X & Y & Z & \dot{X} & \dot{Y} & \dot{Z} & \phi & \theta & \psi & \dot{\phi} & \dot{\theta} & \dot{\psi} \end{bmatrix}^T \quad (7.2)$$

which is used by the controllers in the feedback loop and is defined in (7.2). Note that this is an under-actuated system since it has six degrees of freedom but only four inputs.

In the sections that follow, a typical control strategy for multirotors will be introduced in Section 7.1, after which additional control strategies will be adopted and/or modified for use with a multi-medium multirotor vehicle in Sections 7.2 through 7.4, thus setting up the framework and proceeding to improve maneuverability.

## 7.1 Single-medium multirotor controller: Hierarchical PID

In order to highlight the inherent differences between a multi-medium multirotor vehicle and single-medium multirotor vehicle, first consider the proportional-integral-derivative (PID) controller applied to a vehicle with Euler angles representation shown in Figure 7.1, where the two controller loops are shown: (1) an altitude controller with reference  $Z_d$  and an angle controller in cascade with a body angle rate controller with

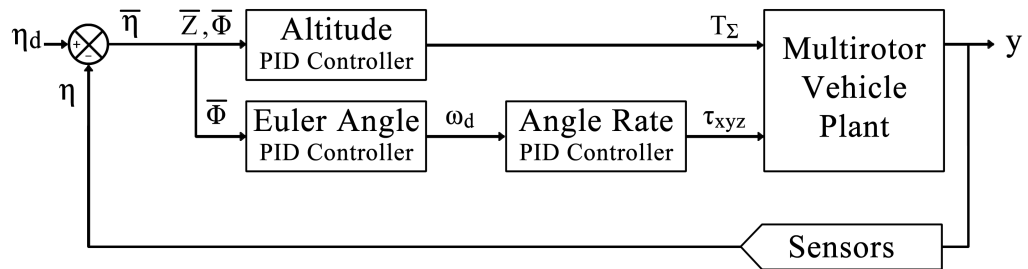


Figure 7.1: Block diagram of a standard hierarchical PID controller commonly used for multirotor vehicles in a single medium, where the subindex **d** indicates that it is a desired reference for the controller to follow and **y** is the output to the system.

reference  $\Phi_d$ . A PID controller is the “industry standard” and most commonly used controller due to its simplicity and ability to tackle many different types of systems [7]. The input to a PID controller is simply the error between the input/desired state and the output/measured state, as defined for the state variables of interest in (7.3) through (7.5), where  $Z = \mathbf{r} \cdot \hat{\mathbf{a}}_3$ , the upper bar indicates the error for the specific state and the subindex d indicates that it is a desired or target state, such that

$$\bar{Z} = Z_d - Z \quad (7.3)$$

$$\bar{\Phi} = \Phi_d - \Phi \quad (7.4)$$

$$\bar{\omega} = \omega_d - \omega \quad (7.5)$$

Although the system is under-actuated, it has full torque actuation and a PID control law  $\tau_{xyz}$  can be implemented based on a desired angular velocity  $\omega_d$ , which is ultimately determined by a desired angular orientation  $\Phi_d$  in (7.4) that is then used to determine the angular rate error by plugging in the desired angular rate

$$\omega_d = \mathbf{Q}(\Phi) \mathbf{K}_{P\Phi} \bar{\Phi} \quad (7.6)$$

into angular rate error, resulting in inner attitude control loop

$$\tau_{xyz} = \mathbf{K}_{P\omega} \bar{\omega} + \mathbf{K}_{D\omega} \dot{\bar{\omega}} + \mathbf{K}_{I\omega} \int \bar{\omega} dt \quad (7.7)$$

In the torque controller defined by (7.6)-(7.7),  $\mathbf{K}_{P\Phi}$  contains the proportional gains,  $\mathbf{Q}(\Phi)$  is once again the transformation from Euler angle rates to body angular velocities,  $\mathbf{K}_{P\omega}$  contains the proportional gains,  $\mathbf{K}_{D\omega}$  contains the derivative gains, and  $\mathbf{K}_{I\omega}$  contains the integral gains. In the Euler angle controller. Note that upon application of the Euler angles controller proportional gain matrix  $\mathbf{K}_{P\Phi}$ , the  $\mathbf{K}_{P\Phi} \bar{\Phi}$  component is considered to be describing Euler angle rates and not Euler angles, which is then

mapped to a desired body rate reference.

For the remaining input, thrust, the goal is to match the Earth fixed frame vertical component along the axis  $\hat{\mathbf{a}}_3$  of the total thrust  $T_\Sigma$  such that it compensates for gravity and buoyancy and use that as a midpoint to a  $\hat{\mathbf{a}}_3$ -axis PID controller in the inertial frame. To obtain the vertical component of the total thrust in the inertial frame, the familiar transformation  $\mathbf{R}(\Phi)$  is applied to  $T_\Sigma$  and then the result is projected onto  $\hat{\mathbf{a}}_3$  by multiplying  $\hat{\mathbf{e}}_3 = [0 \ 0 \ 1]^T$ . Applying a PID controller with compensation for the restoring forces to the projection of the total thrust onto the  $\hat{\mathbf{a}}_3$ -axis and solving for the total thrust yields

$$T_\Sigma = \frac{mg - \mathcal{B} + K_{PZ}\bar{Z} + K_{DZ}\dot{\bar{Z}} + K_{IZ} \int \bar{Z} dt}{\hat{\mathbf{e}}_3^T \mathbf{R}(\Phi) \hat{\mathbf{e}}_3} \quad (7.8)$$

Unfortunately, division by zero is possible in this scheme and an alternative is to instead of projecting the total thrust onto the inertial frame vertical axis, to project the PID controller with compensation for the restoring forces onto the body frame vertical axes  $\hat{\mathbf{b}}_3$  as in

$$T_\Sigma = \hat{\mathbf{e}}_3^T \mathbf{R}(\Phi)^T \hat{\mathbf{e}}_3 \left[ mg - \mathcal{B} + K_{PZ}\bar{Z} + K_{DZ}\dot{\bar{Z}} + K_{IZ} \int \bar{Z} dt \right] \quad (7.9)$$

In summation, the inputs in (7.1) can be used to control the state variables  $Z$ ,  $\phi$ ,  $\theta$  and  $\psi$ . Since altitude of the vehicle is determined using the pressure sensor, depending on its location, it may be necessary to apply a transformation to relate the position back to the vehicle centroid. However, moving forward, the pressure sensor will be assumed to be sufficiently close to the centroid such that altitude estimation errors due to vehicle orientation are negligible. Furthermore, it has been shown in several works that linear control strategies such as the PID controller used on the multirotor here and similar strategies are guaranteed to be exponentially stable for nearly all rotations (see [25], [28] and [32])

However, in practice, these inputs must be mapped to actuator inputs, which are used to generate the necessary forces and torques. The only type of actuator input is the throttle for each rotor, which controls the duty cycle of the commutation pulses, where the duty-cycle is linearly correlated to thrust and torque. To determine the throttle for each rotor of this under-actuated vehicle in response to the input  $\mathbf{u}$ , a thrust and torque mixer is applied. The mixer may be obtained by simply solving (5.9) for the thrusts  $\mathbf{T} = [T_1 \dots T_8]^T$  using optimization techniques such as the minimum norm [8]. Approaching the aforementioned system of equations as an optimization problem, first let the variables  $\mathbf{y} = \mathbf{T}$ , the known values  $\mathbf{b} = \mathbf{u}_d$  where  $\mathbf{u}_d$  is the desired inputs vector to the dynamic system, and the mixing matrix for thrust and torque  $\mathbf{A} = [\mathbf{1}_{8 \times 1} \quad \text{sgn}(\mathbf{C}^T)]^T$  where the signum function  $\text{sgn}$  returns the element-wise sign of an arbitrary value  $* \in \mathbb{R}$  according to  $\text{sgn}(*_{ij}) = *_{ij} \div |*_{ij}|$ . Proceeding to solve the optimization problem statement

$$\begin{aligned} & \text{minimize} \quad \|\mathbf{T}\| \\ & \text{subject to} \quad \mathbf{A}\mathbf{y} = \mathbf{b} \end{aligned} \tag{7.10}$$

the solution  $\mathbf{y}^* = \mathbf{T}^*$  yielding the minimum norm of the thrusts is given by

$$\mathbf{T}^* = \begin{bmatrix} T_1^* & \dots & T_8^* \end{bmatrix}^T = \mathbf{A}^T (\mathbf{A}\mathbf{A}^T)^{-1} \mathbf{b} \tag{7.11}$$

Intuitively, the same result can be obtained by distributing the output of the altitude controller to each rotor, resulting in a baseline of  $T_{\text{base}} = T_{\Sigma}/8$  and adding or subtracting from each rotor according to a desired torque  $\boldsymbol{\tau}_{\text{xyz}}$  as shown in

$$\mathbf{T}^* = T_{\text{base}} \mathbf{1}_{8 \times 1} + \frac{1}{8} \text{sgn}(\mathbf{C}^T) \boldsymbol{\tau}_{\text{xyz}} \tag{7.12}$$

Note that the  $\mathbf{C}$  matrix in the thrust and torque mixing is used only as a reference of direction (only the signs of the matrix matter) and the magnitude of the response

relies solely on the output of the controller, which is dependent on the controller gains and saturation. The desired thrust output  $\mathbf{T}^*$  is then mapped to the system output throttle to the motor drivers  $T_{\%i}$  using a linear factor  $K_{T_{\%}}$  where  $T_{\%i} = K_{T_{\%}} T_i^*$ .

### 7.1.1 Simulations in a single medium: Water

Applying the controllers within this section, the simulations were carried out using MATLAB Simulink<sup>®</sup> employing the hierarchical approach described herein with an Euler angle reference controller that feeds into a body angular rate reference controller. See Appendix A for a snapshot of the Simulink model used in this scheme. When the control strategy was implemented, the autopilot firmware and Simulink<sup>®</sup> setup were made to have the same control scheme with equivalent gains. These gains were selected in simulation and tuned experimentally through trial and error, and are presented in Table 7.1. Since there is no consensus on tuning a PID controller due to it being dependent on specific applications, discussions relating to how PID gains were obtained will be limited moving forward.

Table 7.1: Control gains underwater

$K_{pz}$	$K_{dz}, K_{iz}$	$\mathbf{K}_{\Phi}$
5	0	4.5
$\mathbf{K}_p$	$\mathbf{K}_d \times 10^{-3}$	$\mathbf{K}_i$
$diag(0.25, 0.25, 0.2)$	$diag(4, 4, 10)$	$diag(0.01, 0.01, 0)$

In order to validate that the control strategy employing gain scheduling works for underwater operation, we begin by running an underwater simulation with underwater gains. A mission that highlights the excellent maneuverability of the prototype is in conducting a “Figure 8” shape underwater. We have feedback on the altitude/depth and attitude of the vehicle. Therefore, we can complete a figure eight by commanding the vehicle pitch forward and translate while maintaining depth to make a full right-hand turn followed by a full left hand turn and we can control the turn radius by



modifying increasing or decreasing the desired yaw, which translates to prescribing a yaw rate (but in the form of a linear yaw angle reference). Throughout the simulation, the vehicle will be given an altitude reference of  $-1m$  (ie. in water) and a roll angle of  $0^\circ$ . During this, the vehicle will be told to pitch forward to  $75^\circ$  and then complete the right and left hand turns. The turns will be provided as a linear yaw input from  $0^\circ$  to  $360^\circ$  and then back to  $0^\circ$ , after which the vehicle will pitch to level back to  $0^\circ$  and the mission will conclude.

Figures 7.2 and 7.3 show the altitude and Euler angles, respectively.

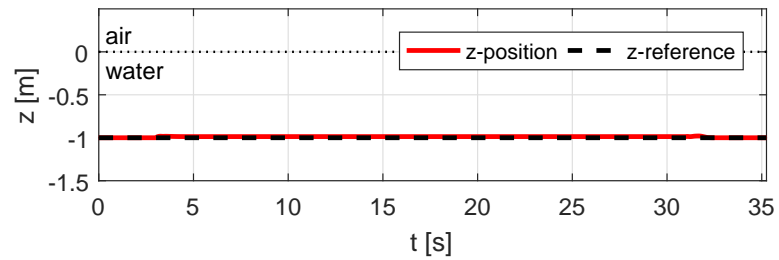


Figure 7.2: Euler angles and respective input reference angles of the vehicle over time as it conducts a figure 8 maneuver in simulation.

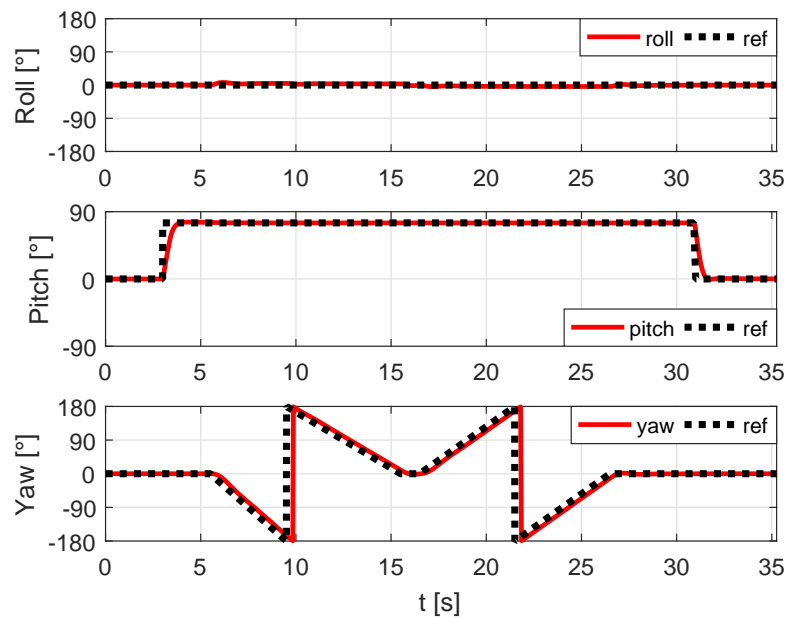


Figure 7.3: Euler angles and respective input reference angles of the vehicle over time as it conducts a figure 8 maneuver in simulation.

The altitude controller shown in Figure 7.2 has excellent agreement with the desired reference, even with the drastic forward pitch angle of  $75^\circ$ . The Euler angles shown in Figure 7.3 also match with the reference very well. A small perturbation can be seen in the roll as the vehicle conducts a drastic yaw change, as seen in 7s, 16s and 25s. The pitch response was great and is able to achieve its target within one second, despite needing to overcome the induced drag torque. The yaw heading of the vehicle is wrapped within  $-180^\circ$  to  $180^\circ$  for simplicity and also follows the reference very well, lagging behind by only 0.5s chiefly due to the drags involved.

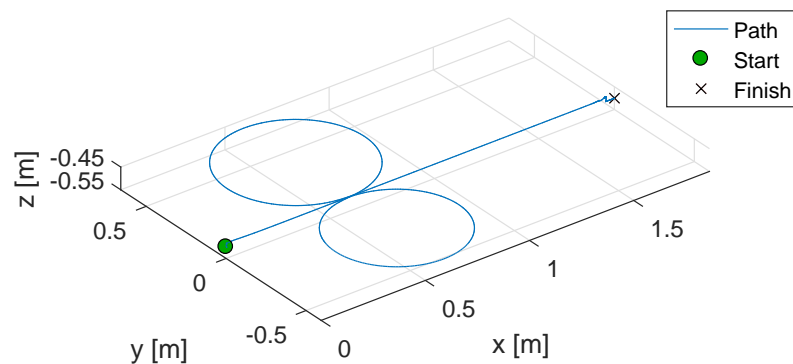


Figure 7.4: Position of the vehicle over time as it conducts a figure 8 maneuver in simulation.

The output position of the system is shown in Figure 7.4 and is a “Figure 8” as expected. One thing to note is that the left-hand turn circle of the path is larger than the right-hand turn. That is because when making the left-hand turn, the vehicle must compensate for both moment of inertia of the platform and angular momentum of the right-hand turn, whereas when commencing the the right-hand turn, there is no angular momentum to that resists the change in direction. Therefore, the right-hand turn is able to complete the full loop quicker than in the left-hand turn, resulting in a smaller trajectory loop on the right.

### 7.1.2 Experiments in a single medium: Water

The simulation results can be validated through several real-time experiments in both mediums. As a proof of concept and in order to highlight the great maneuverability of the proposed configuration, a "Figure 8" mission is performed, where the desired references are identical to the simulated references. The Naviator is fully autonomous—the references are fed to the vehicle as an input before the mission and later initialized.

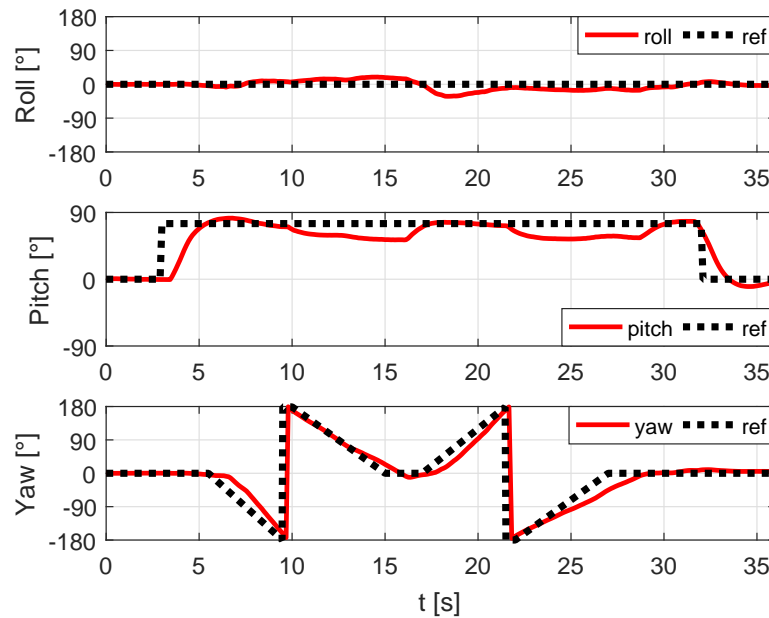


Figure 7.5: Euler angles and respective input reference angles of the vehicle over time as it conducts a figure 8 maneuver in the field.

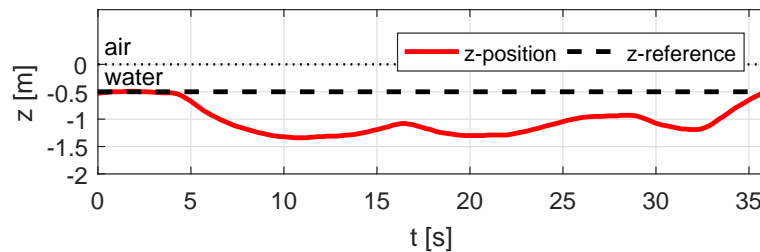


Figure 7.6: Altitude/Depth and respective input altitude reference of the vehicle over time as it conducts a figure 8 maneuver in the field.

The agreement between the outputs and references of altitude in Figure 7.6 and Euler

angles in Figure 7.5 are satisfactory, but there are some errors in altitude and attitude. An offset in the altitude of roughly  $1m$  exists. The optional tether was used to aide in data collection and the weight and pull of the tether is known to adversely affect the weight compensation of the vehicle, and so, an offset is expected. The coupling between the Euler angle changes are more pronounced than in the simulation, but the trends are the same—whenever there is a large change in the yaw angle, there is a perturbation in the roll. The drop in pitch angle during turns when the yaw rate is constant indicates that the proportional gain on the pitch should be increased and favored over the others since it is taken to its extreme.

Given the simplified nature of the dynamic model, the vehicle performed the mission exceptionally well and a video of the experiment can be found online at <https://youtu.be/CFioBkh9haQ>. Another video without a tether in which both an autonomous "Figure 8" maneuver and manual transition out of the water are conducted can be found at <https://youtu.be/V-QRaZpx8CU>. In the latter video, we can also appreciate the ability of the vehicle to operate in the interface if necessary.

## 7.2 Coupling discrete-continuous dynamics:

### Hybrid controller

Whereas a multi-medium vehicle is meant to periodically traverse between mediums of very different dynamics, the typical PID controller implementation for multirotors from Section 7.1 is based solely on continuous dynamics of a vehicle that operates in a single medium. It therefore becomes necessary to consider discrete events in the control strategy where there is an interaction between continuous and discrete dynamics which, when coupled, is best described as a hybrid system. Here, the term "hybrid system" is understood in the sense of a system whose dynamics depend on a coupling between continuous and discrete variables [44], [16]. The concept of hybrid

control systems has been recently applied to UAVs in order to consider with these discontinuous dynamics as a whole system [41], [5], [35], [20].

Adopting the definition proposed in [16], consider the hybrid system  $\mathcal{H}$  with time domain  $(t, j) \in \mathbb{R}^+ \times \mathbb{N}$ , where  $t$  is the continuous time and  $j$  are the jump times. Let it consist of the data  $\mathcal{H} = (O, F, C, G, D)$  with state space  $O \subset \mathbb{R}^n$  and state

$$\boldsymbol{\eta}_c \in O := [\boldsymbol{\eta}^T \ \rho]^T = [\mathbf{r}^T \ \mathbf{v}^T \ \boldsymbol{\Phi}^T \ \dot{\boldsymbol{\Phi}}^T \ \rho]^T \quad (7.13)$$

In the system presented, a flow map  $F : O \rightrightarrows \mathbb{R}^n$  consider the pendulum example,  $O = (-\pi, \pi)$  but  $F : O \rightarrow \mathbb{R}^n$  (speed takes real values) describes the continuous behavior, a flow set  $C \subset O$  specifies when the continuous evolutions can occur, a jump map  $G : O \rightrightarrows O$  which determines the value of the state after a jump, denoted by  $\boldsymbol{\eta}_c^+ \in G(\boldsymbol{\eta}_c)$ , and a jump set  $D \subset O$  where the discrete jumps may occur. The hybrid system  $\mathcal{H}$  representation may then be written as

$$\mathcal{H} : \begin{cases} \dot{\boldsymbol{\eta}}_c \in F(\boldsymbol{\eta}_c) & \boldsymbol{\eta}_c \in C \\ \boldsymbol{\eta}_c^+ \in G(\boldsymbol{\eta}_c) & \boldsymbol{\eta}_c \in D \end{cases} \quad (7.14)$$

where for a multi-medium vehicle, the previously defined state in (7.2) is extended to include density as a parameter describing medium change. In this case, the state space  $O \subset \mathbb{R}^{12} \times \{\rho_A, \rho_W\}$ , where  $\rho_A$  is the density of air and  $\rho_W$  is the density of water.

The flow map  $F(\boldsymbol{\eta}_c)$  inherits the continuous dynamics described by (5.23)-(5.26) where the density is constant until a jump occurs, at which point the density will depend on the definition of the jump map  $G(\boldsymbol{\eta}_c)$ . Although continuous evolutions occur according to the flow set  $C := O$ , jumps occur when the vehicle altitude is in the neighborhood of the air-water interface ( $z = 0$ ) and therefore, the jump set  $D := \{\boldsymbol{\eta}_c \mid z = 0\}$ . Since the jump map simply updates the discrete parameters

within the state, it is defined as (7.15).

$$G(\boldsymbol{\eta}_c) := \left\{ \begin{bmatrix} \mathbf{r}^T & \mathbf{v}^T & \boldsymbol{\Phi}^T & \dot{\boldsymbol{\Phi}}^T & \{\rho_A, \rho_W\} \end{bmatrix}^T \quad \boldsymbol{\eta}_c \in D \right. \quad (7.15)$$

In practice, the change in medium is not instant, but a gradual process that takes place for each rotor and body independently. For instance, consider the side view of the multi-medium multirotor vehicle employing the X8 rotor configuration in Figure 7.7(a). At the given instant, rotors 1 and 2 are in the air, rotor 4 is in the water and the body indicated by 0 as well as rotor 3 are partially submerged in the water.

Therefore, the controller must update the medium and make available a metric of partially submerged regions for use in the controllers. Nevertheless, the current objective is to deliver a framework that will make clear the inherent coupling between continuous-time and discrete-time state variables. Toward this goal, it is prudent to employ a simplification shown in Figure 7.7(b) where the vehicle is taken to be a sphere with a single propeller, where the transition occurs within the bound  $|Z| \leq h$  where  $h$  is the vertical height of the vehicle. In this scheme, the discrete parameters indicating medium change are only updated when the vehicle centroid is within these bounds. Another consideration regards the safe transition of the rotors, which happens independently for each rotor when the propeller is entirely in a single medium and has enough of a fluid column  $h_p$  above and below to generate reliable propulsion. Consequently, within the transition zone there is a region  $|Z| \leq h_p$  at which the vehicle density changes at the extremes. For details on the dynamic modeling, refer to [14] for the case of underwater vehicles, [38] for aerial vehicles and [2] for general dynamics.

To control the hybrid system, first let the desired trajectory and trajectory error be defined as  $\boldsymbol{\eta}_d(t)$  and  $\bar{\boldsymbol{\eta}} := \boldsymbol{\eta} - \boldsymbol{\eta}_d$ , respectively. Furthermore, let the problem be

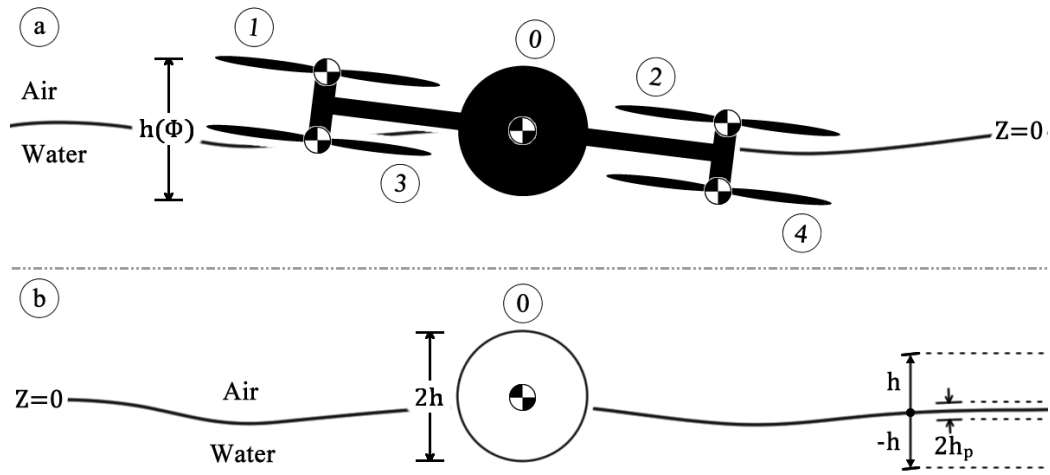


Figure 7.7: Graphical aid to describe hybrid transition through the interface showing (a) the X8 multirotor configuration of height  $h(\Phi)$  with rotors 1 and 2 in the air, rotor 4 in the water and the body indicated by 0 as well as rotor 3 partially submerged in the water and (b) a simplified example of the vehicle to illustrate transition, with height  $2h$  a single rotor coincident with the centroid of the vehicle body with required interface clearance of  $2h_p$ , both of which are partially submerged in the water, where the relevant transition regions are marked on the right with dashed lines and the centroids of the labeled components are indicated by  $\odot$ .

partitioned into three sub-problems: (1) design of a control law for vehicle operation in a single medium, (2) design of a transition strategy and (3) the design of a hybrid controller that incorporates (1) and (2).

### 7.2.1 Trajectory tracking for a single medium

Since the system is under-actuated, the position may be controlled by utilizing the reference angles  $\Phi_d$  as a virtual input, which is possible since vehicle rotations occur much faster than translations.

**Position** First consider the translation of the vehicle described by (5.23)-(5.24) and with corresponding error dynamics shown in (7.16) where the objective is to assign a new virtual input term  $\mathbf{u}_{c_r}$  to take on a value for  $T_\Sigma \mathbf{R}(\Phi_d) \hat{\mathbf{b}}_3$  for which the system converges asymptotically to a desired reference  $\boldsymbol{\eta}_d$ .

$$\mathbf{F}_r := \begin{cases} \dot{\bar{\mathbf{r}}} = \bar{\mathbf{v}} \\ m\dot{\bar{\mathbf{v}}} = (T_\Sigma \mathbf{R}(\Phi_d) + \mathcal{B}(Z, \Phi, \rho) - mg) \hat{\mathbf{b}}_3 - \mathbf{F}_{D_r}(\mathbf{v}) - m\dot{\mathbf{v}}_d \end{cases} \quad (7.16)$$

**Lemma 1.** *By choosing the feedback linearization control law  $\mathbf{u}_{c_r}$  defined in (7.17), the system defined in (7.16) is rendered asymptotically stable for some diagonal and positive definite constant matrices  $\mathbf{K}_{p_r}, \mathbf{K}_{d_r} \in \mathbb{R}^{3 \times 3}$ .*

$$\mathbf{u}_{c_r} = (mg - \mathcal{B}(Z, \Phi, \rho)) \hat{\mathbf{b}}_3 + \mathbf{F}_{D_r}(\mathbf{v}) + m\dot{\mathbf{v}}_d - \mathbf{K}_{p_r} \bar{\mathbf{r}} - \mathbf{K}_{d_r} \bar{\mathbf{v}} \quad (7.17)$$

*Proof.* Define  $\bar{\boldsymbol{\xi}} := \bar{\mathbf{r}} + \mathbf{K}_1^{-1} \bar{\mathbf{v}}$  and consider the Lyapunov candidate function  $V_1 : [0, \infty) \times \mathbb{R}^6 \rightarrow \mathbb{R}$ , with a diagonal and positive definite matrix  $\mathbf{K}_1$

$$V_1 = \frac{1}{2} \bar{\mathbf{r}}^T \bar{\mathbf{r}} + \frac{1}{2} \bar{\boldsymbol{\xi}}^T \bar{\boldsymbol{\xi}} \quad (7.18)$$



the time derivative is given by

$$\begin{aligned}\dot{V}_1 = & -\bar{\mathbf{r}}^T \mathbf{K}_1 \bar{\mathbf{r}} + \bar{\xi}^T \mathbf{K}_1 \bar{\xi} + \frac{1}{m} \bar{\xi}^T \mathbf{K}_1^{-1} \\ & (\mathbf{u}_{\text{cr}} + (\mathcal{B}(Z, \Phi, \rho) - mg) \hat{\mathbf{b}}_3 - \mathbf{F}_{\text{Dr}}(\mathbf{v}) - m\dot{\mathbf{v}}_{\text{d}})\end{aligned}\quad (7.19)$$

applying the control law (7.17)

$$\begin{aligned}\dot{V}_1 = & -\bar{\mathbf{r}}^T \mathbf{K}_1 \bar{\mathbf{r}} + \bar{\xi}^T \mathbf{K}_1 \bar{\xi} \\ & + \frac{1}{m} \bar{\xi}^T \mathbf{K}_1^{-1} (-\mathbf{K}_{\text{pr}} \bar{\mathbf{r}} - \mathbf{K}_{\text{dr}} \bar{\mathbf{v}})\end{aligned}\quad (7.20)$$

choosing  $\mathbf{K}_{\text{pr}} = m(\mathbf{K}_1^2 + \mathbf{K}_1 \mathbf{K}_2)$  and  $\mathbf{K}_{\text{dr}} = m(\mathbf{K}_1 + \mathbf{K}_2)$ , for any diagonal and positive definite constant matrix  $\mathbf{K}_2$ , yields

$$\dot{V}_1 = -\bar{\mathbf{r}}^T \mathbf{K}_1 \bar{\mathbf{r}} - \bar{\xi}^T \mathbf{K}_2 \bar{\xi} < 0 \quad (7.21)$$

Therefore, by Lyapunov's direct method, the proposed control law renders the system asymptotically stable.  $\square$

The control law and the proof presented here are close to the ones in [17], but extended to include drag and buoyancy.

**Attitude** Next, considering the rotation of the vehicle, control strategies for multi-rotor attitude in a single medium have been extensively studied, especially in the air [17] [21] [33]. In the current vehicle, a PID attitude controller similar to (7.6)-(7.7) in Section 7.1 may be written as

$$\boldsymbol{\tau}_{xyz} = -\mathbf{K}_{\text{P}\omega} (\boldsymbol{\omega} - \mathbf{Q}(\Phi) \mathbf{K}_{\text{P}\Phi} \bar{\Phi}) - \mathbf{K}_{\text{D}\omega} \dot{\bar{\omega}} - \mathbf{K}_{\text{I}\omega} \int \bar{\omega} dt \quad (7.22)$$

Assembling the control strategies for position and attitude, the complete control law

$\mathbf{u}_c$  for trajectory tracking in a single medium (continuous dynamics) is obtained by

$$\mathbf{u}_c := \begin{bmatrix} \|\mathbf{u}_{c_r}\| & \boldsymbol{\tau}_{xyz}^T \end{bmatrix}^T \quad (7.23)$$

### 7.2.2 Transition strategy

With the control strategy for a single medium complete, the next step is to define how the vehicle handles transition in and out of the water. Recall that that transition occurs with the bound  $|Z| < h$  and that entering the denser water medium is easy and can be accomplished by simply turning off the rotors and allowing gravity to work. On the other hand, leaving the water is more complex, requiring that the total thrust be greater than the restoring forces such as gravity and buoyancy (ie.  $T_\Sigma > mg - \mathcal{B}(Z, \Phi, \rho)$ ). Although not considered, there are also other contributions other than the restoring forces mentioned which play a role in transition, such as the surface tension of the water and added mass. If  $T_n$  is a total thrust that ensures  $T_n > mg - \mathcal{B}(Z, \Phi, \rho)$ , then it can be shown that for a thrust input in the transition control law  $\mathbf{u}_{t_r}$  defined in (7.24) is stable for both case of the boolean variable  $\mathbf{i}$  defined in (7.25).

$$\mathbf{u}_{t_r} := T_n \mathbf{i} \hat{\mathbf{b}} - \mathbf{m} \mathbf{K}_1^2 \bar{\boldsymbol{\xi}} + \mathbf{F}_{D_r}(\mathbf{v}) + \mathbf{m} \dot{\mathbf{v}}_d \quad (7.24)$$

$$\mathbf{i} := \begin{cases} 0 & \bar{z} > 0 \\ 1 & \bar{z} \leq 0 \end{cases} \quad (7.25)$$

The control law for transition can then be written as (7.26).

$$\mathbf{u}_t := \begin{bmatrix} \|\mathbf{u}_{t_r}\| & \boldsymbol{\tau}_{xyz}^T \end{bmatrix}^T \quad (7.26)$$

### 7.2.3 Hybrid controller

Finally, the results from Sections 7.2.1 and 7.2.2 are incorporated into the closed-loop hybrid system  $\mathcal{H} = (F, C, G, D)$  and to negotiate between different vehicle operations, let the logic variable  $q \in \{1, 2, 3\}$  be introduced as state variables that will indicate the current operation mode and throttle cut, where  $q = 1$  is air mode,  $q = 2$  is transition mode,  $q = 3$  is water mode, the state vector becomes  $\boldsymbol{\eta}_{\mathcal{H}} := [\boldsymbol{\eta}^T \quad \rho \quad q]^T$ , and the trajectory tracking error is taken to be  $\bar{\boldsymbol{\eta}}_{\mathcal{H}} := [\bar{\boldsymbol{\eta}}^T \quad \rho \quad q]^T$ . The flow map based on the error dynamics takes the form shown in (7.27), where  $\mathbf{F}_{\mathbf{r}}$  is the error dynamics for translation defined in (7.16),  $\mathbf{F}_{\boldsymbol{\omega}}$  consists of the error dynamics for rotations derived from (5.25) and (5.26) and  $C := \mathbb{R}^{12} \times \{\rho_A, \rho_W\} \times \{1, 2, 3\}$ .

$$\dot{\boldsymbol{\eta}}_{\mathcal{H}} \in \mathbf{F} := \begin{cases} \mathbf{F}_{\mathbf{r}} \\ \mathbf{F}_{\boldsymbol{\omega}} \\ [0, 0]^T \end{cases} \quad \boldsymbol{\eta}_{\mathcal{H}} \in C \quad (7.27)$$

Furthermore, the jump map that allows the hybrid system to select different control laws base on medium change may be designed as (7.28), where the transition is only considered complete once there is sufficient air or water column  $|Z| < h$ .

$$\boldsymbol{\eta}_{\mathcal{H}}^+ = G(\boldsymbol{\eta}_{\mathcal{H}}) := \begin{cases} \mathbf{r} \quad \mathbf{v} \quad \Phi \quad \dot{\Phi} \quad \rho \quad 2 & \boldsymbol{\eta}_{\mathcal{H}} \in D_1 \\ \mathbf{r} \quad \mathbf{v} \quad \Phi \quad \dot{\Phi} \quad \rho_W \quad q & \boldsymbol{\eta}_{\mathcal{H}} \in D_2 \\ \mathbf{r} \quad \mathbf{v} \quad \Phi \quad \dot{\Phi} \quad \rho_A \quad q & \boldsymbol{\eta}_{\mathcal{H}} \in D_3 \\ \mathbf{r} \quad \mathbf{v} \quad \Phi \quad \dot{\Phi} \quad \rho \quad (2.0 - Z/|Z|) & \boldsymbol{\eta}_{\mathcal{H}} \in D_4 \end{cases} \quad (7.28)$$

and the jump set  $D$  is defined in (7.29), where vehicle enters the transition zone  $D_1$ , completes transition to water in  $D_2$ , completes transition to air in  $D_3$  and exits the

transition zone in  $D_4$ .

$$D := \cup_{i=1}^4 D_i := \begin{cases} D_1 := \{ \boldsymbol{\eta}_{\mathcal{H}} \mid q \neq 2, |Z| < h \} \\ D_2 := \{ \boldsymbol{\eta}_{\mathcal{H}} \mid \rho = \rho_A, Z \leq -h_p \} \\ D_3 := \{ \boldsymbol{\eta}_{\mathcal{H}} \mid \rho = \rho_W, Z > h_p \} \\ D_4 := \{ \boldsymbol{\eta}_{\mathcal{H}} \mid q \neq (2 - Z/|Z|), |Z| \geq h \} \end{cases} \quad (7.29)$$

In full, the hybrid control law  $\mathbf{u}_{\mathcal{H}} \in \mathbb{R}^4$  incorporates the single medium control law  $\mathbf{u}_{\mathbf{c}}$  and transition control law  $\mathbf{u}_{\mathbf{t}}$  according to the control mode  $q$  shown in (7.30).

$$\mathbf{u}_{\mathbf{r}}(\bar{\boldsymbol{\eta}}_{\mathcal{H}}, q) = \begin{cases} \mathbf{u}_{\mathbf{c}} & q \neq 2 \\ \mathbf{u}_{\mathbf{t}} & q = 2 \end{cases} \quad (7.30)$$

To ensure that the system does not remain in the neighborhood of the transition zone indefinitely, the conditions  $q_d \neq 2, |Z_d| > h$ , such that  $\bar{Z} \neq 0$  are imposed for traversing through mediums. Under such conditions, it can be shown that the hybrid system  $\mathcal{H}$  is asymptotically stable. First, note that the proposed hybrid system satisfies the hybrid system basic conditions as they are defined in [16] whereby the state space  $O = \mathbb{R}^{12} \times \{\rho_A, \rho_W\} \times \{1, 2, 3\}$  is an open set,  $\bar{C} \cap O = C$  and  $\bar{D} \cap O = D$ ,  $C$  and  $D$  are relatively closed sets in  $O$ , and  $F_c$  is a locally bounded continuous, single valued function, convex and outer semi-continuous. Also, Since  $D$  is closed and only discrete variables are only affected by the jump map,  $D \times G(D)$  is also closed and thus, the jump map is outer semi-continuous.

**Hybrid system stability** To study the stability of the hybrid system, let  $V_{\mathcal{H}}$  be a Lyapunov candidate function

$$V_{\mathcal{H}}(\boldsymbol{\eta}_{\mathcal{H}}) = V_1(\bar{\boldsymbol{\eta}}) + (\rho - \rho_d)^2 + (q - q_d)^2 \quad (7.31)$$

where the time derivative is given by

$$\begin{aligned}\dot{V}_{\mathcal{H}}(\eta_{\mathcal{H}}) &= \langle \nabla V_{\mathcal{H}}(\eta_{\mathcal{H}}), F(\eta) \rangle \\ &= \langle \nabla V_1(\bar{\eta}), F_{\mathbf{r}}(\bar{\eta}, \mathbf{u}_{\mathcal{H}}(\bar{\eta}) \times q) \rangle \quad \forall \eta_{\mathcal{H}} \in C\end{aligned}\tag{7.32}$$

Since this is a hybrid system, evolutions on  $V_c$  may be produced by continuous dynamics or discrete jumps. To apply the hybrid LaSalle's invariance principle, we compute the boundary functions for the continuous variations  $u_C$  and for the discrete ones  $u_D$ , defined as [16]

$$u_C := \begin{cases} \max_{v \in F(\eta_{\mathcal{H}})} \max_{\zeta \in \nabla V_{\mathcal{H}}(\eta_{\mathcal{H}})} \langle \zeta, v \rangle & \eta_{\mathcal{H}} \in C \\ -\infty & \text{otherwise} \end{cases}\tag{7.33}$$

$$u_D := \begin{cases} \max_{\zeta \in G(\eta_{\mathcal{H}})} \{V_{\mathcal{H}}(\zeta) - V_{\mathcal{H}}(\eta_{\mathcal{H}})\} & \eta_{\mathcal{H}} \in D \\ -\infty & \text{otherwise} \end{cases}\tag{7.34}$$

applying a hybrid control of the form (7.30), satisfying  $\langle \nabla V_1(\bar{\eta}), F_{\mathbf{r}}(\bar{\eta}, \mathbf{u}_{\mathcal{H}}(\bar{\eta}_{\mathcal{H}}) \times \{1, 3\}) \rangle < 0$  and choosing the transition law  $\mathbf{u}_t$ , we can see that  $u_C = 0$  for all  $\eta_{\mathcal{H}} \in C$ . For the discrete part we compute

$$V(G(\eta_{\mathcal{H}})) - V(\eta_{\mathcal{H}}) = \begin{cases} -3 & \eta_{\mathcal{H}} \in D_1 \\ -1 & \eta_{\mathcal{H}} \in D_2 \\ -(\rho_A - \rho_W)^2 & \eta_{\mathcal{H}} \in D_3 \cup D_4 \end{cases}\tag{7.35}$$

then the discrete bound is  $u_D = -1$  for all  $\eta_{\mathcal{H}} \in D$ . According to [16] Theorem 8.2, all the solutions to the system approach the largest invariant subset of

$$V_c^{-1}(r) \cap U \cap [\overline{u_C^{-1}(0)} \cup (u_D^{-1}(0) \cap G_c(u_D^{-1}(0)))]\tag{7.36}$$

for some  $U \subset \mathbb{R}^{14}$ ,  $r \in \mathbb{R}$ . Taking into account the constraint in the desired trajectory  $|Z_d| > h$ , we can compute  $u_D^{-1}(0) = G(u_D^{-1}(0)) = \{\emptyset\}$  and  $u_C^{-1}(0) = \mathbf{0}$ . Henceforth,

the largest invariant set in (7.36) is the origin, and every solution to the closed-loop hybrid system  $\mathcal{H}$  with control law  $\mathbf{u}_{\mathcal{H}}$  converge to the origin. We conclude that every solution to the close-loop hybrid system is precompact, and the origin is globally asymptotically stable.

#### 7.2.4 Hybrid controller Simulation

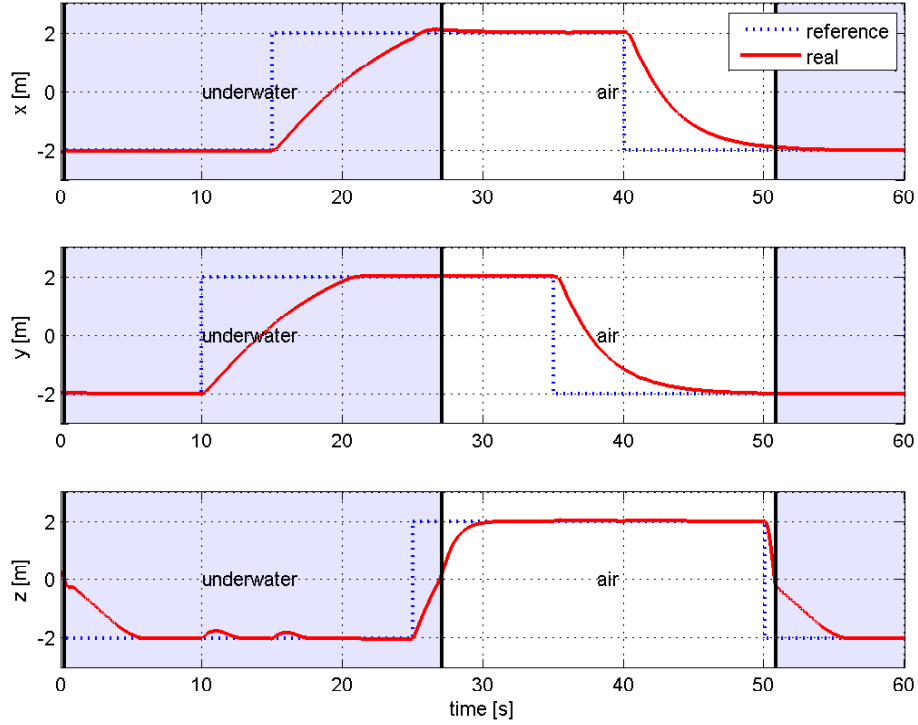


Figure 7.8:  $x$ ,  $y$  and  $z$  (from top to bottom) position during the mission. Three transitions take place at  $0.27s$ ,  $27.08s$  and  $50.80s$ . The darker (blue) area highlights when the vehicle is on underwater mode, and the white area represents air mode.

In order to test the validity of the proposed control strategy, numerical simulations were carried out using *MATLAB Simulink*. A point mass is considered with instant changes of density when the vehicle exits the transition zone, note that this is harsher than the real case, where the density changes abruptly but taking intermediate values. A small hysteresis is introduced around the interface in order to avoid chattering. The mission consisted of (1) traveling  $2m$  underwater in the  $z$ -direction; (2) traveling  $2m$

in the  $y$ -direction followed by  $2m$  in the  $x$ -direction; (3) traveling in the  $z$ -direction back to the surface; (4) flying  $2m$  above the water level; (5) displace again  $2m$  in the  $y$  then  $x$ -direction and (6) return to the water. The results are shown in Figures 7.8 through 7.10. The real and desired positions for each coordinate are shown in Figure 7.8, where there are three transitions at times  $0.27s$ ,  $27.08s$  and  $50.80s$  (solid vertical lines). The darker (blue) areas indicate when the vehicles operates underwater. The simulation proves, as expected, that dynamics underwater are slower than in air due to the damping action of the drag force, however, the inclusion of a compensation term for the drag in the control law helps to attenuate this effect. It can also be observed that fast movements in the horizontal plane may disturb the altitude due to the high coupling in their dynamics (see time  $10s$  and  $15s$ ). This can lead to undesired behavior while working close to the transition zone. A possible solution would be to define one boundary  $h$  to enter the transition zone and another one  $h_e$  to exit it. Figure 7.9 depicts the orientation of the vehicle during the mission (top three) and the total thrust commanded to the motors (bottom). From this Figure we observe that horizontal displacements underwater demand larger changes on the angles (up to  $60^\circ$ ) due to the effect of buoyancy and the drag forces. The high coupling of the system produces a large change on the direction of the thrust force, affecting the control over  $z$ , and special attention must be paid while moving simultaneously in the three directions. The bottom plot in Figure 7.9 shows the total thrust and the action of the transition controller just before each transition takes place (solid vertical lines). As expected, higher thrust is demanded in air to overcome the weight of the vehicle, while underwater the buoyancy force helps with this task, decreasing the energy consumption and allowing for higher operation time. This is one of the main advantages of this new kind of vehicles. Finally, Figure 7.10 shows the complete mission in a three dimensional (3D) representation, where the shaded (blue) volume indicates the water and the darker (green) planes represent the boundaries of the transition zone. It is seen in the figure that the vehicle response is more sluggish

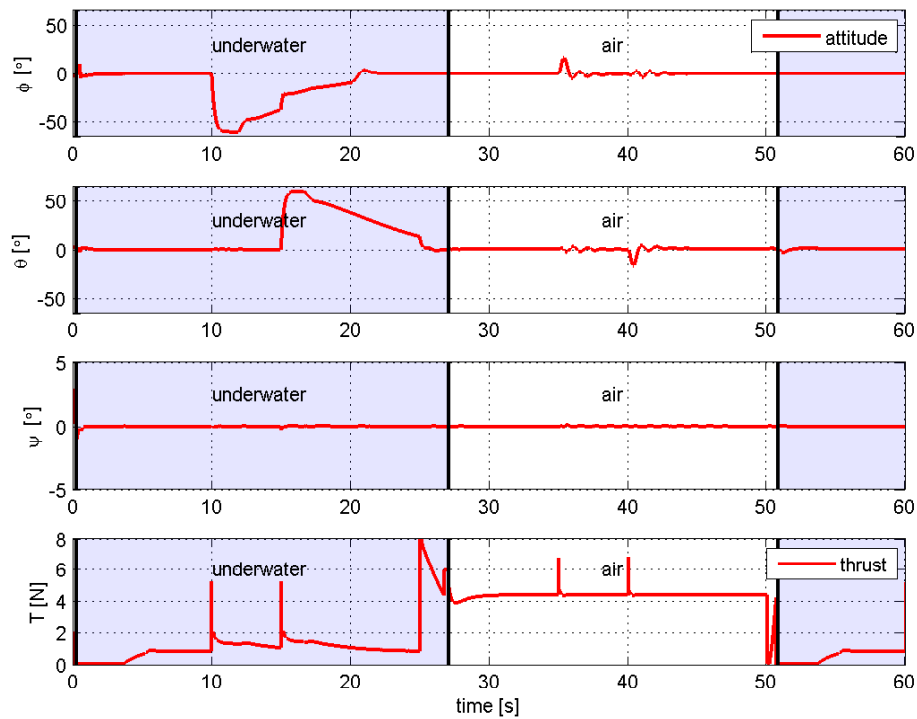


Figure 7.9: Orientation response (top three) and total thrust force (bottom) underwater and in air. Underwater movements require higher angular changes to overcome drag forces.

underwater when compared to air for the same initial error in the state. That is due to the additional drag of the water. Furthermore, saturation of the thrust outputs per motor limits the response of the vehicle. The simulation demonstrated the good performance of the control strategy for both mediums, while handling the drastic changes in density.

### 7.2.5 Hybrid Controller Experiments

The experimental platform described in the previous section was tested in real-time experiments to analyze the performance of the vehicle in air and underwater, in semi-autonomous mode, where the orientation and altitude are controlled automatically by PID controllers with compensation of the restoring forces where the desired orientation commanded by the human pilot.



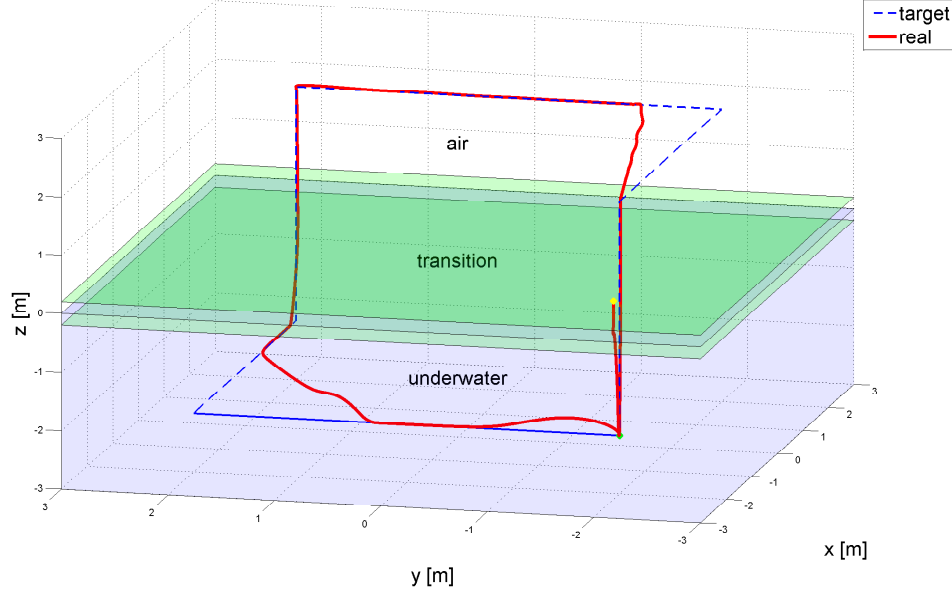


Figure 7.10: 3D representation of the mission. The vehicle starts close to the water (solid yellow cross mark), submerges immediately to  $-2m$ , moves  $2m$  first on  $y$  then on  $x$ , before emerging again to the air to displace  $2m$  on  $y$  then  $x$  and go back underwater. The darker (green) planes signal the boundaries of the transition zone, while the shaded (blue) volume represents the water.

Control on the  $x$  and  $y$  coordinates is done manually due to the lack of a precise estimation of the vehicle's position. Precise localization for an air/underwater vehicle is an interesting problem without a straightforward solution since GPS signals are not available underwater and acoustic sensors normally used for underwater localization are too heavy to be carried on flight by a small vehicle. Hence, only performance on altitude is tested for both media (air and water), along with the transition between them. The air-to-water transition strategy consists in switching off the motors once the water sensor on the bottom is triggered. The physical parameters of the multi-medium vehicle are summarized in Table 7.2.

Table 7.2: Experimental parameters.

$h_p$	$h$	$l$	$T_n[\%]$
0.153	0.204	0.27	35-65.7
$K_{p\phi}^1$	$K_{d\phi}^2$	$K_{pz}$	$K_{dz}$
$[0.25, 0.25, 0.30]$	$[0.002, 0.002, 0]$	$\{air : 1, water : 5\}$	0

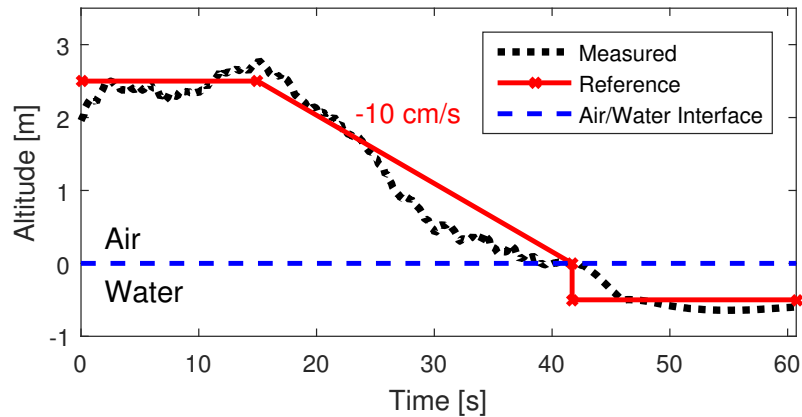


Figure 7.11: Real-time experiment on altitude. The vehicle hovers at an altitude of  $2.5m$  for  $15s$ , descends at a rate of  $10cm/s$  until it reaches the water level, transitions into the water, then it sinks until it approaches the depth reference of  $0.5m$  and maintains the desired depth for  $15s$ .

The mission consists of: holding a reference altitude of  $2.5m$  for  $15s$  by means of an altitude controller; slowly descending at a rate of  $10cm/s$ ; transitioning into the water and descending with rotors off until approaching the new depth reference of  $-0.5m$ ; and activating the altitude controller to maintain depth for  $15s$ . The performance of the altitude controller during the experiment is depicted in Figure 7.11. We can observe that the same vehicle is perfectly capable of evolving in both media and maintain its altitude. However, performance in air mode is affected by measurement noise, where is important to notice that the same pressure sensor is used for altitude measurements in both mediums, with an accuracy within one centimeter underwater and half a meter in air. The observed error in altitude hold during time  $25s - 40s$  is attributed to the increased measurement error of the pressure sensor while in air.

The throttle percentage is presented in Figure 7.12, where we can see when the transition mode is triggered (motors off) as soon as the water sensor is activated, in time  $42s - 45s$ . It is also interesting to notice the vast difference in throttle required for altitude hold in air versus maintaining depth underwater, mainly due to the increase in the buoyancy force associated with the change of density. Finally, Figure 7.13 shows the orientation of the vehicle during the mission. We can observe that the

attitude controller satisfactorily stabilize the vehicle's orientation for hover in air and underwater. The small perturbations observed are produced by manual commands from the pilot to correct for horizontal displacements. Also note that during the transition (42s – 45s) the orientation error is slightly increased, but once the vehicle goes out of the transition mode, it is able to recover and regain proper orientation.

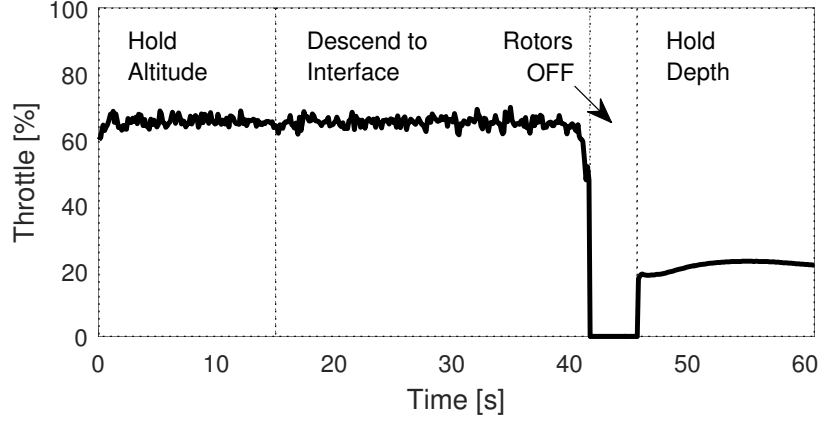


Figure 7.12: Throttle percentage output during the autonomous mission into water.

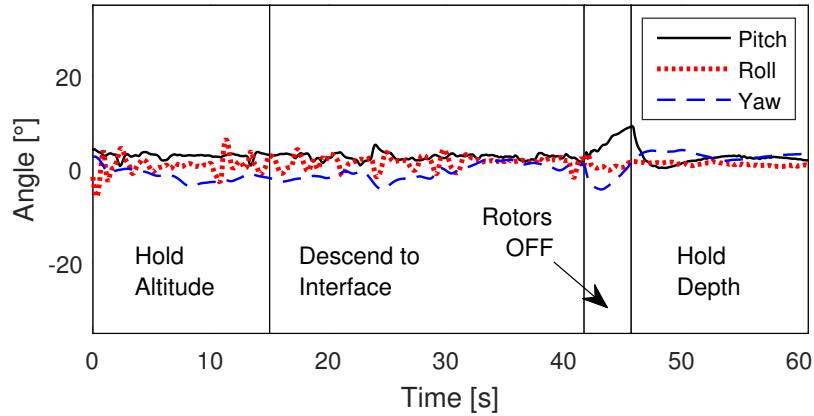


Figure 7.13: Orientation during the experiment into the water.

A transition-out strategy was also conducted. The mission consists of: starting 1m underwater; proceeding to a reference depth of -0.5m; going to a reference depth of 0m; switching to transition-out mode; and maintaining a 0.5m reference. The transition-out mode applies the transition out strategy where when the top water sensor registers water, the vehicle switches the rotors to air mode such that throughout the entire

process, a throttle ensures a thrust  $T_n$  as discussed in Section 7.2.2 that is capable of bringing the vehicle out of the water. The altitude/depth during the mission as measured by the vehicle is shown in Figure 7.14. It can be seen that while underwater, the vehicle converges to the desired reference very well, but with a slight offset. The offset can be attributed to the weight of the tether, which is not compensated for. The transition mode is shown by the shaded region and successfully brings the vehicle out of the water. However, once the vehicle exits the transition mode to hold altitude, it is observed that the altitude is mostly higher than the desired reference. The throttle

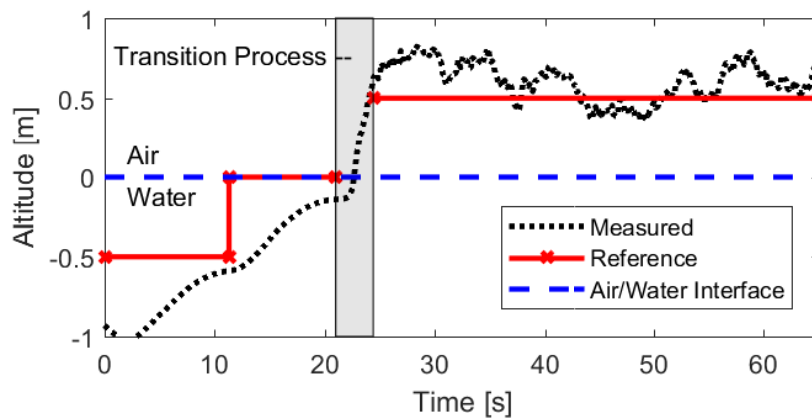


Figure 7.14: Real-time experiment on altitude. The vehicle starts 1m underwater, goes to 0.5m, goes to 0m, proceeds to transition out of the water, and goes to a reference of 0.5m.

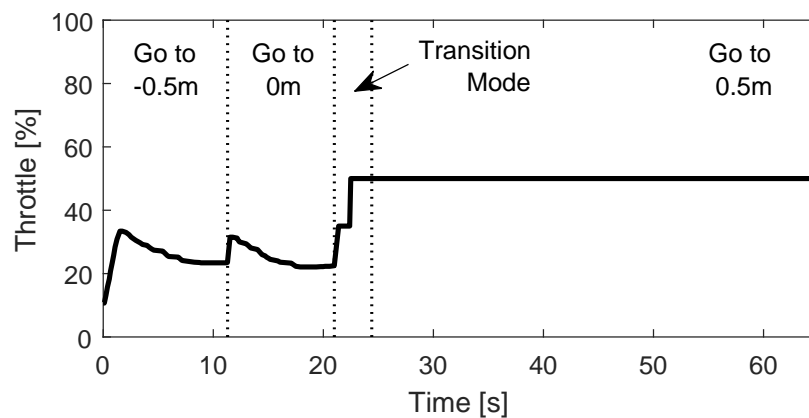


Figure 7.15: Throttle percentage output during the autonomous mission out of water.

for the mission out of the water is given in Figure 7.15. The regions  $0s$ - $12s$  and  $12s$ - $21s$  show a typical step response for the depth PID controller going to the  $-0.5m$  and  $0m$  targets, respectively. The transition period between  $21s$  and  $24s$  shows the throttle that is provided that is known to ensure that at any given time, the overall thrust produced is sufficient to compensate for the restoring forces. Finally, after the transition mode, the output throttle ensures that the vehicle maintains its altitude in the air. Throughout this experiment, which focuses on the transition of the vehicle, the altitude was controlled autonomously by the vehicle autopilot according to the desired references, but the position was controlled using manual inputs of roll, pitch and yaw. The resulting Euler angles corresponding to the orientation of the vehicle during the mission are shown in Figure 7.16, which shows that although the majority of the mission yielded small angle variations, the transition mode had an adverse effect on both roll and yaw. This is because the mission investigated a jump from water mode (low RPM) to air mode (high RPM) triggered by the vehicle water sensors and since the rotor response times vary slightly, such a jump caused a perturbation in the attitude of the vehicle, which was quickly corrected by the angle and torque controllers once all rotors were up to speed. These perturbations can be reduced by gradually increasing throttle from low RPM to high RPM. However, this experiment demonstrates that even without a smooth ramping up of the rotor angular velocities, the vehicle is still capable of traversing out of the water.

### 7.3 Improving response: Gain scheduling

In Section 7.1, a hierarchical PID controller for a single medium vehicle was highlighted and in Section 7.2, that same hierarchical PID controller was used in a framework that facilitates dealings with systems containing continuous-time and discrete characteristics, which included a transition strategy that relied on the discrete variable  $q$  that describes vehicle operation more (ie. air, transition, water). An important

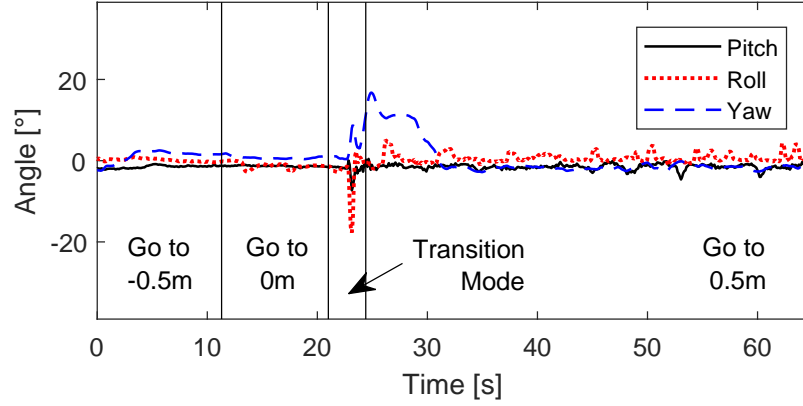


Figure 7.16: Orientation during the experiment out of the water.

consequence of operating in multiple mediums is in the fact that the tuning of the controllers may be vastly different depending on that mode of operation the vehicle is in. For instance, due to viscous damping in water, intuitively, the proportional gains will be likely be higher and the derivative gains will likely be lower than what it would be if it were in the air. Similarly, the added instability and interruption of rotor operation during transition will require a higher proportional gain and a more finely balanced yet higher derivative gain than in the air. Nevertheless, experiments will need to be carried out to verify these remarks.

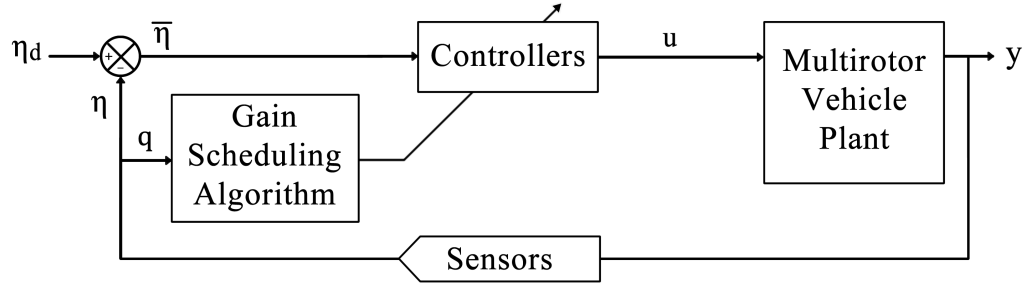


Figure 7.17: Block diagram showing the architecture of how gain scheduling could be applied to a multi-medium vehicle.

Consider the gain scheduling architecture shown in Figure 7.17, where a state error  $\bar{\eta}$  is fed to both the controller set and the gain scheduling block. Recall the framework from the hybrid system  $\mathcal{H}$ , where the discrete variable  $q \in \{1 : \text{air}, 2 : \text{transition}, 3 : \text{water}\}$  and changes according to the jump map  $G$  and jump set  $D$ . Then let the

set of gain matrices for the system be  $\mathbf{K}_{a_q}$ , where the subindex  $a$  identifies the gain matrix and the subindex  $q$  is the same as the discrete variable for the vehicle modes and designates which of the three gain matrices to pull values from when updating the main gain matrix  $\mathbf{K}_a$  in the controllers in the gain scheduling algorithm block. Another benefit of hybrid system representation is in that boolean sensors such as water sensors could be easily incorporated to drive essential behaviors.

## 7.4 Improving maneuverability: Quaternion controller

Thus far, the vehicle may be taken to be a hierarchical hybrid system with gain scheduling that allows the multi-medium vehicle to be responsive, regardless of which mode of operation it is in. However, maneuverability is key for a multi-medium vehicle and no matter how responsive the vehicle, if the attitude of the vehicle is bounded, then it is not very maneuverable, as is the case for many multi-rotors in the market.

**Attitude representations** The are many ways in which rigid body orientation can be represented, three of which are: Euler angles, a direction cosine matrix (DCM) and quaternions, which are composed of Euler parameters. In the literature, different representations for the pose of the vehicle can be found [45], where the Euler angles [6, 17], quaternions [5, 19, 13] and the special orthogonal group  $\text{SO}(3)$  [24, 15] are the most common ones. The importance of attitude representation is that it relates body rotations back to some orientation relative to a reference frame such as the inertial frame, thus enabling transformations based on the body frame rotations.

*Euler angle representation* is a three parameter descriptor of attitude containing angles of elementary rotations, such as roll  $\phi$ , pitch  $\theta$  and yaw  $\psi$ . Euler angles are often used because they are intuitive and carry values that are easily visualized. Unfortunately, they also contain singularities, which limit the angles of operation. Despite

this fact, this representation has been used for multirotors in the past due to the shallow roll and pitch angles at which they operate, which are far from the singularity limits. A physical example of Euler angle singularities is in gimbal lock where if two of the rotation axis align, one degree of freedom is lost. Mathematically, the singularity can be shown by first considering the governing dynamic equation for attitude with external torques  $\boldsymbol{\tau}$  shown in

$$\dot{\boldsymbol{\omega}} = [\mathbf{I}_{cm}]^{-1} (-\boldsymbol{\omega} \times \mathbf{I}_{cm}\boldsymbol{\omega} + \boldsymbol{\tau}) \quad (7.37)$$

In order to estimate relative vehicle position (even if just altitude) with respect to a reference frame such as the inertial frame, the thrust vector direction must be known and therefore, by association, the body orientation must also be known. The attitude dynamic equation (7.37) can be solved for  $\boldsymbol{\omega}$ , which is a measure of body angular rotation rate about the body frame axis  $\{\hat{\mathbf{b}}_1, \hat{\mathbf{b}}_2, \hat{\mathbf{b}}_3\}$ . Simply integrating this angular rate will yield a vector containing the angle of rotation that each body axis has undergone, which cannot be directly used to apply a coordinate transformation. Fortunately, the purpose of Euler angles is to make it possible to transform body angular rates  $\boldsymbol{\omega}$  to Euler angle rates  $\dot{\boldsymbol{\Phi}}$  according to

$$\dot{\boldsymbol{\Phi}} = \mathbf{Q}^{-1}\boldsymbol{\omega} \quad (7.38)$$

where the transformation matrix  $\mathbf{Q}^{-1}$  for the current Euler angle sequence is given by

$$\mathbf{Q}^{-1} = \begin{bmatrix} 1 & \frac{\sin \phi \sin \theta}{\cos \theta} & \frac{\cos \phi \sin \theta}{\cos \theta} \\ 0 & \cos \phi & -\sin \phi \\ 0 & \frac{\sin \phi}{\cos \theta} & \frac{\cos \phi}{\cos \theta} \end{bmatrix} \quad (7.39)$$

By inspection, it is evident that the transformation matrix contains singularities at  $\theta = \pm 90^\circ$ .



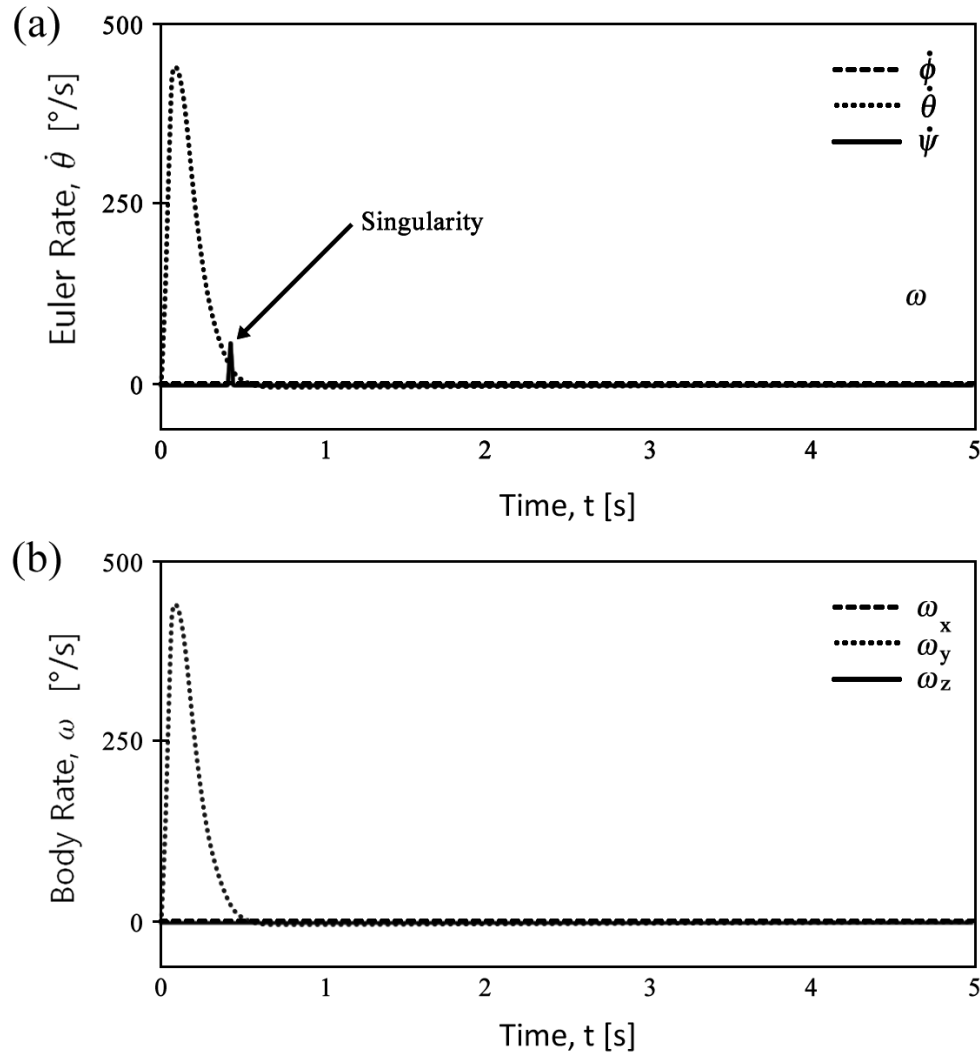


Figure 7.18: Two plots of demonstrating the singularity problem of Euler angles for a reference  $\theta = 90^\circ$  (initial condition is  $\theta = 0^\circ$ ) showing (a) the singularity of the Euler rate converted from the body rate and (b) the raw body rate of the system which for this scenario,  $\omega:2$  should be identical to  $\text{rpy\_rate}:2$ .

The singularity is visible in simulations as shown in Figure 7.18, where the Euler angle rate  $\dot{\Phi} = [\dot{\phi} \ \dot{\theta} \ \dot{\psi}]^T$  and body angular rate are plotted for a reference pitch angle of  $\theta = 90^\circ$ . Since only  $\hat{\mathbf{b}}_2$  (the body frame  $z$ -axis) rotation is taking place,  $\dot{\theta}$  in Figure 7.18(a) should be identical to  $\omega_y$  in Figure 7.18(b) except for the singularity, which appears in Figure 7.18(a). Note that although the singularity is an asymptote, the MATLAB<sup>®</sup> Simulink<sup>®</sup> automatic solver is able to minimize its effects (for the singularity test, the solver chosen was the “ode4 (Rung-Kutta)”). Nevertheless, the

singularity is still visible in the plots. Another disadvantage of Euler angles is that for a given transformation, there exists more than one set of Euler angles, which results in ambiguity. Therefore, Euler angles are unsuitable for attitude representation in a highly maneuverable multi-medium multirotor vehicle.

Euler angles prevent the vehicle from being capable of pitching more than  $90^\circ$ , thus inhibiting the vehicle from pointing the thrust vector downward, which is imperative for underwater operation. For instance, in previous tests, the set of missions which were possible are akin to the one depicted in Figure 7.19, where the vehicle maintains  $|\theta| < 90^\circ$  at all times.

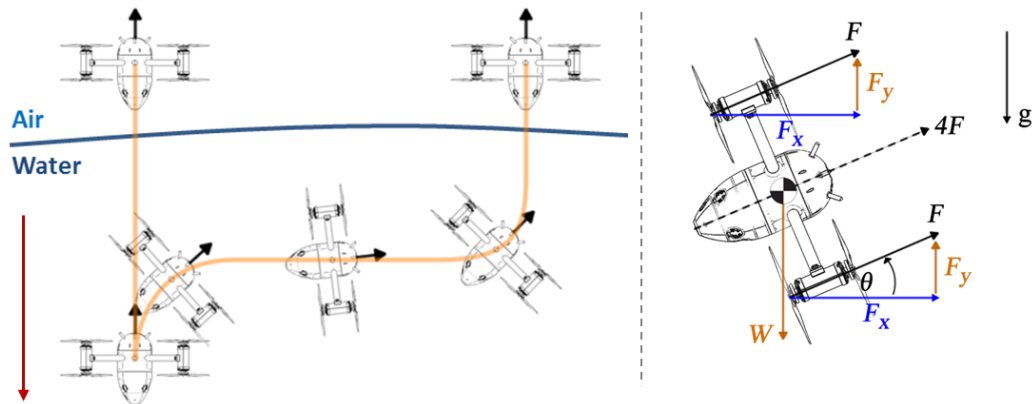


Figure 7.19: Example of a typical mission with pitch angle limited to  $< 90^\circ$ .

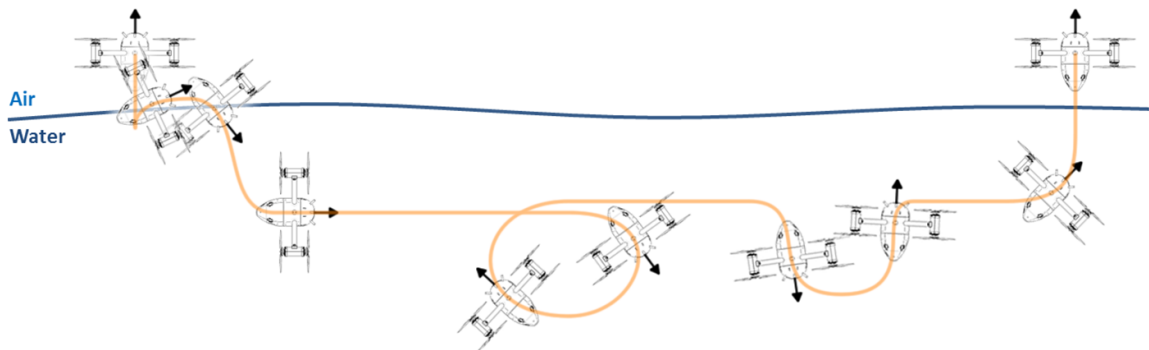


Figure 7.20: Example of a typical mission without pitch angle limit.

For actuators that only operate in one direction or better yet, that operate more efficiently in a single direction, it becomes advantageous to have the capability of

reorienting the thrust vector in any direction. Furthermore, for a neutrally buoyant vehicle that enters the water, depth control is not possible unless the thrust vector has a negative component along the  $\hat{\mathbf{a}}_3$  axis (or inertial  $z$ -axis) which can only happen if the vehicle is free to pitch and roll past  $90^\circ$ . This is the reason why the multi-medium multirotor vehicle prototypes were designed such that the weight is greater than the maximum buoyancy force.

However, in order to have arbitrary buoyancy, added maneuverability and resilience to unknown initial condition (ie. dropping the vehicle from an upside down state), it becomes necessary to employ a singularity-free representation, thus requiring alternatives to Euler angles in both the representation and control strategy (since some autopilots use a singularity-free representation but still use Euler angles directly in the controllers).

*The Direction Cosine Matrix (DCM)* is a nine-parameter matrix that offers attitude representation without singularities or ambiguity. In the past, it was avoided due to being computationally expensive but with advances in embedded systems, this is no longer a concern. A disadvantage is that the matrix is not intuitive and very little information can be extracted from the matrix elements by inspection.

*Quaternions* is a four-parameter representation consisting of a scalar and a three-dimensional imaginary part which together are called Euler parameters. They can be thought of as a rotation about an axis and offers a minimal representation for attitude. It does, however, contain ambiguity where a single orientation may be achieved with the two different quaternions. However, this is not an obstacle since quaternions make it easy to determine which direction yields the least angle of rotation about the axis of rotation.

None of the representations discussed are new and all have been heavily studied [45]. However, selecting a representation for use in a multi-medium multirotor vehicle is something that has not been done and is paramount to achieving better vehicle

maneuverability. Toward that end, a control strategy will be developed for quaternion representation, which was selected due to its minimal representation pseudo-intuitive parameters (ie. rotation about an axis). Note that moving forward, the quaternions of interest are unit quaternions, which are normalized.

### 7.4.1 Background on Quaternions

Quaternions are an extension of complex numbers and can be represented as

$$\mathbf{q} = q_0 + q_1\mathbf{i} + q_2\mathbf{j} + q_3\mathbf{k} = \begin{bmatrix} q_0 \\ \bar{\mathbf{q}} \end{bmatrix} = [q_0 \ q_1 \ q_2 \ q_3]^T \quad (7.40)$$

for a quaternion  $\mathbf{q}$ , with scalar and vector components  $q_0$  and  $\bar{\mathbf{q}}$ , respectively, and the axes  $\mathbf{i}$ ,  $\mathbf{j}$ ,  $\mathbf{k}$  satisfying

$$\begin{aligned} \mathbf{i}^2 = \mathbf{j}^2 = \mathbf{k}^2 &= -1 \\ -\mathbf{ij} = \mathbf{ji} = \mathbf{k}, \quad -\mathbf{jk} = \mathbf{kj} = \mathbf{i}, \quad -\mathbf{ki} = \mathbf{ik} = \mathbf{j} \end{aligned} \quad (7.41)$$

where a unit quaternion must also satisfy the unitary norm

$$|\mathbf{q}| = \sqrt{\mathbf{q}^T \mathbf{q}} = 1 \quad (7.42)$$

The quaternion is the most compact form to represent rotations without singularities. Given a unit axis of rotation  $\hat{\mathbf{k}}$  and an angle  $\alpha$ , the vector part of the quaternion of rotation  $\bar{\mathbf{q}}$  and the scalar part  $q_0$  satisfy

$$q_0 = \cos(\alpha/2), \quad \bar{\mathbf{q}} = \hat{\mathbf{k}} \sin(\alpha/2) \quad (7.43)$$

Rotation of a vector by a quaternion  $\mathbf{q}$  can be represented by means of a rotation

matrix  $\mathbf{R}(\mathbf{q})$  of the form

$$\mathbf{R}(\mathbf{q}) = \mathbf{I}_3 + 2q_0\bar{q}_\times + 2\bar{q}_\times^2 \quad (7.44)$$

where  $\mathbf{I}_3$  stands for the three by three identity matrix and  $\bar{q}_\times$  is the skew-symmetric matrix of the vector  $\bar{q}$ . Unit quaternions present ambiguities since they double cover the  $\text{SO}(3)$  group ( $\mathbf{R}(\mathbf{q}) = \mathbf{R}(-\mathbf{q})$ ). The quaternion rate is given by

$$\dot{\mathbf{q}} = \frac{1}{2}\mathbf{U}(\mathbf{q})\boldsymbol{\omega} \quad (7.45)$$

where the transformation matrix from body rates to quaternion rates is defined as

$$\mathbf{U}(\mathbf{q}) = \begin{bmatrix} \bar{q}^T \\ q_0\mathbf{I}_{3 \times 3} + \tilde{\bar{q}} \end{bmatrix} = \begin{bmatrix} -q_1 & -q_2 & -q_3 \\ q_0 & -q_3 & q_2 \\ q_3 & q_0 & -q_1 \\ -q_2 & q_1 & q_0 \end{bmatrix} \quad (7.46)$$

and the  $\tilde{\bar{q}}$  is the skew-symmetric matrix of the vector  $\bar{q}$ . It is very clear that  $\mathbf{U}(\mathbf{q})$  does not contain any singularities. The dynamic equations may be updated by utilizing  $\mathbf{R}(\mathbf{q})$  instead of  $\mathbf{R}(\Phi)$ .

### 7.4.2 Quaternion Control Laws

If the trajectory tracking position error is taken as  $\bar{\mathbf{r}} = \mathbf{r} - \mathbf{r}_d$ , then the PID controller for position control with compensation for the restoring forces (weight and buoyancy) may be defined as

$$\mathbf{T}_\Sigma = g(m - \rho V)\mathbf{e}_3 + m\ddot{\mathbf{r}}_d - \mathbf{K}_P\bar{\mathbf{r}} - \mathbf{K}_D\dot{\bar{\mathbf{r}}} - \mathbf{K}_I \int \bar{\mathbf{r}} dt \quad (7.47)$$

where the diagonal gain matrices  $\mathbf{K}_P$ ,  $\mathbf{K}_D$  and  $\mathbf{K}_I$  are positive definite. The desired thrust force is computed as the magnitude of the new virtual control input according

to

$$T_{\Sigma} = \|\mathbf{T}_{\Sigma}\| \quad (7.48)$$

and the desired quaternion can be extracted from the virtual input orientation as in [47].

Given a desired quaternion  $\mathbf{q}_d$ , the quaternion error may be defined as  $\tilde{\mathbf{q}} = \mathbf{q}_d^{-1}\mathbf{q}$  for which quaternion multiplication must be applied. The attitude control law may then be defined as the PD controller

$$\boldsymbol{\tau} = -\mathbf{K}_{D\omega}\boldsymbol{\Omega} - \mathbf{K}_{P\omega}sgn(\tilde{q}_0)\tilde{\tilde{\mathbf{q}}} \quad (7.49)$$

### 7.4.3 Quaternion Simulations: Aerial operation

In order to study the behavior of UAVs in different mediums and test the performance of the proposed control algorithms, several simulations were carried out with the help of MATLAB-Simulink<sup>®</sup>, using the Simulink model shown in Appendix B. In this section, we present some results for tracking of a spiral trajectory in both mediums, air and water.

As confirmed through Figures 7.21-7.24, aerial operation of multirotors requires the vehicle to operate in an orientation close to zero, directing the thrust force vector mostly upwards to compensate for gravity. Also, small angle variations will produce relatively large accelerations and fast response. The trajectory consists of a spiral with  $4m$  radius and  $20s$  period, as depicted in three-dimensions in Figure 7.24. The vehicle starts  $-2m$  away of the desired trajectory along the  $x$  axis,  $1m$  in  $y$  and  $2m$  in  $z$ , as can be appreciated in Figure 7.21, where the position (top) and the position errors (bottom) are depicted. We can observe that the errors quickly converge to zero and always remain small. In particular, the vehicle starts  $2m$  over the desired position in altitude, and has to turn upside down in order to reach the target reference. This

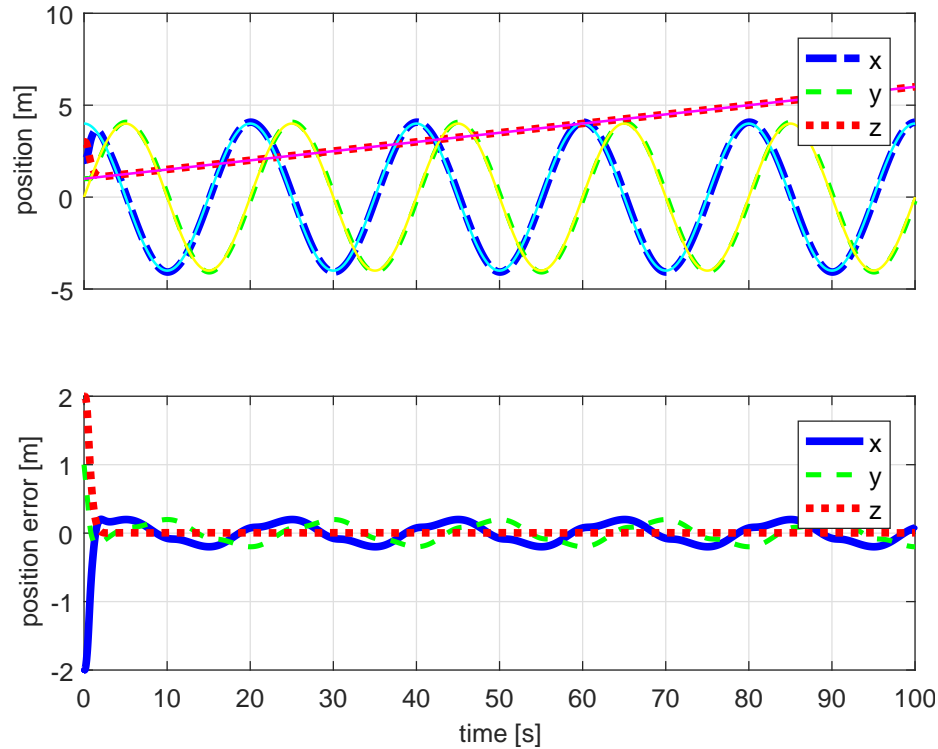


Figure 7.21: Trajectory tracking position in air. Real vs desired position (top). The position errors (bottom) quickly converge to zero and remain well bounded.

can be seen from Figure 7.22, where the vehicle's attitude (top) and the attitude errors (bottom) are depicted. Euler angles are used only to show the results in a more intuitive way. Once the drone is close to the desired trajectory, it turns again to direct the thrust vector opposite to the gravity, and the vehicle operates within small angles while in air. The orientation controller shows good performance as the errors quickly converge to the equilibrium point. Figure 7.23 presents the control inputs, with thrust on top and torques in the bottom. From this Figure, we can highlight that the thrust force converges to the magnitude of the weight of the vehicle and operates around this point, since and its main objective is to compensate for gravity.

#### 7.4.4 Quaternion Simulations: Underwater operation

In contrast with aerial operation, while underwater the vehicle must deal with larger drag and buoyancy forces produced by the significant increase in the medium density

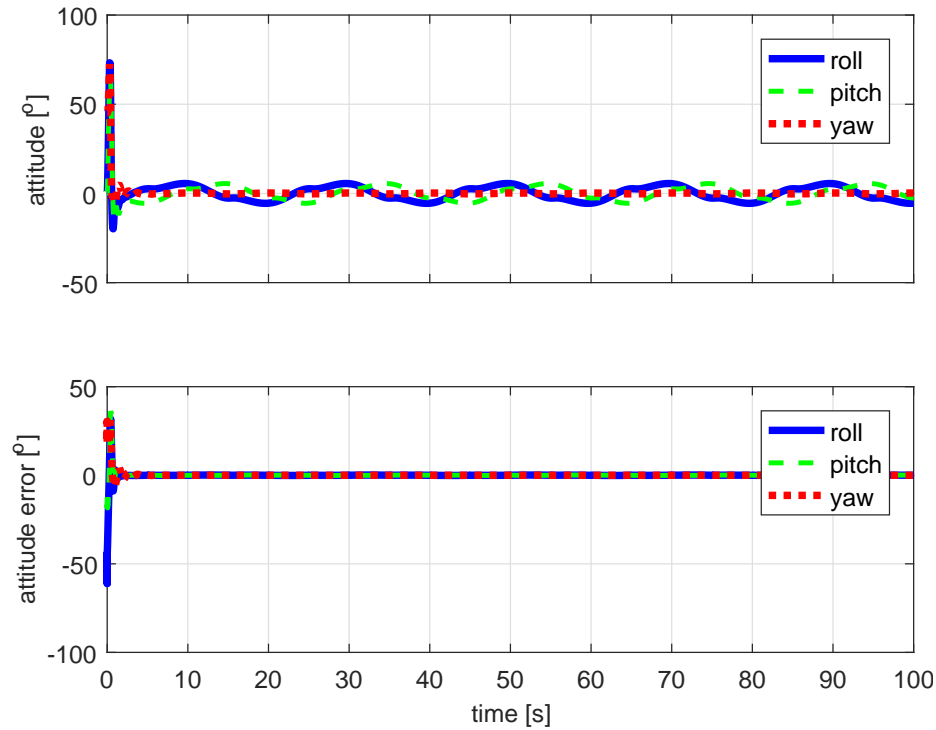


Figure 7.22: Trajectory tracking attitude in air. The desired orientation is provided by the position controller. The attitude (top) remains mostly close to the origin to compensate gravity. The attitude errors (bottom) quickly converge to the origin and stay close to zero.

of about three orders of magnitude. In this sense, the vehicle's behavior must vary as well. The buoyancy force can be used by design to compensate for gravity, leaving the thrust only to translate the vehicle. We consider a slightly buoyant vehicle ( $g < \rho V$ ), since this property allows for an easy recovery in case of system failure in a real scenario. Therefore, the only way for the drone to dive is to turn upside down directing the thrust force downwards. Also, the increased drag force acts against the motion of the vehicle, such that it is required to direct the thrust force vector in the direction of motion. Hence the importance of a singularity-free representation is highlighted in this case. All of this can be observed in Figs. 7.25-7.28, where the operation of the drone during a trajectory tracking mission underwater is studied. The desired trajectory, as seen in Figure 7.28 consists of a spiral with radius of  $4m$  and a period of  $50s$ . Note that the spiral chosen underwater is much slower than the one in air, because the motion of the vehicle is much slower underwater due to the larger drag



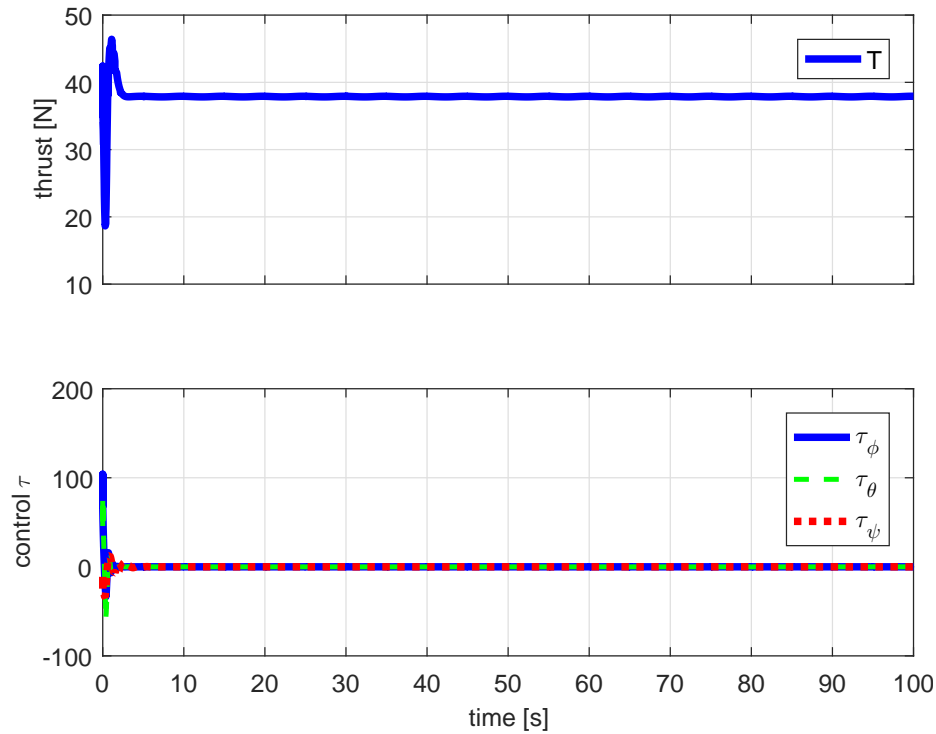


Figure 7.23: Trajectory tracking control inputs in air. The thrust force (top) is used mainly to compensate for gravity. Small changes in the torques inputs (bottom) produce significant motions of the vehicle in air.

force, as verified in Figure 7.25, where the position (top) and position errors (bottom) are presented. Although the trajectory tracking is accomplished satisfactorily, little decay is observed in the tracking performance, with slower response resulting in larger errors which is expected. As stated earlier, to best overcome the large drag force, the thrust force vector is directed towards the direction of motion, resulting in larger rotations. This can be analyzed from Figure 7.26, where the orientation of the drone (top) is shown along with the orientation errors. We can observe aggressive angle changes to drive the vehicle to the desired position, specially in roll. It is interesting to notice that the thrust force was saturated to the maximum during the entire mission, as can be seen in Figure 7.27 in which the control input signals are presented, with thrust on top and torques on the bottom.

From the simulations we can conclude that the proposed control strategies are suitable for trajectory tracking of under-actuated UAVs with full torque actuation and a

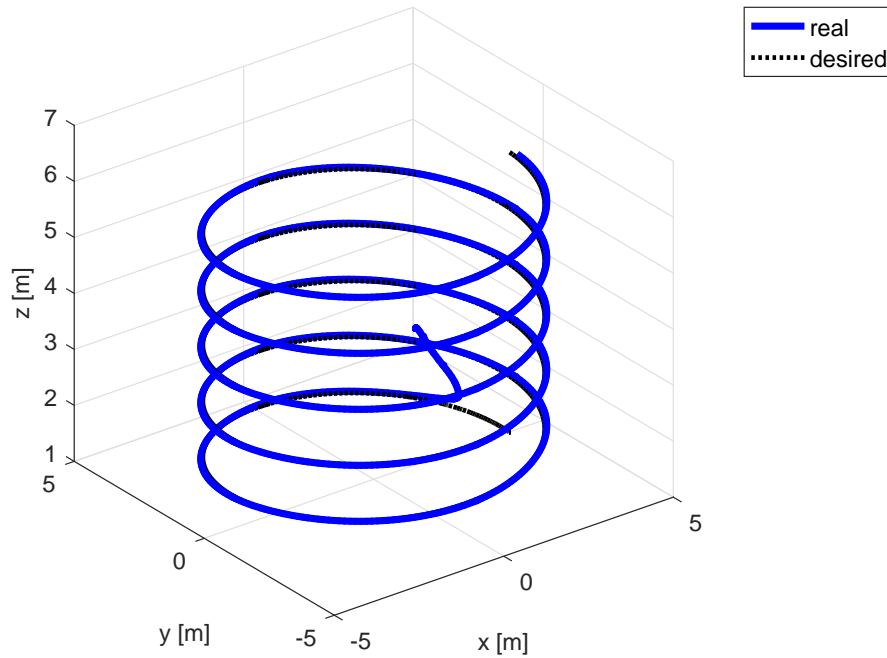


Figure 7.24: 3D visualization of the trajectory tracking in air. The desired trajectory consists of a spiral with  $4m$  amplitude and  $20s$  period. The vehicle is able to follow the spiral trajectory with good performance.

single thrust force, in multiple mediums. We can also appreciate the main effects of the density change for different mediums, and the resulting difference in the behavior of the vehicle.

### 7.4.5 Quaternion Experiments

To verify the results of the numerical simulation, experiments were carried out on the fifth prototype iteration of the experimental platform, the “Naviator-NV5”. The rotor configuration and corresponding multirotor dynamics of the actual vehicle align closely with the dynamic model presented in previous sections. To reiterate briefly, some of the most important characteristics of the Naviator-NV5 are in its customized rotor driver firmware, autopilot firmware and rugged watertight construction, which allow the vehicle to operate at low rotor speeds when deep underwater and high rotor speeds when in the air. Additional water and altitude/depth sensors together with

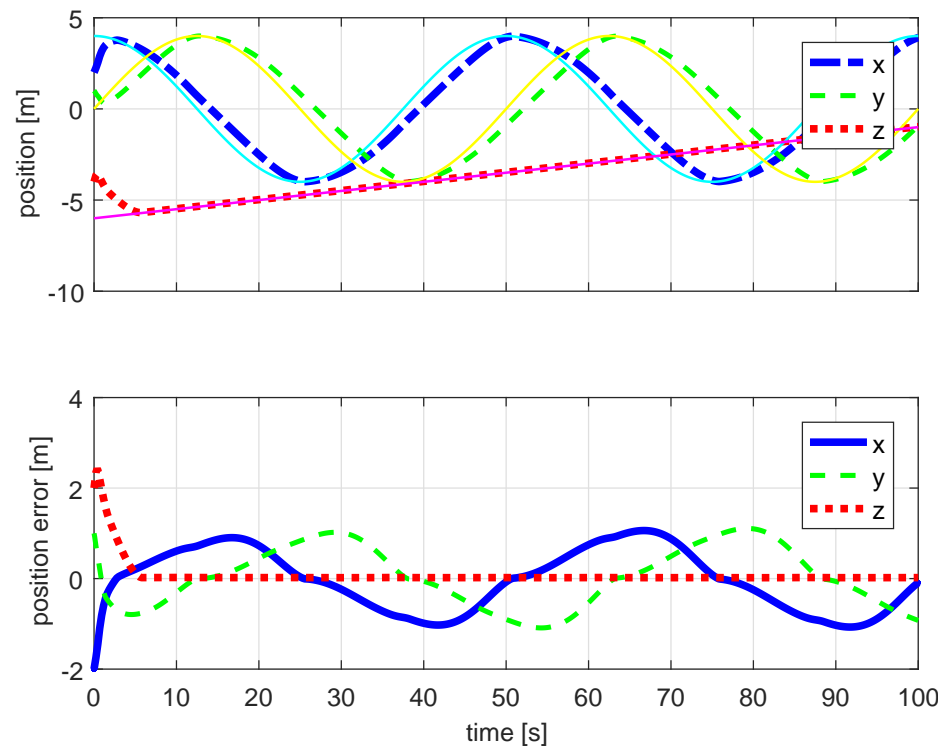


Figure 7.25: Trajectory tracking position underwater. Real vs desired position (top). The position errors (bottom) remain bounded, but the increased drag force underwater slows down the system response, resulting in larger errors.

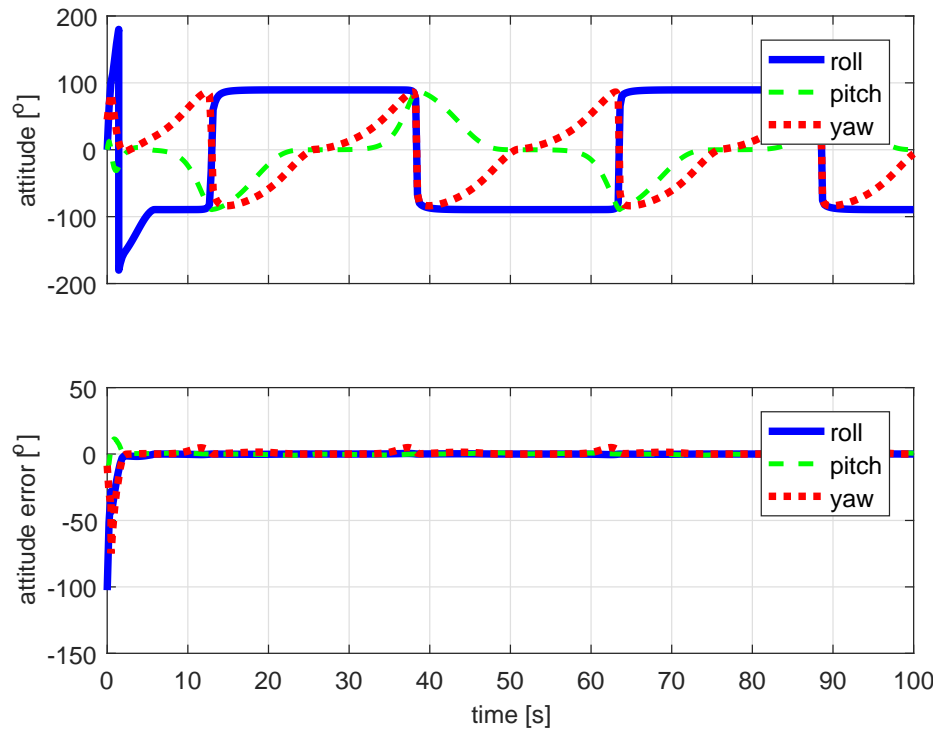


Figure 7.26: Trajectory tracking attitude underwater. The desired orientation is provided by the position controller. Due to the increased drag and buoyancy forces underwater, the thrust force must be pointed in the direction of motion, hence, more aggressive orientations are commanded (top). The attitude errors (bottom) quickly converge to the origin and remain well bounded.

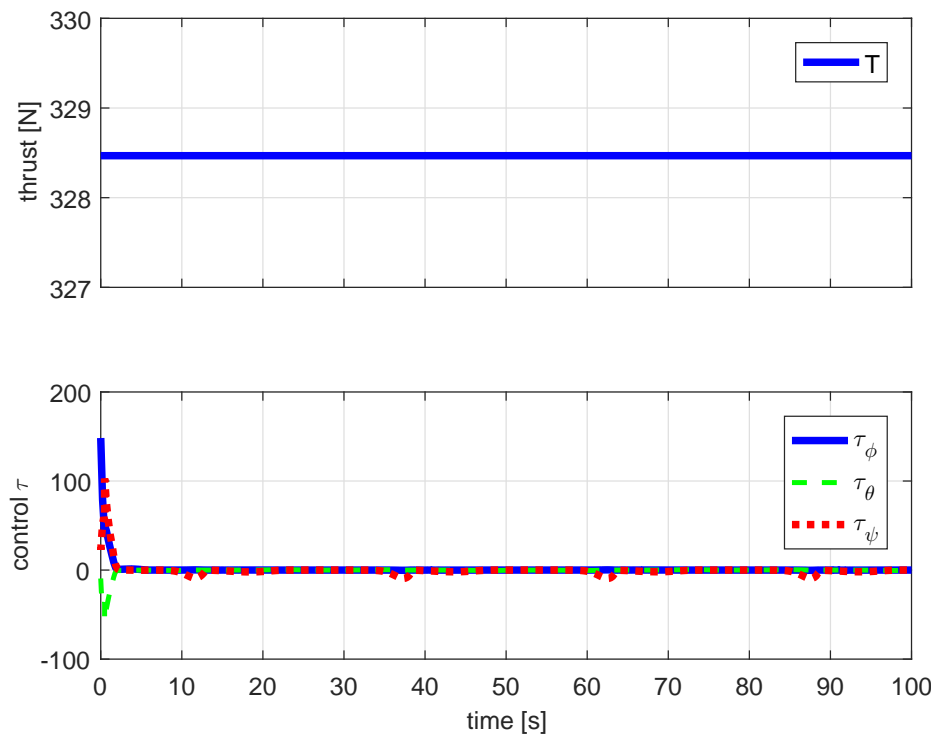


Figure 7.27: Trajectory tracking control inputs underwater. In order to overcome the larger drag force and keep track of the desired position, the thrust force (top) is saturated to its maximum and oriented in the direction of motion. Torques inputs (bottom).

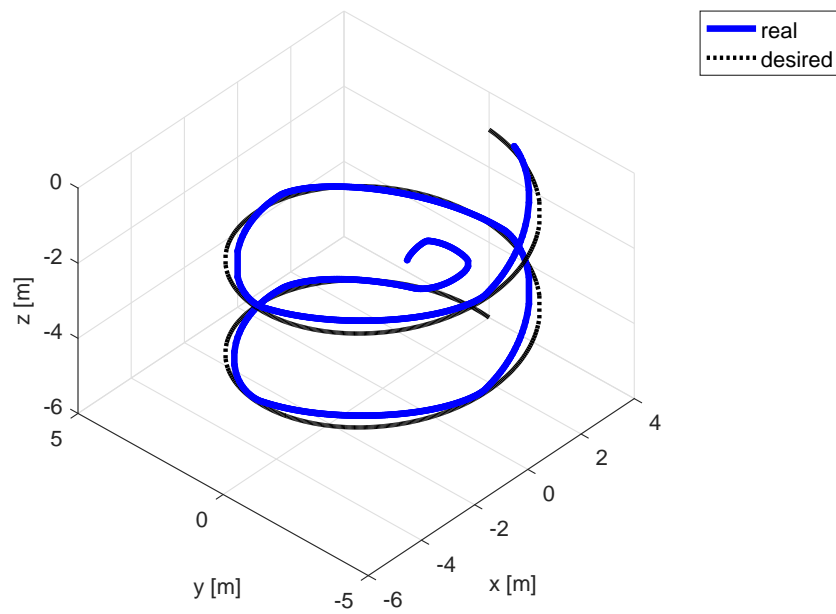


Figure 7.28: 3D visualization of the trajectory tracking underwater. The desired trajectory consists of a spiral with  $4m$  amplitude and  $50s$  period. The larger drag force underwater acts as a natural damper to the system, hindering the motion of the vehicle. Henceforth, only slower trajectories are accomplished underwater.

the inertial measurement units make it possible to directly measure four states of the vehicle  $\mathbf{y}_m = [\omega^T \ z]^T$ , which are utilized in the proposed quaternion control strategies. Prior to using quaternions, the vehicle was limited to conducting missions with pitch angles limited to  $|\theta| < 90^\circ$  due to Euler angle singularities, which meant that it was impossible for the thrust vector to have a negative vertical component to drive the vehicle downward in the case of neutral or positive buoyancy. Therefore, the vehicle was designed to be slightly negatively buoyant and essentially hover in water, but with very little thrust required. In that scheme, to descend deeper into the water, the rotors spin extremely slow or not at all, only turning on to correct attitude during the descent. More details on the platform and the angle control, using Euler angles, of the Naviator-NV5 with angles approaching (but not hitting) the singularity while maintaining depth is found in [29]. With quaternions, the singularity problem is no longer a concern and to demonstrate the ability of the vehicle to go further than  $90^\circ$  on the pitch, a vertical loop maneuver underwater was showcased experimentally as shown in Figure 7.29.

Although transition in and out of water is depicted, it has already been shown in prior works that the vehicle is capable of seamless transition and since the topic is

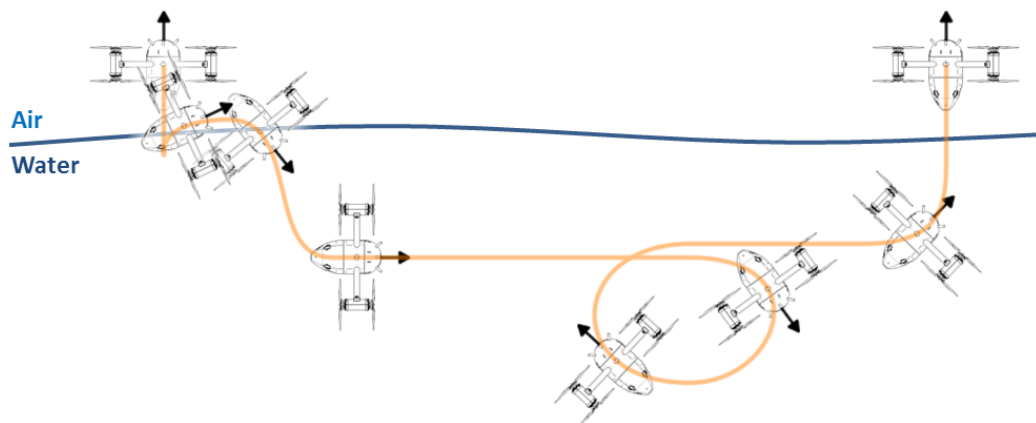


Figure 7.29: An illustration of the mission conducted experimentally showing the Naviator conducting a vertical loop underwater.

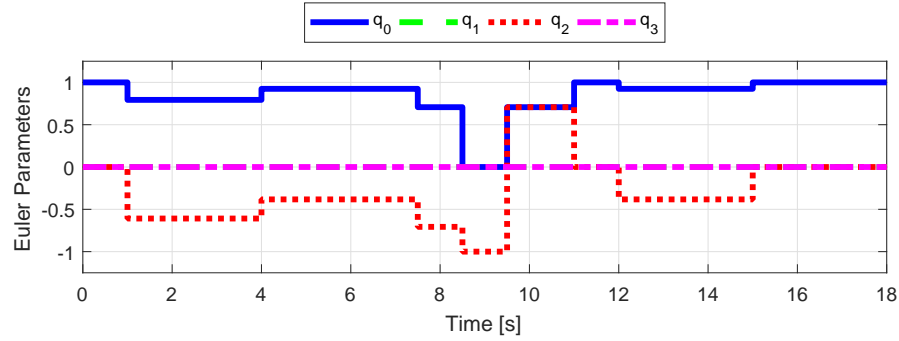


Figure 7.30: The input quaternion references throughout the underwater vertical loop mission showing the value of each Euler parameter over time.

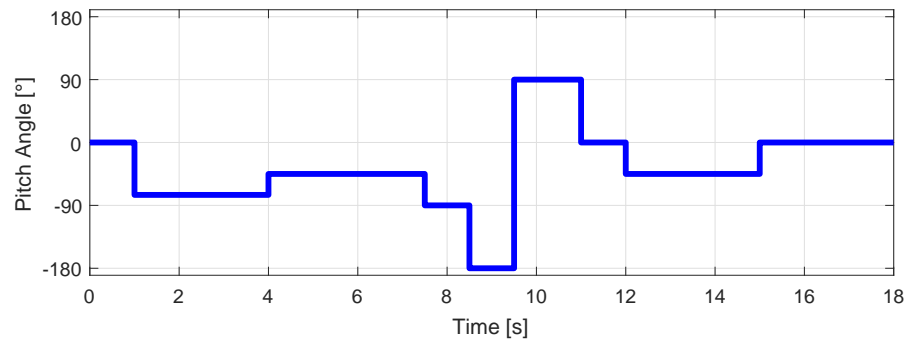


Figure 7.31: The value of the pitch angle throughout the underwater vertical loop mission obtained from converting the Euler parameters in Figure 7.30 to Euler angle where throughout the mission, the roll and yaw references are zero.

on singularity-free control of a multi-medium vehicle, the focus will be on the underwater vertical loop. To drive the vehicle through the vertical loop, quaternion step inputs were uploaded to the Naviator-NV5 and the vehicle executed these inputs autonomously. Throughout the mission, the depth input reference was fixed and during moments when the vehicle's thrust vector vertical component made it impossible to control depth, a default fixed throttle value was used. The quaternion inputs are shown in Figure 7.30 and their converted values in a more intuitive pitch angle is shown in Figure 7.31.

A video of the experiment showing several runs of the same mission can be found in <https://youtu.be/QwOMgMPBoBQ> and confirms that a vertical loop was successfully executed and matches very closely qualitatively with the desired mission shown in



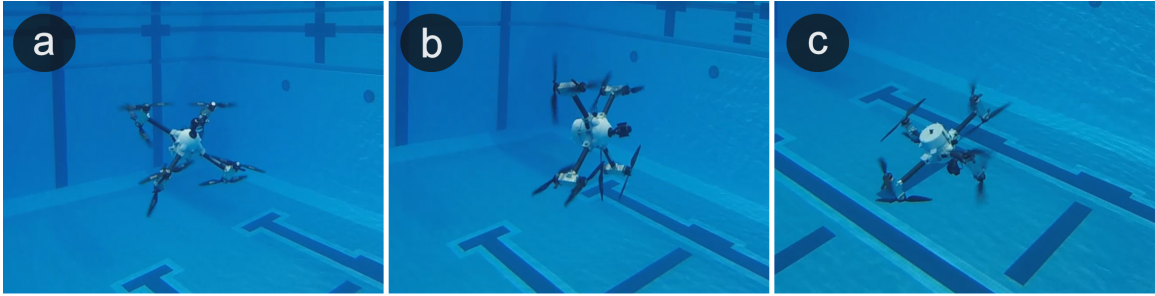


Figure 7.32: Experimental platform "Naviator" performing a flip maneuver underwater, shown approaching a forward pitch of  $45^\circ$  in (a),  $90^\circ$  in (b) and  $180^\circ$  in (c).

Figure 7.29. Snapshots of the mission video at key moments are shown in Figure 7.32. Furthermore, despite a step reference being used as the input instead of a gradual trajectory, the vehicle was able to converge to the desired state satisfactorily, but with some oscillations.

This same mission was conducted in a simulation, which showed similar path, as shown in Figure 7.34. Furthermore, it is seen in Figure 7.33 that the quaternion controller responds well and that for each step input, the quaternion errors are able to converge to zero. However, if the same orientation references are given to the Euler angle based controller, the resulting path shown in Figure 7.36 achieves the same path up until the point that the pitch angle becomes greater than or equal to zero, after which the vehicle loses control and drifts downward. That is because the Euler angle controller was modeled after the ArduCopter APM autopilot Euler angle controller, which turns off the rotors when the pitch angle exceed an absolute value of  $90^\circ$ . This is clearly seen in Figure 7.35, where as soon as the pitch angle becomes  $-90^\circ$ , it fails to properly go to the desired references. Therefore, quaternion representation and quaternion controllers are much more suitable for use in multi-medium vehicles than Euler angles due to the increased maneuverability with singularity-free representation.

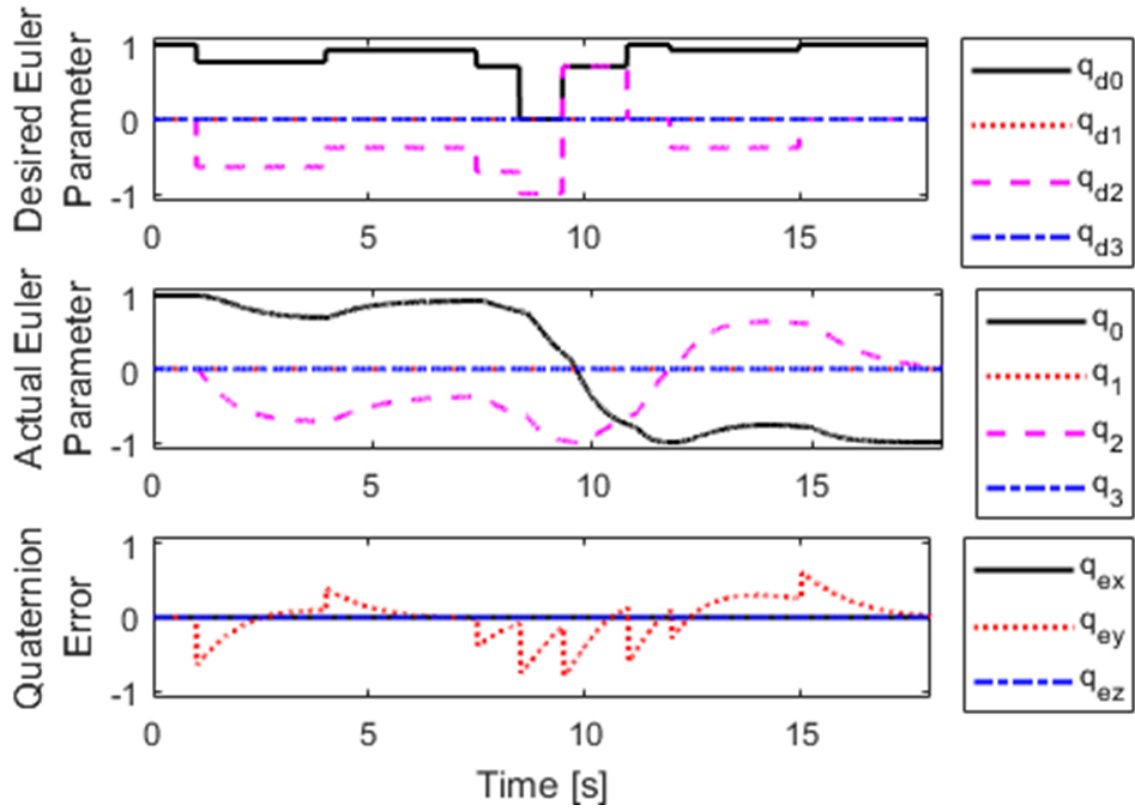


Figure 7.33: Plots of the desired quaternion Euler parameters, actual Euler parameters and the quaternion error for a mission of a vertical loop underwater similar to the experiment, using a quaternion controller.

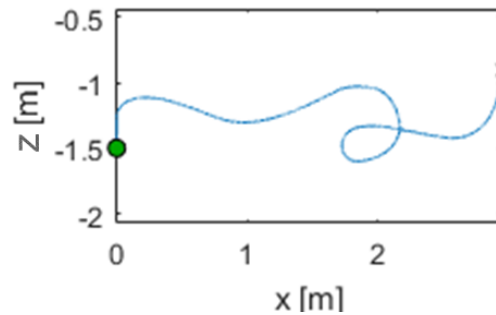


Figure 7.34: Plot of the path obtained for a mission of a vertical loop underwater similar to the experiment, using a quaternion controller.

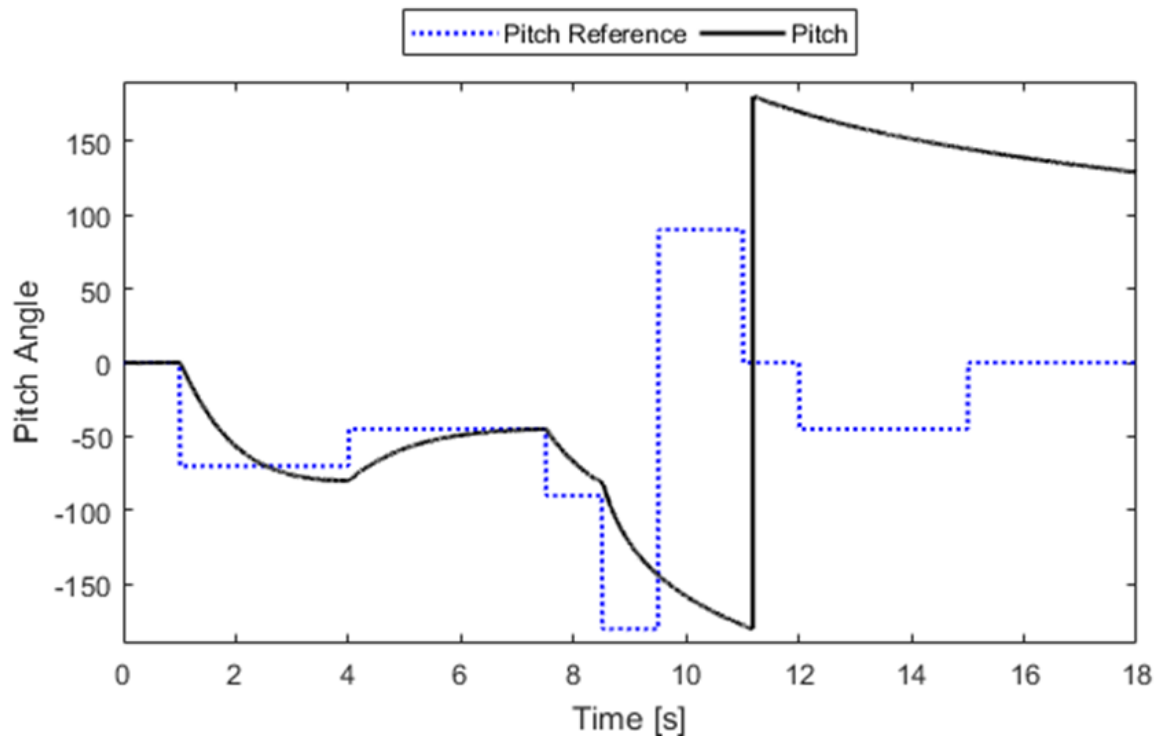


Figure 7.35: Plot of the desired pitch angle references and pitch angle response for a mission of a vertical loop underwater similar to the experiment, using an Euler angle controller.

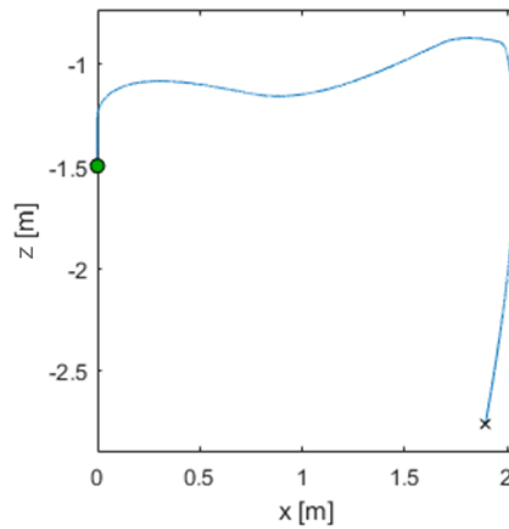


Figure 7.36: Plot of the path obtained for a mission of a vertical loop underwater similar to the experiment, using an Euler angle controller.

## Chapter 8

### Conclusion

A multi-plane propulsion system was introduced that ensures seamless transition and some basic requirements on designing multi-medium multirotor vehicles were briefly discussed, which touched on hardware level components as well as firmware for the autopilot and the motor drivers.

Five prototypes have been developed and these fully developed platforms adopted several control schemes that when aggregated, properly handle the continuous-discrete behavior that a multi-medium vehicle entails. First, a standard multirotor controller employing a hierarchical PID controller was formalized. Next, this hierarchical controller was incorporated into a discrete-continuous system through a hybrid controller. Then, a gain scheduling algorithm was added by exploiting the discrete variables established by the hybrid system. Finally, a singularity-free quaternion representation was employed such that when combined with a hierarchical hybrid quaternion controller with gain scheduling will render the vehicle highly maneuverable, agile and adept at each medium in which it operates.

Ultimately, it was found that using quaternions as the singularity-free attitude representation, the vehicle performance did not deteriorate and the vehicle's agility was greatly increased (it allowed the vehicle to operate in any orientation, whereas before it was limited to orientation within the upper hemisphere. Furthermore, the drag coefficient was found to be within the expected range between 0.5 and 1.5 for Reynolds numbers near  $10^4$ , which supports the overall proposed dynamic model.

## 8.1 Future work

There are some interesting areas to investigate which are outside the scope of the current work, namely:

1. Drag and surface tension at the air-water interface. It would be beneficial to characterize all of the forces that are involved with transitioning the vehicle in and out of water.
2. Decreasing the drag coefficient. In this work, a small study was conducted that provided an indication of what the current drag on the vehicle is. Having a vehicle with a drag coefficient akin to that of a teardrop would vastly increase underwater performance, endurance, and range since the teardrop has one of the lowest drag coefficients known. For instance, an investigation could be done on the pressure vessel as a teardrop and the arms as an airfoil.
3. Efficiency of power system on the vehicle is an area that could benefit from further development. If the rotor system efficiency could be maximized through both firmware and mechanical changes (ie. introduction of a transmission), then again, it would vastly increase underwater performance, endurance, and range.
4. Lastly, in the electronics space, communication and localization without the need of an expensive acoustic equipment remains a challenge.

## Bibliography

- [1] D. Auld and K. Srinivas. Aerospace, mechanical and mechatronic engineering. [http://www-mdp.eng.cam.ac.uk/web/library/enginfo/aerothermal\\_dvd\\_only/aero/fprops/introvisc/node11.html](http://www-mdp.eng.cam.ac.uk/web/library/enginfo/aerothermal_dvd_only/aero/fprops/introvisc/node11.html), 2005. University of Sydney. Accessed: 2017-11-17.
- [2] H. Baruh. *Applied Dynamics*. CRC Press, New York, United States, 2015.
- [3] R. Bogue. Underwater robots: a review of technologies and applications. *Industrial Robot: An International Journal*, 42(3):186–191, 2015.
- [4] G. Brown. Georgia Tech UAV research facility. <http://www.uavrf.gatech.edu/>, 2015. Accessed: 2017-01-05.
- [5] P. Cassau, R. Sanfelice, R. Cunha, D. Cabecinhas, and C. Silvestre. Robust global trajectory tracking for a class of underactuated vehicles. *Automatica*, 2015.
- [6] P. Castillo, R. Lozano, and A. Dzul. *Modelling and control of mini-flying machines*. Springer-Verlag, London, 2005.
- [7] C. S. Chin. *Control System Fundamentals*. CRC Press, 2012.
- [8] E. K. Chong and S. H. Zak. *An introduction to optimization*, volume 76. John Wiley & Sons, 2013.
- [9] DARPA. Broad agency announcement: Submersible aircraft, 2008.

- [10] P. Drews-Jr, A. Neto, and M. Campos. Hybrid unmanned aerial underwater vehicle: modeling and simulation. *International Conference on Intelligent Robots and Systems (IROS)*, 2014.
- [11] D. Edwards. Flimmer: a flying submarine. *Naval Research Laboratory Spectra*, pages 6–9, 2014.
- [12] A. Fabian, Y. Feng, E. Swartz, D. Thurmer, and R. Wang. Hybrid aerial underwater vehicle (mit lincoln lab). *SCOPE Projects*, 2012.
- [13] O.-E. Fjellstad and T. I. Fossen. Quaternion feedback regulation of underwater vehicles. *Proceedings of the Third IEEE Conference on Control Applications*, 1994.
- [14] T. I. Fossen. *Guidance and Control of Ocean Vehicles*. John Wiley and sons, England, 1994.
- [15] E. Frazzoli, M. Dahleh, and E. Feron. Trajectory tracking control design for autonomous helicopters using a backstepping algorithm. *Proceedings of the American Control Conference*, 2000.
- [16] R. Goebel, R. Sanfelice, and A. Teel. *Hybrid Dynamical Systems: Modeling, Stability and Robustness*. Princeton University Press, 2012.
- [17] T. Hamel, R. Mahony, R. Lozano, and J. Ostrowsky. Dynamic modeling and configuration stabilization for a X4-flyer. *15th Triennial IFAC world congress*, 2002.
- [18] E. N. Johnson. New UAV can launch from underwater for aerial missions. <http://www.jhuapl.edu/newscenter/pressreleases/2016/160317.asp>, 2016. Accessed: 2016-03-17.

- [19] S. Joshi, A. Kelkar, and J. Wen. Robust attitude stabilization of spacecraft using nonlinear quaternion feedback. *IEEE Transactions on Automatic control*, 40(10), 1995.
- [20] R. S. K. Alexis, C. Huerzeler. Hybrid predictive control of a coaxial aerial robot for physical interaction through contact. *Control Engineering and Practice*, 32: 96–112, 2014.
- [21] F. Kendoul, D. Lara, I. Fantoni, and R. Lozano. Nonlinear control for systems with bounded inputs: real-time embedded control applied to UAVs. *Proceedings of the 45th IEEE Conference on Decision and Control*, 2006.
- [22] Kollmorgen. Sea sentry organic submarine launched UAV, 2009.
- [23] V. Kumar and N. Michael. Opportunities and challenges with autonomous micro aerial vehicles. *International Symposium on Robotics Research*, 2011.
- [24] T. Lee. Global exponential attitude tracking controls on  $so(3)$ . *IEEE Transactions on Automatic Control*, 60(10), 2015.
- [25] T. Lee, M. Leoky, and N. H. McClamroch. Geometric tracking control of a quadrotor UAV on  $SE(3)$ . In *Decision and Control (CDC), 2010 49th IEEE Conference on*, pages 5420–5425. IEEE, 2010.
- [26] U. Lei, C. Yang, and K. Wu. Viscous torque on a sphere under arbitrary rotation. *Appl. Phys. Lett.*, 89, 2006.
- [27] G. J. Leishman. *Principles of helicopter aerodynamics with CD extra*. Cambridge university press, 2006.
- [28] R. Mahony, V. Kumar, and P. Corke. Multirotor aerial vehicles. *IEEE Robotics and Automation magazine*, 20(32), 2012.



- [29] M. Maia, D. Mercado, and F. Diez. Design and implementation of multirotor aerial-underwater vehicles with experimental results. *International Conference on Intelligent Robots and Systems (IROS)*, 2017.
- [30] M. M. Maia. Viability of a multi-medium (air and water) unmanned aerial/underwater vehicle (UAV/UUV), 2013.
- [31] D. Majumdar. U.s. navy launches UAV from a submarine. *U.S. Naval Institute News*, 2013.
- [32] D. Mellinger and V. Kumar. Minimum snap trajectory generation and control for quadrotors. In *Robotics and Automation (ICRA), 2011 IEEE International Conference on*, pages 2520–2525. IEEE, 2011.
- [33] D. Mercado, P. Castillo, R. Castro, and R. Lozano. 2-sliding mode trajectory tracking control and ekf estimation for quadrotors. *In the 19th IFAC World Conference*, 2014.
- [34] C. C. Murray and A. G. Chu. The flying sidekick traveling salesman problem: Optimization of drone-assisted parcel delivery. *Transportation Research Part C: Emerging Technologies*, 54:86–109, 2015.
- [35] R. Naldi, M. Furci, R. Sanfelice, and L. Marconi. Global trajectory tracking for underactuated VTOL aerial vehicles using a cascade control paradigm. *52nd IEEE Conference on Decision and Control*, 2013.
- [36] G. Petrov. Flying submarine. *Journal of eet*, 1995.
- [37] O. Rawashdeh. Embedded systems research laboratory: Loon copter. <https://sites.google.com/a/oakland.edu/oar/>, 2015. Accessed: 2016-03-17.
- [38] J. Roskam. Airplane flight dynamics and automatic flight controls. In *Airplane*

- Flight Dynamics and Automatic Flight Controls*, chapter 2, pages 25–31. Roskam Aviation and Engineering Corporation, USA, 1982.
- [39] S. Seager. *Exoplanet atmospheres: physical processes*. Princeton University Press, 2010.
  - [40] R. Siddall and M. Kova. Launching the aquamav: bioinspired design for aerial-aquatic robotic platforms. *Bioinsp. Biomim.*, 9(3), 2014.
  - [41] D. Smith and R. Sanfelice. Autonomous waypoint transitioning and loitering for unmanned aerial vehicles via hybrid control. *AIAA Guidance, Navigation and Control Conference*, 2016.
  - [42] H. P. Tan, R. Diamant, W. K. G. Seah, and M. Waldmeyer. A survey of techniques and challenges in underwater localization. *Ocean Eng.*, 38(14):1663–1676, 2011.
  - [43] G. Vallis. *Atmospheric and oceanic fluid dynamics: Fundamentals and large-scale circulation*, 2006.
  - [44] A. van der Shaft and J. Schumacher. *An Introduction to Hybrid Dynamical Systems*. Springer, 2000.
  - [45] J.-Y. Wen and K. Kreutz-Delgado. The attitude control problem. *IEEE Transactions on Automatic control*, 36(10):1148–1162, 1991.
  - [46] S. Wood. *Autonomous underwater gliders*. In-Tech, Vienna, Austria, 2009.
  - [47] S. Zhao, A. Dong, and J. Farrell. Quaternion-based trajectory tracking control of VTOL-UAVs using command filtered backstepping. *American Control Conference (ACC)*, 2013.

## Appendix A

### Simulink Model Employing an Euler angle Controller

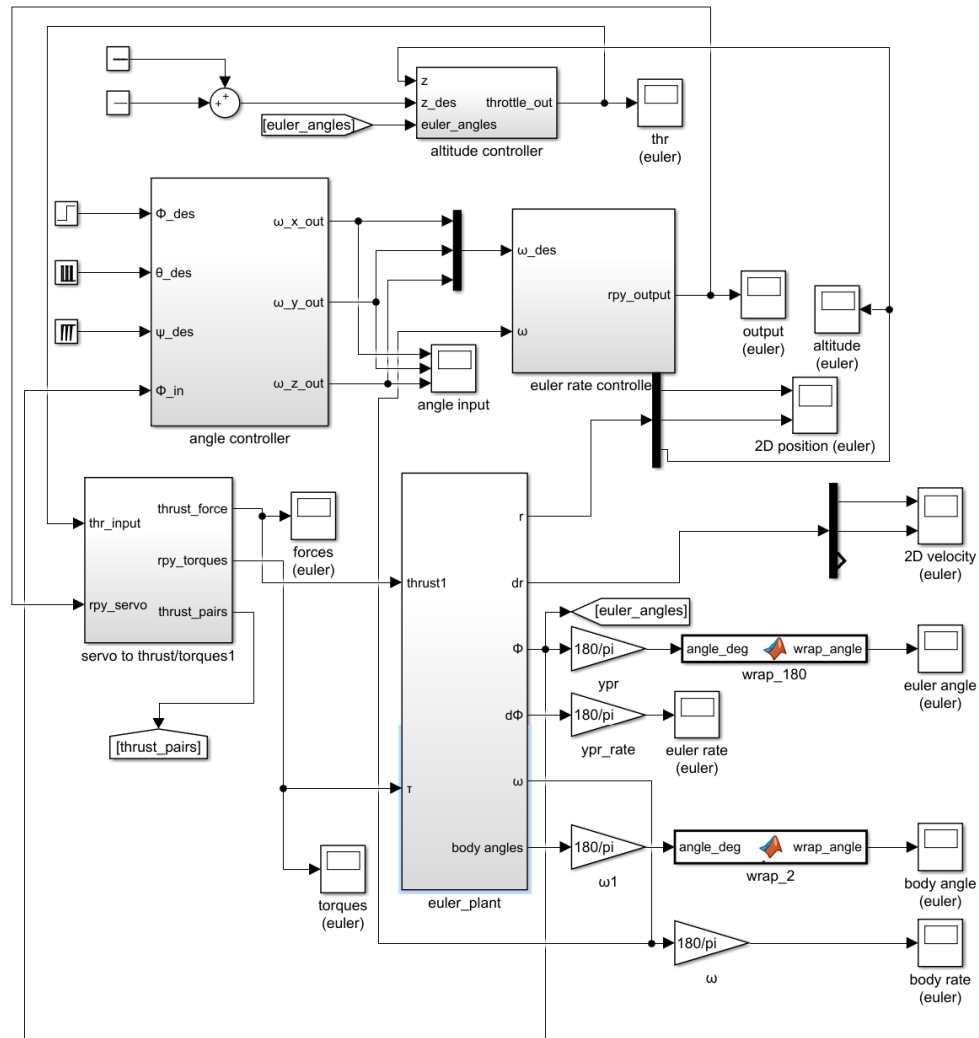


Figure A.1: Snapshot of the outermost layer of the Simulink model created to model the Euler angle controller on a multi-medium vehicle.

## Appendix B

### Simulink Model Employing a Quaternion Controller

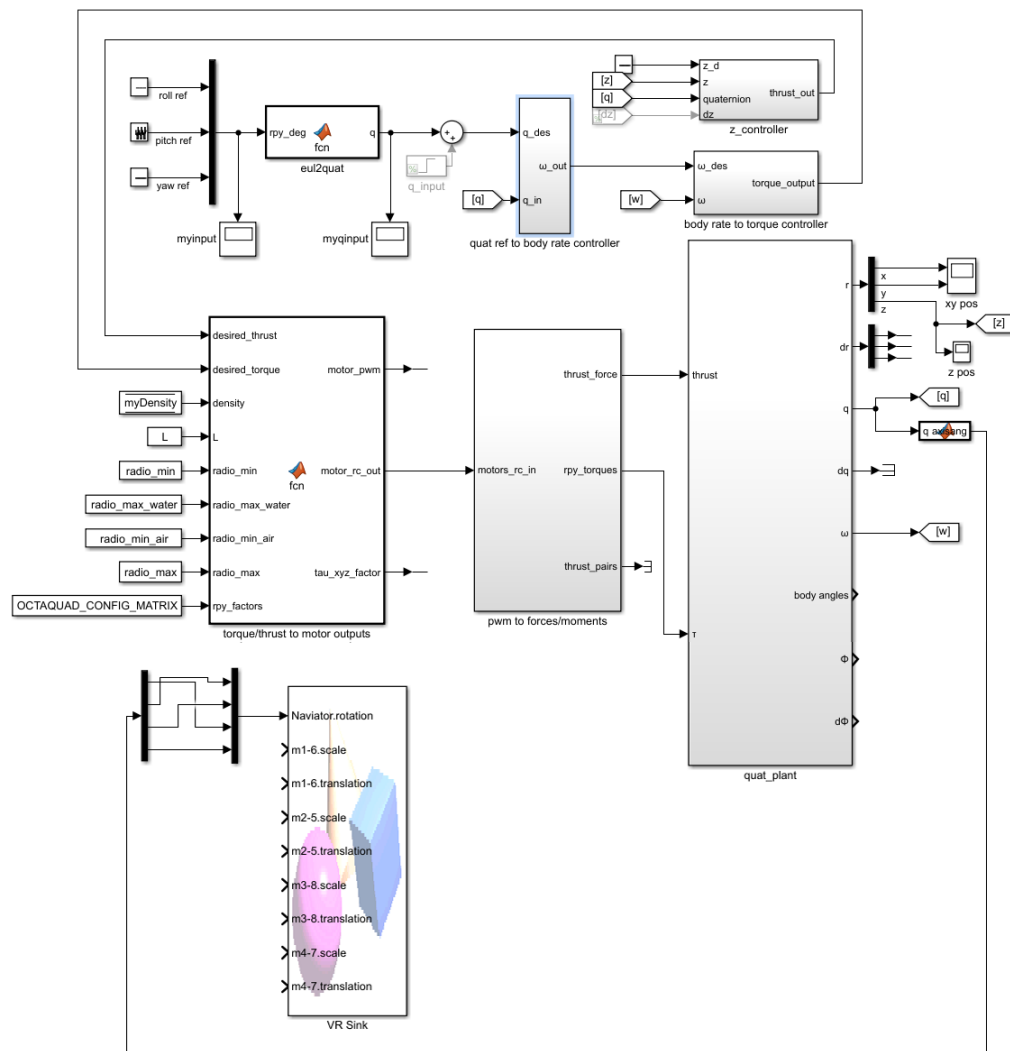


Figure B.1: Snapshot of the outermost layer of the Simulink model created to model the quaternion controller on a multi-medium vehicle.